

MODEL PREDICTIVE CONTROL METHODS FOR PHOTOVOLTAIC  
ELECTRICAL ENERGY CONVERSION SYSTEMS

A Dissertation

by

MORCOS MORAD SAAD METRY

Submitted to the Office of Graduate and Professional Studies of  
Texas A&M University  
in partial fulfillment of the requirements for the degree of

DOCTOR OF PHILOSOPHY

Chair of Committee,  
Committee Members,

Robert S. Balog  
Miroslav Begovic  
Shankar Bhattacharyya  
John Valasek

Head of Department,

Miroslav Begovic

May 2020

Major Subject: Electrical Engineering

Copyright 2020 Morcos Morad Saad Metry

## ABSTRACT

Solar photovoltaic energy systems (PV) have had a consistently increasing market penetration over the past seven years, with a total global installed capacity of over 500 GW. A PV installation must harvest the maximum possible electrical energy at the lowest cost to be economically justifiable. This presents many engineering challenges and opportunities within power electronics amongst which include low-cost power converter implementation, high reliability, grid-friendly integration, fast dynamic response to track the stochastic nature of the solar resource, and disturbance rejection to grid transient and partial shading.

This dissertation investigates the controls of the power electronic interface with the objective to reduce cost, increase reliability, and increase efficiency of PV energy conversion systems. The overall theme of this dissertation involves exploring the theory of model predictive control (MPC) within a range of applications for PV systems. The applications within PV energy conversion systems are explored, ranging from cell to grid integration.

MPC-based maximum power point tracking (MPPT) algorithm is investigated for the power electronics interface to maximize the energy harvest of the PV module. Within the developed MPC based MPPT framework, sensorless current mode and adaptive perturbation are proposed. The MPC framework is expanded further to include inverter control. The control of a single-phase H-bridge inverter and sub-multilevel inverter are presented in this dissertation to control grid current injection. The multi-objective

optimization of MPC is investigated to control the dc-link voltage in microinverters along with grid current control. The developed MPC based MPPT controller is shown to operate with a single-stage impedance source three-phase inverter with PID based grid-side control.

## DEDICATION

*To my mother; Mona*

*To my father; Morad*

*To my brother; Bishoy*

## ACKNOWLEDGEMENTS

I begin this acknowledgment by commending Prof. Robert S. Balog for his supervision and direction of my work. Prof. Balog has had a profound impact on my career, as he helped me expand my intellectual abilities and taught me how to apply those in engineering and teaching alike. I am truly indebted to Prof. Balog for his time and patience throughout my studies. I would also like to thank my committee members, Prof. Miroslav Begovic, Prof. Shankar P. Bhattacharyya, and Prof. John Valasek, for their guidance and support throughout the course of this research.

Thanks also go to my friends and colleagues and the department faculty and staff for making my time at Texas A&M University a great experience. In particular, I am indebted to Prof. Mohammad B. Shadmand for his mentorship and collaboration when I first joined the REAPER lab. I acknowledge Dr. Wesam Rohouma for his assistance and direction of my experimental work for this dissertation. I also learned a lot from, and appreciated working with many mentors and colleagues, namely Prof. Haitham Abu-Rub, Dr. Mostafa Mousa, Prof. Yushan Liu, Dr. Sertac Bayhan, Dr. Mohammed Trabelsi, Dr. Xiao Li, Dr. Shunlong Xiao and Dr. Naki Guler. Thank you Minjeong Kim for your kind help in my defense logistics. Also, thanks to Sawsan Shukri for helping me with linguistics and editing of this dissertation. Thank you Dr. Ayman Bassil for your support throughout my scholarship. I acknowledge my dear friends Dr. Mina Shaker, Dr. Joseph Riad, Dr. Joseph Costandy, Dr. David Shoukr and Dr. Sinan Al Obaidly.

Last but never the least, thanks to my mother, father, and brother for their encouragement and for standing by me during the hardest of times.

## CONTRIBUTORS AND FUNDING SOURCES

### Contributors

This work was supervised by a dissertation committee consisting of Professors Robert S. Balog [advisor], Miroslav Begovic [member] and Shankar P. Bhattacharyya [member] of the Department of Electrical and Computer Engineering, and Professor John Valasek of the Department of Aerospace Engineering.

All other work conducted for the dissertation was completed by the student independently.

### Funding Sources

Graduate study was fully supported by a scholarship from the Qatar National Research Fund as part of the Qatar Research Leadership Program (grant number: QRLP8-G-3330036).

This dissertation was also made possible by NPRP Grant 7-299-2-124 from the Qatar National Research Fund (a member of Qatar Foundation). The statements made herein are solely the responsibility of the authors.

## TABLE OF CONTENTS

	Page
ABSTRACT .....	ii
DEDICATION .....	iv
ACKNOWLEDGEMENTS .....	v
CONTRIBUTORS AND FUNDING SOURCES.....	vi
TABLE OF CONTENTS .....	vii
LIST OF FIGURES.....	x
LIST OF TABLES .....	xvii
1. INTRODUCTION.....	1
1.1. Power electronic interfaces for solar photovoltaic systems .....	2
1.2. Maximum power point tracking in photovoltaic power electronic interfaces .....	4
1.3. Model predictive control of power electronic interface in PV applications .....	5
1.4. Dissertation overview.....	6
2. FOUNDATIONS OF MODEL PREDICTIVE CONTROL IN POWER ELECTRONICS APPLICATIONS .....	10
2.1. Background on hybrid systems .....	11
2.2. Power converter modeling .....	13
2.3. Classification of predictive controllers .....	16
2.4. The basic principles of MPC.....	19
2.5. MPC cost functions .....	20
2.6. Cost function optimization .....	23
2.7. Understanding the MPC control handler.....	25
2.8. Fixed frequency MPC .....	27
2.9. Low-cost microcontroller implementation.....	28
2.10. Conclusion.....	30
3. MAXIMUM POWER POINT TRACKING IN DC POWER OPTIMIZERS.....	32
3.1. Introduction .....	32
3.2. Maximum power point tracking.....	34
3.3. Background on the flyback converter topology .....	36

3.3.1. Circuit analysis .....	37
3.3.2. Steady-state averaging .....	38
3.4. The MPC formulation .....	39
3.4.1. MPC implementation to the flyback converter .....	39
3.4.2. MPC based load prediction .....	39
3.4.3. MPC based maximum power point tracking .....	40
3.4.4. MPC sensorless current mode .....	41
3.4.5. MPC adaptive cost function .....	42
3.5. Simulation .....	46
3.5.1. The real time simulation setup .....	46
3.5.2. Step response and dynamic response results .....	47
3.5.3. The EN50530 test standard .....	49
3.5.4. EN50530 standardized test results .....	50
3.5.5. Parameter mismatch study .....	52
3.5.6. Model parity study .....	56
3.6. Experimental verification .....	60
3.6.1. Experimental setup .....	60
3.6.2. Experimental results .....	62
3.6.3. Analysis of results based on NREL data .....	63
3.6.4. Comparative analysis of results .....	64
3.6.5. Results discussion .....	66
3.7. Implementation in a low cost microcontroller unit .....	67
3.8. Conclusion .....	73
4. MAXIMUM POWER POINT TRACKING IN A GRID-INTERACTIVE INVERTER – SUB-MULTILEVEL INVERTER .....	75
4.1. Introduction .....	75
4.2. Background on the sub-multilevel inverter .....	78
4.2.1. Circuit analysis .....	78
4.3. The boost converter .....	81
4.3.1. Circuit analysis .....	81
4.3.2. Steady-state averaging .....	83
4.4. Developing the MPC formulation for the sub-multilevel inverter .....	84
4.4.1. MPC-based grid current controller .....	84
4.4.2. MPC-MPPT for PV side .....	85
4.4.3. Overall MPC framework for sMI .....	90
4.5. Simulation results .....	90
4.6. Conclusion .....	96
5. MAXIMUM POWER POINT TRACKING IN A GRID-INTERACTIVE INVERTER – QUASI-Z-SOURCE INVERTER .....	98
5.1. Introduction .....	98



5.2. Background on the quasi-Z-source inverter topology.....	100
5.2.1. Circuit analysis.....	100
5.3. Developing the MPC formulation.....	102
5.3.1. MPC-MPPT for PV side.....	103
5.3.2. Grid-side PQ decoupling control.....	104
5.3.3. Overall controller.....	105
5.4. Simulation results.....	106
5.5. Conclusion.....	109
6. DOUBLE-FREQUENCY POWER RIPPLE CONTROLLER.....	110
6.1. Introduction.....	110
6.2. Background on the ripple port microinverter topology.....	112
6.3. The motivation for a closed-loop controller for ripple port.....	115
6.3.1. Parametric sweep study.....	115
6.3.2. Modulator based closed-loop controller based on the hill-climbing algorithm.....	118
6.3.3. Simulation results of the modulator based control algorithm.....	120
6.3.4. Results discussion – motivation for MPC regulator.....	124
6.4. Developing the MPC formulation.....	126
6.4.1. Background on MPC based grid current controller for a single-phase inverter.....	126
6.4.2. Proposed MPC-based dc-link voltage controller.....	127
6.4.3. Overall MPC cost function.....	130
6.5. Simulation results.....	131
6.6. Conclusion.....	133
7. CONCLUSION.....	134
REFERENCES.....	136
APPENDIX A SENSORLESS CURRENT MPPT BASED ON MPC.....	152
APPENDIX B MPC CONTROLLED RIPPLE-PORT MODULE INTEGRATED INVERTER CODE.....	155

## LIST OF FIGURES

	Page
Figure 1.1 Contributions of this dissertation to the PV energy harvesting system. ....	3
Figure 1.2 Some power electronic interfaces typically used in the PV market and discussed in this dissertation. ....	4
Figure 1.3 Applications considered within the PV energy harvesting system are presented in the following chapters. ....	6
Figure 1.4 Contributions of this dissertation to the PV energy harvesting system. ....	9
Figure 2.1 Hybrid systems are an interaction between continuous and discrete dynamics as adapted from [59]. ....	12
Figure 2.2 Voltage vectors of a three-phase two-level inverter as adapted from [61]. ....	15
Figure 2.3 Classification of predictive control methods used in power electronics as adapted from [43]. ....	17
Figure 2.4 A generalized block diagram on the fundamentals of MPC implementation for power electronics converters. ....	22
Figure 2.5 The concept of moving horizon estimation is a fundamental concept in understanding model predictive control adapted from [73]. ....	24
Figure 2.6 The buck converter circuit topology. The double-throw switch could be placed in position '1' or in position '2' ....	26
Figure 2.7 The buck converter switching configurations. The switching configuration on the left ( $\sigma = 1$ ) occurs when the double-throw switch is in position 1. The switching configuration on the right ( $\sigma = 2$ ) occurs when the double-throw switch is in position 2. ....	27
Figure 3.1 The flyback converter topology with snubber circuit for PV application. ....	36
Figure 3.2 The flyback converter configuration when $Qf$ is turned on, $\sigma=1$ (left), and when $Qf$ is turned off, $\sigma=0$ (right). ....	37
Figure 3.3 A flowchart of the proposed ASC-MPPT algorithm showing the control sequence of the proposed integrated MPC cost function. ....	45
Figure 3.4 The flyback converter with snubber circuit for PV application and a detailed block diagram of the proposed ASC-MPPT algorithm. ....	45

Figure 3.5 PV current and voltage under gradual change in solar irradiance. ....	48
Figure 3.6 PV current and voltage under step change in solar irradiance level. ....	48
Figure 3.7 PV current and voltage ripple at 750 W/m <sup>2</sup> solar irradiance level. ....	48
Figure 3.8 The EN 50530 test sequence used in this experiment is composed of two parts: 1- Medium to high solar irradiance level (black solid line) and 2- Low to medium solar irradiance level (blue dashed line). ....	50
Figure 3.9 PV power under dynamic EN 50530 standard test. ....	51
Figure 3.10 PV current under dynamic EN 50530 standard test. ....	51
Figure 3.11 PV voltage under dynamic EN 50530 standard test. ....	51
Figure 3.12 The control effectiveness of ASC-MPPT under load parameter mismatch. ....	53
Figure 3.13 A model parameter mismatch, the output capacitance, $C$ is tested for a mismatch of $\pm 50\%$ of the nominal model value of $C = 680 \mu F$ . The equivalent series resistance is tested for mismatch of $\pm 50\%$ of the nominal datasheet value of $ESR = 0.1 \Omega$ . The control effectiveness is recorded and statistically analyzed using a two-way ANOVA study. ....	54
Figure 3.14 Measured current, observer-model estimated current and theoretical PV current compared for different irradiance values. ....	56
Figure 3.15 A comprehensive SCM parity study of ASC-MPPT estimated current. (a) The error between the estimated current and the measured current in Amperes. (b) The error between estimated current and the theoretical current in Amperes. (c) Error between measured current and theoretical current in Amperes. (d) The magnitude of the estimation error percentage relative to theoretical current. (e) The magnitude of the estimation error percentage relative to the measured current. ....	58
Figure 3.16 Parametric study of the error as a function of compensation. Selecting 0.18 A as a value for error compensation minimizes the error between the magnitude of error between the estimated current and the measured current. To minimize the error between the estimated current and the MPPT theoretical current, other techniques could be employed. ....	59
Figure 3.17 The experimental setup while running the EN50530 standardized test on the proposed ASC-MPPT algorithm. ....	61

Figure 3.18 Portion of the EN 50530 standardized test applied to the experimental setup. (a) Oscilloscope waveforms of the experimental setup running the proposed ASC-MPPT algorithm for an hour and ten minutes long portion of the EN50530 standardized test. PV voltage, PV current and Load voltage do show the tracking throughout the timeframe of the test. (b) Actual circuit operation power waveform calculated for the experimental setup running the proposed ASC-MPPT algorithm and compared to the theoretical MPP. (c) Control efficacy of the proposed algorithm throughout the portion of the test. Upper and lower boundaries are calculated by accounting for instrumentation precision.....63

Figure 3.19 The insolation and temperature data used were based on the 2018 NREL data for the State of Arizona. The captured energy in kWh is based on theoretical MPP for the setup used in this chapter. (a) Total energy captured throughout a year binned by solar irradiance of 20 W/m<sup>2</sup>. (b) Cumulative distribution function showing the amount of available energy captured over the solar irradiance bins. The total amount of available energy captured is 23.5% for irradiance values less than 500 W/m<sup>2</sup>. .....64

Figure 3.20 An experimental comparison based on hardware tests for the proposed ASC-MPPT in comparison to Incremental Conductance (Inc) MPPT based on portion of the EN50530 testing sequence from irradiance 500 W/m<sup>2</sup> to 1000 W/m<sup>2</sup>. (a) Power waveform for the experimental setup running the proposed ASC-MPPT algorithm. (b) Power waveform calculated from a ten-minute portion of the test measurements for the experimental setup running Incremental conductance MPPT. Waveform in (a) shows similar efficacy like (b), but with significantly less oscillations.....64

Figure 3.21 An experimental comparison based on hardware tests for the proposed ASC-MPPT in comparison to Incremental Conductance (Inc) MPPT based on a step change test from irradiance 500 W/m<sup>2</sup> to 750 W/m<sup>2</sup> to 1000 W/m<sup>2</sup> and back to 750 W/m<sup>2</sup> then 500 W/m<sup>2</sup>. (a) Power waveform for the experimental setup running the proposed ASC-MPPT algorithm. (b) Power waveform calculated from a ten-minute portion of the test measurements for the experimental setup running Incremental conductance MPPT. The waveform in (a) shows lower settling time, lower steady-steady error and less oscillations than (b).....66

Figure 3.22 A contour plot showing control effectiveness results for the proposed ASC-MPPT corresponding to different temperature and insolation data. ....67

Figure 3.23 Implementation schema of the control algorithm. ....68

Figure 3.24 Implementation schema of the control algorithm. ....70

Figure 3.25 Portion of the EN 50530 standardized test applied to the experimental setup using TI C2000. (a) Oscilloscope waveforms of the experimental setup running the proposed ASC-MPPT algorithm for an hour and ten minutes long portion of the EN50530 standardized test. PV voltage, PV current and Load voltage do show the tracking throughout the timeframe of the test. (b) Actual circuit operation power waveform calculated for the experimental setup running the proposed ASC-MPPT algorithm and compared to the theoretical MPP. (c) Control efficacy of the proposed algorithm throughout the portion of the test. Upper and lower boundaries are calculated by accounting for instrumentation precision.....	71
Figure 3.26 An experimental comparison based on hardware tests for the proposed ASC-MPPT in comparison to Incremental Conductance (Inc) MPPT based on a step change test from irradiance 500 W/m <sup>2</sup> to 750 W/m <sup>2</sup> to 1000 W/m <sup>2</sup> and back to 750 W/m <sup>2</sup> then 500 W/m <sup>2</sup> . (a) Power waveform for the experimental setup running the proposed ASC-MPPT algorithm. (b) Power waveform calculated from a ten-minute portion of the test measurements for the experimental setup running Incremental conductance MPPT. The waveform in (a) shows lower settling time, lower steady-steady error and less oscillations than (b).....	72
Figure 3.27 An experimental comparison based on hardware tests for the proposed ASC-MPPT in comparison to Incremental Conductance (Inc) MPPT based on realistic NREL data. (a) Power waveform for the experimental setup running the proposed ASC-MPPT algorithm. (b) Power waveform calculated from a ten-minute portion of the test measurements for the experimental setup running Incremental conductance MPPT. The waveform in (a) shows lower settling time, lower steady-steady error and less oscillations than (b). .....	72
Figure 4.1 Submodule PV power processing for MPPT to reduce the effect of partial shading. The output of the dc power optimizer stage is connected to a single-phase 7-level SMI.....	76
Figure 4.2 The block diagram of single-phase 16-level SMI in a PV generation system.....	78
Figure 4.3 The output voltage levels produced by the 16-level input stage ( <i>vinv</i> ) as a function of the link voltage ( <i>vlink</i> ).....	79
Figure 4.4 The block diagram of single-phase 7-level SMI in a PV generation system.....	80
Figure 4.5 The block diagram of the boost converter. ....	81

Figure 4.6 The boost converter configuration when $Q_b$ is turned on, $\sigma=1$ (top), and when $Q_b$ is turned off, $\sigma=0$ (bottom). .....	82
Figure 4.7 The block diagram of the sensorless current MPPT algorithm applied to the boost converter. The current surrogate model is derived from within the converter discrete-time model. The use of this sensorless current MPPT adds sizeable benefits for the cascaded dc optimizer illustrated in Figure 4.1. These benefits include reduced hardware cost and improved reliability, especially so when considering 16-level sMI, as in Figure 4.2. ...	89
Figure 4.8 The block diagram of single-phase 7-level SMI in the PV generation system.....	90
Figure 4.9 PV characteristics used in the simulation. ....	91
Figure 4.10 Solar irradiance profile. ....	92
Figure 4.11 PV current using SC-MPC-MPPT and the current ripple.....	93
Figure 4.12 PV voltage using SC-MPC-MPPT and the voltage ripple.....	93
Figure 4.13 PV power using SC-MPC-MPPT and a zoomed-in plot of the PV power during transient step response. ....	94
Figure 4.14 The response of the current fed to the grid by sMI to step-change in solar irradiance level. ....	94
Figure 4.15 Total harmonic distortion in current fed to grid by sMI. ....	95
Figure 4.16 The output voltage of the sMI before the inductive filter.....	95
Figure 4.17 PV current and voltage under step change in solar irradiance level, along with zoomed-in plots of the ripples. Both the current and voltage track the MPP reference. ....	96
Figure 5.1 Known grid interactive PV systems (left) are comprised of multiple stage power processing which impacts system efficiency. The qZSI (right) is capable of both power conditioning of the PV input and grid current injection to the grid. ....	99
Figure 5.2 Three-phase grid-connected quasi-Z-source inverter topology for PV application. ....	100
Figure 5.3 Analysis of qZSI in non-overlap mode.....	100
Figure 5.4 Analysis of qZSI in overlap mode. ....	100

Figure 5.5 MPC-MPPT determines the overlap period, while the grid-side PQ decoupling control determines the modulation index, $M$ . The advantage of qZSI topology is its single-stage power processing of PV systems. The single-power processing is made possible as the control of a qZSI has two degrees of freedom. ....	102
Figure 5.6 The control block diagram of three-phase qZSI in PV generation system. ...	106
Figure 5.7 Simulation results. (a) PV current using P&O MPPT. (b) PV voltage using P&O MPPT. (c) PV power using P&O MPPT. (d) PV current using MPC-MPPT. (e) PV voltage using MPC-MPPT. (f) PV power using MPC-MPPT. (g) Response of the current fed to grid by qZSI to step change in solar irradiance level. (h) Zoomed in plot of the current fed to grid by qZSI. (i) Total harmonic distortion in current fed to grid by qZSI. ....	108
Figure 6.1 Ripple port circuit schematic. ....	112
Figure 6.2 Full parametric sweep. (a) Ripple Port Inverter Parameter sweep contour plot with modulation index varied from 0.1 to 0.7, and the inverter phase angle varied from 30 to 60 degrees. (b) Zoomed in Ripple Port Inverter Parameter sweep contour plot with modulation index varied from 0.36 to 0.4, and the inverter phase angle varied from 48 to 50 degrees. This parametric sweep indicates the presence of a global minimum point at which the capacitor link voltage ripple is minimized to 2% at a modulation index of 0.38 and a phase angle of 49 degrees. ....	117
Figure 6.3 Closed-loop hill-climbing based auto-tuning algorithm for the ripple port configuration to achieve a double frequency ripple cancellation. ....	119
Figure 6.4 Link capacitor voltage response to turning-on the ripple port and its proposed closed loop at time equals 1s. The magnitude of the voltage ripple of the link voltage has gone down from 13.5% to 4% as a result of the hill-climbing auto-tuning algorithm applied on the ripple port. By further tuning of the controller step-size, ripple performance can be further improved. The present step size for the modulation index controller is $\Delta Mod = 0.008$ and that of the phase angle is $\Delta Ang = 0.02$ . ...	121
Figure 6.5 Auto-tuning of the ripple-port parameters: modulation index and phase angle, and the resultant inverse form factor of the dc-link voltage. (a) The auto-tuning of the modulation index by the hill-climbing algorithm. (b) The auto-tuning of the phase angle by the hill-climbing algorithm. (c) The inverse form factor ( $V_{ave}/V_{rms}$ ) of the dc-link voltage has approached a value much closer to the ideal “1”. The observed oscillation is due to the inherent extremum-seeking behavior of the hill-climbing algorithm. ....	122

Figure 6.6	Grid side voltage and current are in-phase before and after the turning on of the closed-loop ripple port inverter controller. This indicates that unity power factor is maintained before and after turning on the ripple port controller. The total harmonic distortion in the grid current was found to be 2.4% after the closed loop controller was activated. ....	123
Figure 6.7	The voltage on the ripple port filter capacitor ( $V_{Cd}$ ) during its operation relative to the dc input voltage ( $V_{dc}$ ) and grid ac voltage ( $V_{ac}$ ). The phase shift between $V_{Cd}$ and $V_{ac}$ is determined by the hill-climbing closed-loop controller of the ripple port. ....	123
Figure 6.8	Block diagram of the modulator based closed loop controller of the RP-MII. As can be noted, two major loops are displayed: the PQ decoupling controller for the grid side and the dc link voltage ripple loop for the ripple port. More sophisticated controllers on the grid-side have a dc link voltage regulator loop embedded in the grid-side loop. The hill-climbing algorithm of the ripple port is composed of two independent loops. ....	125
Figure 6.9	Equivalent circuit of the RP-MII during different switching states. The constants $\alpha$ and $\beta$ have the values in Table 6.2, depending on the switching state $\sigma = \{1,2,..,9\}$ . ....	127
Figure 6.10	A block diagram of the MPC control strategy applied to the RP-MII. ....	131
Figure 6.11	Link capacitor voltage response to turning on the ripple port at time equals 1s. The magnitude of the voltage ripple of the link voltage has been reduced to 5.3%. ....	132
Figure 6.12	Grid side voltage and current are in-phase before and after the turning on of the closed-loop ripple port inverter controller. ....	133



## LIST OF TABLES

	Page
Table 2.1 Examples of digital control platforms as modified from [85].....	29
Table 3.1 Major characteristics comparison of ASC-MPPT with other well-known MPPT techniques and a few more advanced algorithms.....	46
Table 3.2 Simulation model parameter table .....	47
Table 3.3 Details of the experimental setup.....	61
Table 4.1 Switching table for the single-phase H-bridge.....	79
Table 4.2 Switching table for the 7-level sMI.....	81
Table 5.1 Simulation parameters of the qZSI system .....	107
Table 6.1 Simulation parameters of the modulator-based controller.....	120
Table 6.2 Switching states for a single-phase inverter.....	126
Table 6.3 Switching states of the RP-MII.....	129
Table 6.4 Simulation parameters of the RP-MII system.....	131

## 1. INTRODUCTION

Today's society has become increasingly dependent on electricity. A single day power outage could cost small to medium businesses up to \$35 thousand and could cost large businesses up to \$2.3 million [1]. With a world population of over 7.6 billion people, rising birth rates and rising life expectancies at unprecedented rates [2], developing the electrical infrastructure to meet energy demand becomes a real global challenge. The world energy consumption is projected to rise by nearly 50% between 2018 and 2050 [3]. The National Academy of Engineers (NAE) identified the electricity grid (electrification) as one of the greatest achievements of the 20th century [4]. Electrification has been shown to account for 25% of the global greenhouse emissions [5]. Meeting the rising energy demands using carbon-based fuels increases the carbon footprint of electricity generation even further. Therefore, a thorough investigation of new and clean energy sources using sustainable methods are necessary to meet rising energy demands. The new challenge is to integrate renewable energy-based sources into the utility grid. Solar energy is generally abundant and has been shown to reduce carbon emissions. The Fraunhofer photovoltaic report indicated that "in 2018 Greenhouse Gas emissions of about 28 Mio. t CO<sub>2</sub>-equivalent were avoided due to 46 TWh PV electricity consumed in Germany" [6]. The challenge with solar energy is to economically convert it into a usable form to supply the electrical grid. The NAE identified this challenge as one of the 21<sup>st</sup>-century grand challenges [7]. This dissertation studies advanced control techniques for photovoltaic interface converters to make them more cost effective, highly efficient and more reliable.

## **1.1. Power electronic interfaces for solar photovoltaic systems**

Solar photovoltaic energy systems (PV) have had a consistently increasing market penetration over the past seven years, with a total global installed capacity of over 500 GW [8]. A PV installation must harvest the maximum possible electrical energy at the lowest cost to be economically justifiable [9, 10]. This presents many engineering challenges and opportunities within power electronics [11] amongst which are low-cost power converter implementation [12], high reliability [13], grid-friendly integration [14], fast dynamic response to track the stochastic nature of the solar resource [15, 16], disturbance rejection to grid transients [17, 18] and partial shading mitigation [19]. Power electronic interfaces (PEI) are the energy conversion interfaces that condition the voltage level and power output to a usable form in compliance with engineering standards such as IEC 61727 [20]. PEIs could process the power of an array of PV modules interconnected in series or in cascade. PEIs could be connected to standalone PV modules. PEIs could also be connected at the submodule level of a PV module. Different configurations of PV module interconnections are shown in Figure 1.1.

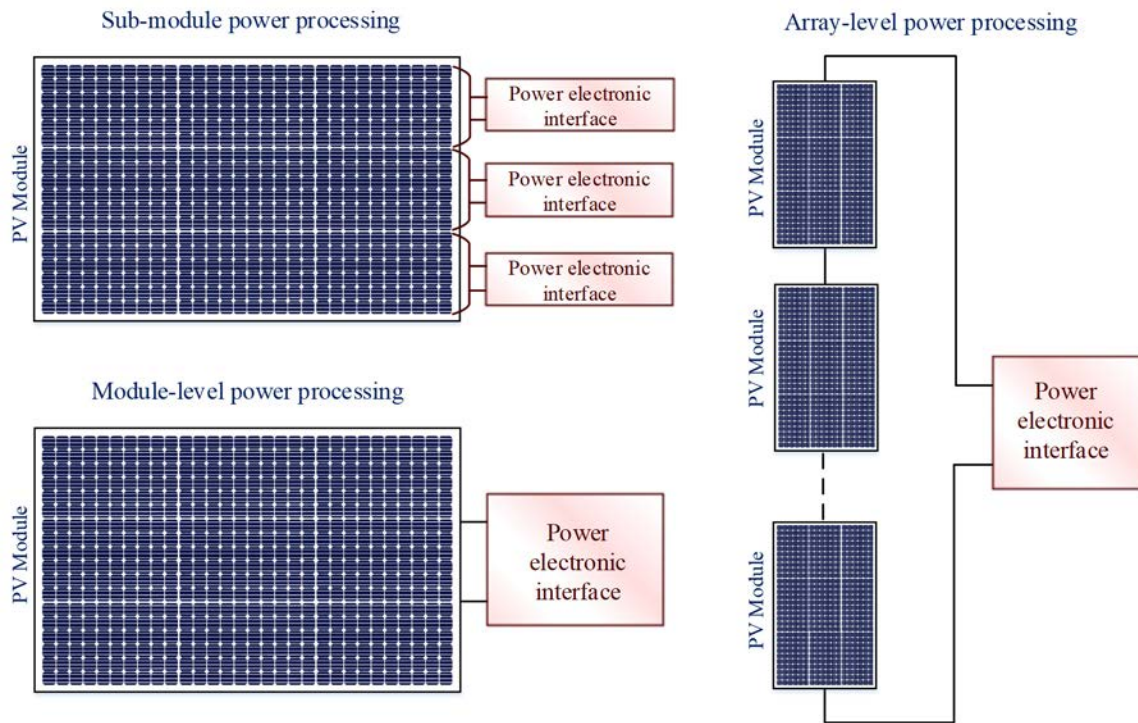


Figure 1.1 Contributions of this dissertation to the PV energy harvesting system.

PEIs used in PV applications range in function, as shown in Figure 1.2. A dc/dc converter is used as a power optimizer stage for PV elements, where each element could be a submodule, a module or an array of PVs. A dc/ac converter (inverter) is used to interact with the utility grid. Microinverters are typically connected to a single PV module. Power optimizers could interface standalone PV modules to a dc load or connected to an inverter stage to interface with the utility grid. Microinverters and dc optimizers are emerging technologies with market shares of 1% and 3%, respectively [6]. String inverters and central inverters for large-scale PV installations dominate the market with a market share of 52% and 44%, respectively [6].

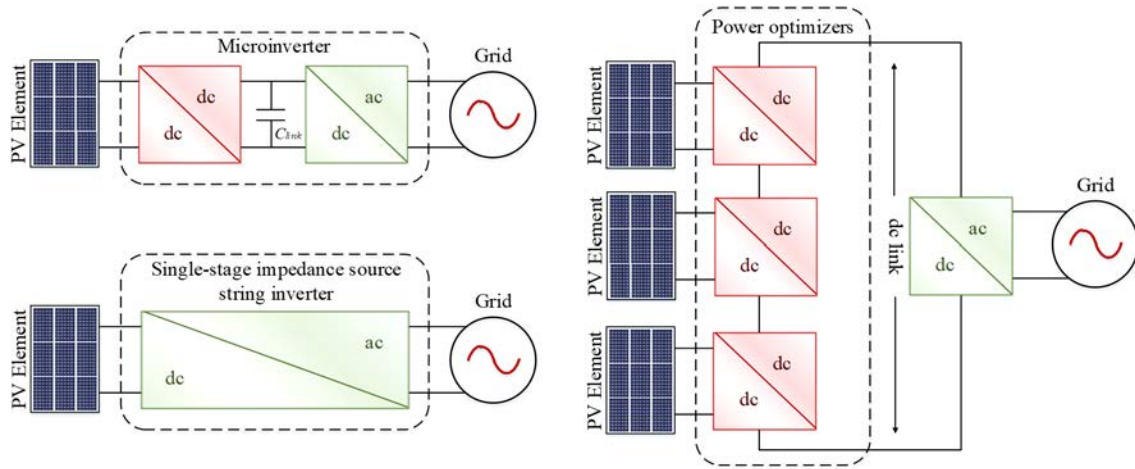


Figure 1.2 Some power electronic interfaces typically used in the PV market and discussed in this dissertation.

## 1.2. Maximum power point tracking in photovoltaic power electronic interfaces

The energy generated from PV systems is highly dependent on environmental factors such as solar irradiation, cloud coverage, and ambient temperature. The challenge with any renewable energy source, particularly solar, is to harvest maximum available energy capacity, even with a stochastic and unpredictable solar irradiation profile [21]. Hence, maximum power point tracking (MPPT) algorithms are employed to ensure that the maximum available energy is harvested from the solar module [22-26]. The concept of MPPT is based on the idea of impedance matching between the PV, the PEI and the load to ensure maximum power transfer [27].

The MPPT controller is mostly implemented in the dc optimizer stage of the solar inverter or to single-stage dc-ac inverters [28-30]. Many MPPT methods have been suggested recently; the relative merits of these various approaches are discussed in [31]. Some MPPT techniques discussed in [31] are: Incremental Conductance (InCon) [32],

Perturb-and-Observe (P&O) [33], fractional Open-Circuit Voltage (Voc) [34], and Best Fixed Voltage (BFV) [35]. The pros and cons of the different MPPT algorithms are generally studied in light of the application. P&O is a well-known technique with relatively good performance; however, P&O method cannot always converge to the true maximum power point [31]. Also, P&O and InCon alike exhibit high steady-state oscillations which reduce overall control efficacy.

### **1.3. Model predictive control of power electronic interface in PV applications**

This dissertation investigates the controls of the PEIs with the objective to reduce cost, increase reliability, and increase the efficiency of PV energy conversion systems. The overall theme of this dissertation involves exploring the theory of model predictive control (MPC) within a range of applications for PV systems. Finite control set MPC is a flexible model-based [36] control method that can include multi-objective optimization [37], constrained control [38], adaptive control [39] and online auto-tuning of weighting factors [40] all in a single controller that exhibits fast dynamic tracking [41].

On the control-side an MPC-based MPPT algorithm is investigated to maximize the energy harvest of the PV module. Within the developed MPC based MPPT framework, sensorless current mode and adaptive perturbation are proposed. The MPC framework is expanded further to include inverter control. The control of a single-phase H-bridge inverter and sub-multilevel inverter are presented in this dissertation to control grid current injection. The multi-objective optimization of MPC is investigated to control the dc-link voltage in microinverters along with grid current control. The developed MPC based

MPPT controller is shown to operate with a single-stage impedance source three-phase inverter with PID based grid-side control.

The MPC framework is developed for

- 1- Maximum power point tracking
- 2- Grid-side current injection controller
- 3- Regulation of dc link voltage ripple

#### 1.4. Dissertation overview

This dissertation investigates the model predictive control technique within PV energy conversion systems. The applications considered illustrate different challenges within the power electronic interface design beginning from the standalone dc optimizer of a PV element to single-stage power processing of a cluster of PV elements. To present the research objectives, different applications are considered according to Figure 1.3.

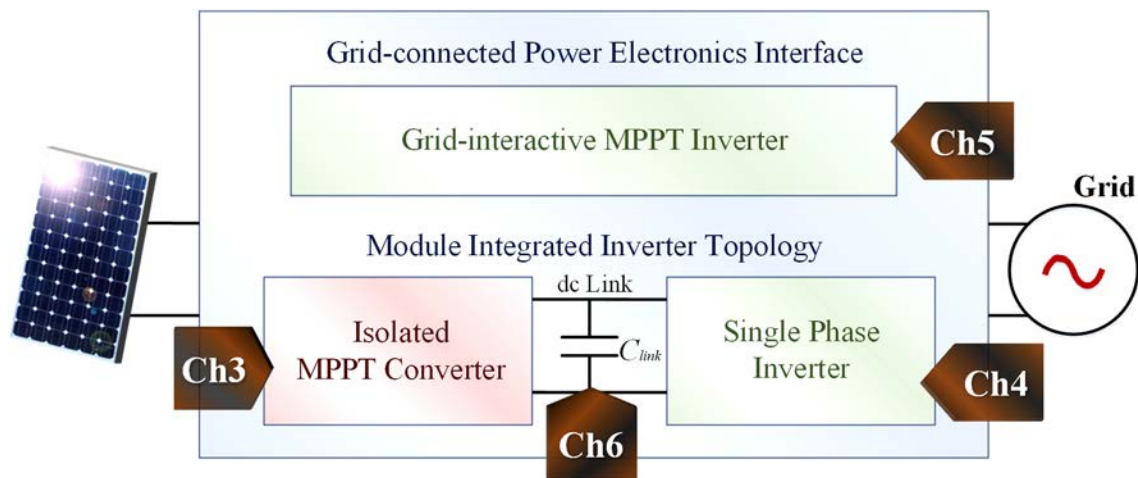


Figure 1.3 Applications considered within the PV energy harvesting system are presented in the following chapters.

Chapter 2 discusses the fundamentals of MPC in power electronics. In this chapter the theory and fundamental operation principles of MPC are being demonstrated. The use case of MPC in power electronics for PV application is established. A complete case on the analysis of the MPC framework for switching power supplies is demonstrated.

Chapter 3 utilizes the model-based framework of MPC to develop an MPPT algorithm that eliminates the input-side current sensor in a PV application. The implementation of MPC realizes the observer-based sensorless current mode being fundamentally model-based design, expressed within the cost function. This chapter also utilizes constrained control and online auto-tuning of MPC to develop an adaptive perturbation MPPT to reduce steady-state oscillation and improve dynamic performance.

Chapter 4 examines the application of the sensorless current MPPT algorithm within submodule PV power processing. The topology of the sub-multilevel inverter (SMI) was considered as its 7-level output voltage is not affected by the mismatch in the submodule voltages of the dc optimizer, making it suitable for the application in this chapter. This chapter demonstrates an MPC framework for both the MPPT controller for the cascaded dc optimizers and the inverter side grid current controller.

Chapter 5 illustrates an approach to integrating MPC-based MPPT controllers within the existing control loop of a three-phase grid connected impedance source inverter. The topology of the impedance source inverter has an inherent advantage that allows two different control objectives to be achieved simultaneously. Such an advantage eliminates the need for two-stage power processing for PV applications.



Chapter 6 explores the topology of the microinverter for a PV module. Single-phase grid-tied inverters have a characteristic double frequency power ripple. This ripple negatively impacts MPPT operation and the parity of the grid-injected current. A model predictive control framework is shown to regulate dc-link voltage ripple the injection while regulating grid current injection.

Overall, the applications within PV energy harvesting systems are explored from generation to grid integration to demonstrate the MPC methods. Power optimizers investigated in this dissertation are the flyback converter and the boost converter. Investigated grid interface inverters include the single-phase H-bridge inverter, the sub-multilevel inverter and the three phase H-bridge inverter. The interaction between dc optimizers and single-phase H-bridge inverters within a microinverter configuration is studied. The interconnection between power optimizers with sub-multilevel inverters is investigated. A single-stage impedance source network with a three-phase H-bridge is investigated for large scale PV installations.

The contributions presented in this dissertation (Figure 1.4) according to the chapters are:

Chapter 3 – Maximum power point tracking of standalone dc power optimizers

- MPC-based sensorless current mode
- MPC-based adaptive perturbation MPPT

Chapter 4 – Maximum power point in a grid interactive inverter – sub-multilevel inverter

- MPC based submodule MPPT converters for partial shading mitigation
- MPC based grid integration based on sub-multilevel inverter

Chapter 5 Maximum power point in a grid interactive inverter – impedance source inverter

- MPC based MPPT control of a single-stage power processing systems
- MPC based MPPT integration with pre-existing PID based controller

Chapter 6 Double frequency power ripple controller for microinverters

- MPC-based control strategy for double frequency ripple on dc link voltage reduction in microinverters
- Integrated multi-objective MPC controller for both grid current injection and dc link voltage control

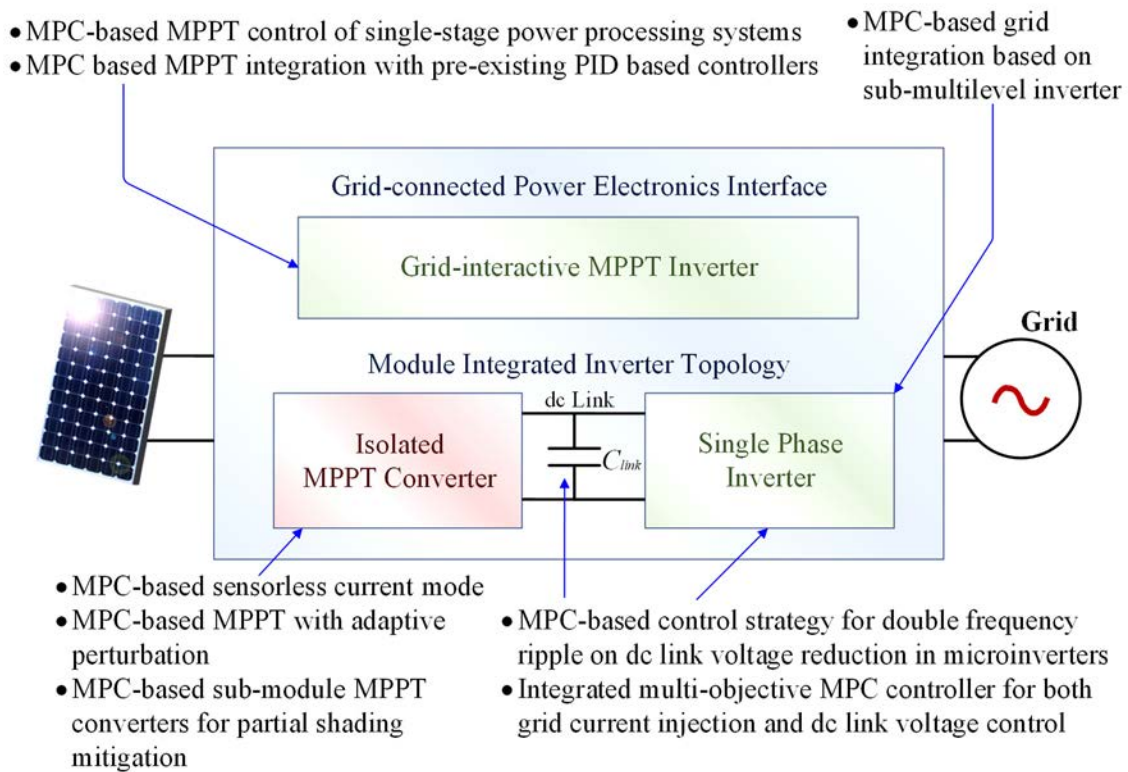


Figure 1.4 Contributions of this dissertation to the PV energy harvesting system.

## 2. FOUNDATIONS OF MODEL PREDICTIVE CONTROL IN POWER ELECTRONICS APPLICATIONS

MPC applications in power electronics can be found in literature from as early as the 1980s for high-power systems with low switching frequency [27, 42, 43]. Model Predictive Control (MPC) is considered to be a mature technique for linear and rather slow systems like the ones encountered in the process industry [44]. More complex systems, such as non-linear, or very fast processes were not considered the realm of MPC [44]. Power converters are hybrid systems that are inherently non-linear and use fast switching. Higher switching frequency devices were not viable at that time due to the immense calculation time required for the control algorithm. The use of finite set MPC, as an optimal controller, has lately gained broad interest in multiple applications in power electronics and motor drives [45-47]. This interest is fueled by the availability of low-cost microprocessors with high processing powers [48-56].

On the one hand, switching power converters are inherently non-linear systems. On the other hand, each state of the power converter, per switching configuration, exhibits electronic linear circuit theory characteristics [57]. Kirchhoff's current and voltage laws allow generating a linear system model for each switching configuration of the power converter [58]. The dichotomy of the switching power converter modeling is described as a hybrid system in control theory [59].

Finite control set model predictive control (MPC) is a model-based [36] control method that can include multi-objective optimization [37], constrained control [38], adaptive control [39] and online auto-tuning of weighting factors [40] all in a single

controller that exhibits fast dynamic tracking [41]. This class of controller is ideally suited for the optimal operation of the switched non-linear control problem studied in this dissertation.

This chapter is organized as follows:

Section 2.1 reviews the concept of hybrid systems and how to model them.

Section 2.2 demonstrates tools in discrete-time modeling of power converters.

Section 2.3 discusses the different classes of predictive controllers.

Section 2.4 illustrates the basic principle of MPC control design.

Section 2.5 provides details on constructing a cost function for power electronics applications.

Section 2.6 presents the concepts of cost function optimization using the receding horizon strategy.

Section 2.7 briefly discusses the control handle of MPC controllers in power electronics.

Section 2.8 shows the possible need for fixed-frequency finite control set MPC.

Section 2.9 presents the challenge of MPC implementation on low-cost microcontroller units.

Section 2.10 concludes this chapter.

## **2.1. Background on hybrid systems**

A system that can be described as an interaction between continuous dynamics and discrete dynamics is often described as a hybrid system [59]. Continuous dynamics can be

expressed in terms of a continuous time-invariant system, such as the linear system in (2.1).

$$\dot{x}(t) = Ax(t) + Bu(t) \quad (2.1)$$

where,

- $x$  state variables,  $x \in \mathbb{R}^n$
- $u$  input signals,  $u \in \mathbb{R}^m$
- $A$  state transition matrix,  $\dim[A(\cdot)] = n \times n$
- $B$  input matrix,  $\dim[B(\cdot)] = n \times m$

Discrete dynamics can be thought of as a deterministic finite state machine, with a finite set  $Q$  and the state  $q \in Q$ . The transitions between the different states are being triggered by some input variable  $v$ . In a hybrid system, the input  $u$  to the continuous dynamics is some function of  $q$ . The value of the input  $v$  to the discrete dynamics is determined by the value of the continuous state  $x$ . An illustrative figure on the interaction between continuous and discrete dynamics in hybrid systems is shown in Figure 2.1 as adapted from [59].

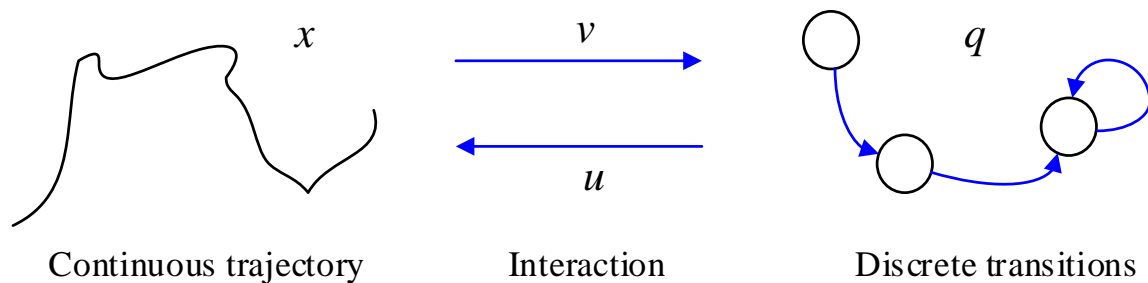


Figure 2.1 Hybrid systems are an interaction between continuous and discrete dynamics as adapted from [59].

In the application of power electronics, power converters can be considered continuous-time systems with isolated discrete switching events. Such systems are referred to as switched systems. A switched system is obtained from a hybrid system by

considering all possible switching states while neglecting the details of the discrete behavior (the switching action).

Suppose a family of functions  $f_\beta$ ,  $\beta \in \mathcal{B}$  where  $\mathcal{B}$  is some finite index set  $\mathcal{B} = \{1, 2, \dots, m\}$ . The state-space representation for a family of linear systems is

$$\dot{x} = f_\beta(x) = A_\beta x, \quad A_\beta \in \mathbb{R}^{n \times n}, \beta \in \mathcal{B} \quad (2.2)$$

A switching signal can be defined using a piecewise constant function  $\sigma: [0, \infty) \rightarrow \mathcal{B}$ . The function  $\sigma$  has a finite number of discontinuities, switching times, and has a constant value on every interval between two consecutive switching times [59]. Thus a switched linear system can be expressed as

$$\dot{x} = f_{\sigma(t)}(x(t)) = A_{\sigma(t)}x(t) \quad (2.3)$$

Power electronics converters are non-linear due to their switching. However, switching systems as shown from this section can be represented as piecewise linear systems based on a switching function.

## 2.2. Power converter modeling

A power electronic switch is typically realized by a semiconductor device optimized for the application like IGBTs, MOSFETs, and diodes. Designing a model for a switched system begins by considering all the switching devices. Ideally, each switching device can be “on” or “off” where “on” refers to current conducting through the device from a first portion of the circuit to a second and “off” refers to the inhibition of current flowing from a first portion of the circuit to a second portion of the circuit. Semiconductor limitations such as on-resistance and turn-on time are neglected to simplify the analysis

[60]. The number of switching configurations generated accordingly is the number of system states. Some of the switching configurations may be defying to some physics or circuit theory principles and are eliminated from the analysis. From this point forward, it is assumed that all switching states considered in the analysis are in fact possible switching states. In practice, the application of Kirchoff's voltage and current laws can reduce the number of possible switch configurations to the number of valid switch configurations by eliminating those that would not be realizable in practice. Since each switch can have two states, the number of possible configurations in a power converter is  $2^s$  where  $s$  is the number of switches.

As an example, a three-phase, two-level inverter has six switches and accordingly has  $2^6 = 64$  switching states. However, the switches in each leg of the two-level inverter should be complimentary to avoid shoot-through. In that case, each phase leg is represented by one switch and the possible switching states are  $2^3 = 8$ . As seen in Figure 2.2 as adapted from [61], the possible switching states generate eight possible voltage vectors. As can be noted in Figure 2.2, states  $S_0$  and  $S_7$  are redundant as their voltage vectors  $v_0$  and  $v_7$  are equal. Redundant states can be eliminated from converter modeling to simplify converter models [62]. In current source converter applications, the relation between switching states and current vectors is analyzed similarly.

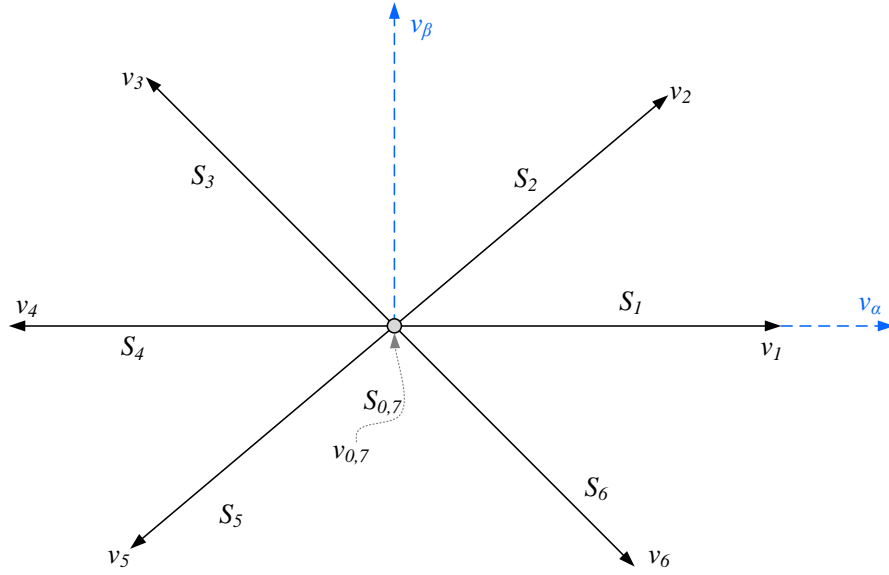


Figure 2.2 Voltage vectors of a three-phase two-level inverter as adapted from [61].

The discrete-time models of the state variables are analyzed using circuit theory to construct model equations to estimate this variable at the next sampling time. Several discretization methods exist to determine the discrete-time model of the system. As an example, for first-order systems, Euler forward method can be used to approximate the derivatives [63]:

$$\frac{dx}{dt} \approx \frac{x(k+1) - x(k)}{T_s} \quad (2.4)$$

where  $T_s$  is the sampling time. Hence, capacitor current and inductor voltage can be expressed by

$$i_c = \frac{dv_c}{dt} \approx \frac{v_c(k+1) - v_c(k)}{T_s} \quad (2.5)$$

$$v_L = \frac{di_L}{dt} \approx \frac{i_L(k+1) - i_L(k)}{T_s} \quad (2.6)$$

Euler forward method may not be an accurate approximation in higher-order systems and the error becomes higher. Thus other discretization techniques are used instead.



### 2.3. Classification of predictive controllers

Predictive controllers include a wide variety of classes that have gained traction for power converter controls. Figure 2.3 shows a classification of different predictive control methods and their main characteristics as adapted from [43]. In predictive controllers, model-based relations are used to estimate the state variables for the next step and are applied to the cost function. According to pre-defined optimization criteria, the controller selects a state  $\sigma$  as the optimal actuation. Hysteresis-based predictive controllers ensure the state variable is the boundaries of a hysteresis area [64]. In trajectory-based predictive controllers, the state variables are forced to follow a certain predefined trajectory [65]. Deadbeat predictive controllers set the error between the state variables and the reference to zero in the next sampling instant [66]. Model predictive controllers use a more generalized form of optimization based on an objective function [67]. As seen in Figure 2.3, deadbeat control and MPC with continuous control set need a modulator to generate the switching signal, which only uses a fixed switching frequency. Other controllers generate the switching signals directly for the converter without the need for a modulator which results in a variable switching frequency.

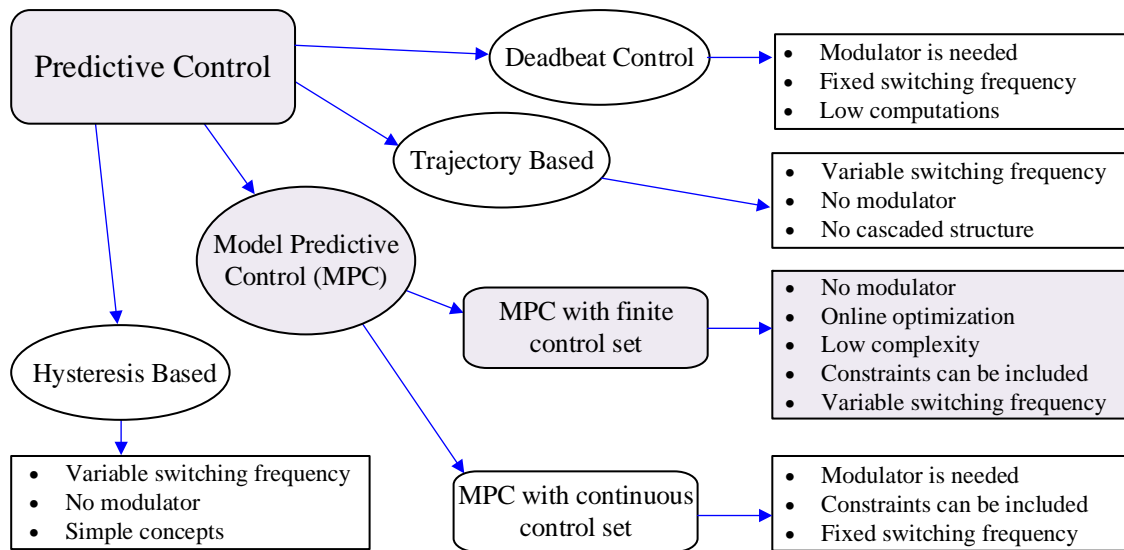


Figure 2.3 Classification of predictive control methods used in power electronics as adapted from [43].

In power electronics, there are advantages for the use of the modulator in very high-frequency converters, for example. These advantages are discussed in section 2.7 on fixed frequency MPC, and a realistic example is given in Chapter 3. Otherwise, the use of finite control set MPC allows the additions of constraints and online optimization of the cost function, which allows for faster system response.

One of the significant advantages of predictive controllers is that the concept is simple and straightforward. When considering continuous control set MPC, the implementation of MPC for some applications is more complex — considering little time available due to small sampling time for calculation of the MPC algorithm and optimization of the MPC algorithm. In some applications, it is common to perform calculations offline using the system and model parameters in a technique known as explicit MPC [68]. In an explicit MPC method, the model of power electronic converter is approximated in the form of a linear system by a modulator to eliminate the need for

online optimization. Explicit MPC algorithms generate control moves in the form of a look-up table containing an optimal solution as a function of the state of the system [69]. Explicit MPC is applied for a wide range of power electronics converter in literature [69-71]. The main drawback of this method is that the discrete characteristics of power electronics converters are not taken into account. Finite control set MPC allows for online optimization while including the discrete characteristics of power converters and pre-defined constraints. More flexibility of implementation and desired constraints for the controller can be achieved when considering online optimization of the cost function in the MPC method.

In summary, finite control set MPC is justified in this dissertation for these reasons:

- The general concepts of MPC are intuitive, which allows practitioners with limited control theory knowledge to design MPC regulators.
- The tuning of MPC is relatively more straightforward, especially when compared to PID controllers.
- Using MPC, multivariable control problems can be solved using multi-objective optimization of the cost function, instead of multiple control loops.
- MPC allows for the inclusion of non-linearities (the switching action) of power converters, without the need for linearization techniques (small-signal averaging).
- MPC allows for the inclusion of constraints during the design process.

Some of the challenges with MPC:

- Derivation of the control law in MPC is more complex, especially when compared to PID control.

- All the computations and online optimization are made every sampling time, which requires higher computing power.
- MPC is based on prior knowledge of the system model and does not account for the model mismatch from the system.
- The variable switching frequency can be disadvantageous for switching devices and circuit elements ratings.

#### **2.4. The basic principles of MPC**

The MPC for power electronics converters can be designed using the following steps [48]:

- Modeling of the power converter to identify all possible switching states and their relation to the input or output voltages or currents.
- Obtaining discrete-time models that allow the predicting of future behavior of the state variables.
- Defining a cost function that represents the desired behavior of the system.

The designed controller should consider the following tasks:

- Predict the behavior of the controlled variables for all possible switching states.
- Evaluate the cost function for each prediction.
- Select the switching state that minimizes the cost function.

The model used for prediction is a discrete-time model which can be presented as the state space of a hybrid system (2.3) model as follow [43]:

$$\begin{aligned}\tilde{x}(k+1) &= A_{\sigma}x(k) + B_{\sigma}u(k) \\ y(k) &= C_{\sigma}x(k)\end{aligned}\tag{2.7}$$

Then a cost function that takes into consideration the future states, references and future actuation can be defined:

$$g = f(x(k), \sigma(k), \dots, \sigma(k+N))\tag{2.8}$$

The defined cost function  $g$  should be minimized for a predefined horizon in time  $N$ ; the result is a sequence of  $N$  optimal actuation:

$$\sigma(k) = [1 \ 0 \ \dots \ 0] \arg \min_{\sigma} g\tag{2.9}$$

Even though  $\sigma(k)$  contains feasible plant inputs over the entire horizon of time only the first element is used in conventional MPC. At the next sampling time  $(k+1)$ , the system states are calculated using the system model, the horizon is shifted by one step, and another optimization is applied. For a horizon length  $N=3$ , the horizon taken into consideration in the minimization of  $g$  slides forward as  $k$  increases. More details on cost function optimization are discussed in section 2.6.

## 2.5. MPC cost functions

Model predictive control (MPC) is a well-known controller framework in which mathematical models are used to optimize the behavior of a physical system. Without loss of generality, finite control set MPC is a suitable variant of MPC in which each possible configuration of the switch mode power supply is evaluated, and the one that minimizes a cost function is chosen as the optimal next configuration. The control requirement such as torque, current or power control can be included in a single cost function,  $g$ , subject to

minimization. Each term in the cost function is multiplied by a weight factor to deal with units and magnitudes of the control variables.

Weight factors in the cost function, in addition to accommodation of different units and scales, enable the prioritization of specific control variables. Selecting weight factors for each control problem is not straight forward [43]. Several empirical approaches to determine a fixed weight factor using trial and error have been investigated in the literature [72]. However, a fixed weight factor is not robust to parameter variation and other uncertainties of the system.

MPC implementation within power electronics is illustrated in Figure 2.4. The controller uses past and present measurements of the state variables  $X(k)$ , to estimate the model behavior of those state variables,  $\tilde{X}(k + N)$  (the tilde denotes an estimated value and  $N$  denotes the length of the prediction horizon) [73]. This estimate,  $\tilde{X}(k + N)$ , is compared to a desired set reference  $X^*(k + N)$  (the star denotes a reference value) to determine the input vector  $\sigma(k + N)$ . The MPC framework requires a cost function, typically denoted with the mathematical symbol  $g$ , which is assigned to one or more mathematical relationships. Each relationship defines a particular objective, such as tracking a reference signal.

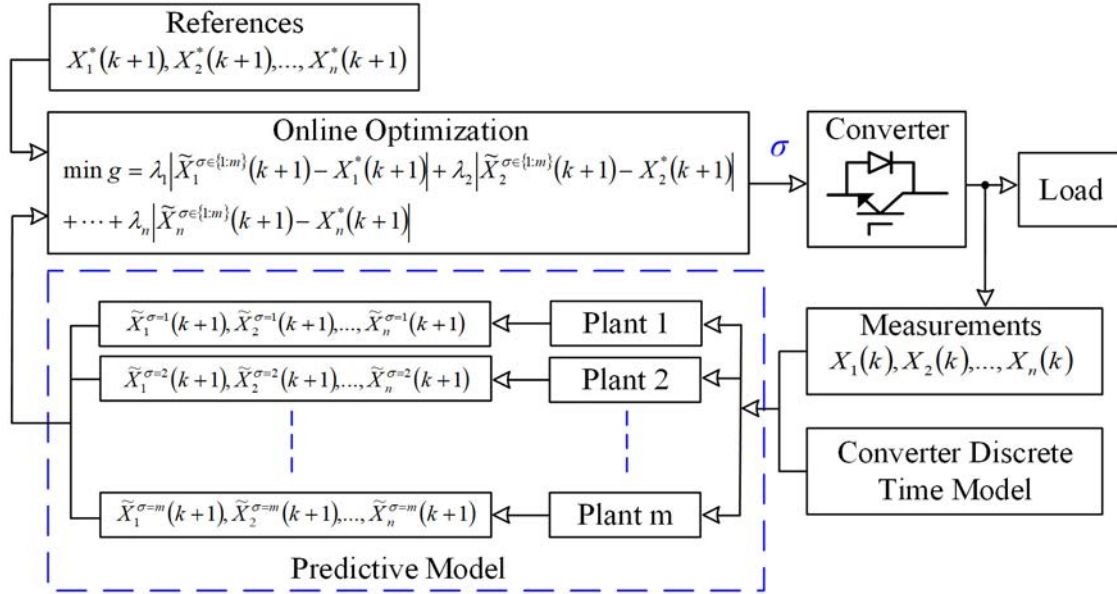


Figure 2.4 A generalized block diagram on the fundamentals of MPC implementation for power electronics converters.

A general formulation of the cost function with ‘ $n$ ’ objectives has the following format:

$$\begin{aligned}
 \min g_{\sigma \in \{1:m\}} &= \lambda_1 |\tilde{X}_1^\sigma(k+1) - X_1^*(k+1)| + \dots + \lambda_n |\tilde{X}_n^\sigma(k+1) - X_n^*(k+1)| \\
 \text{subject to } \tilde{x}(k+1) &= A_\sigma x(k) + B_\sigma u(k) \\
 y(k) &= C_\sigma x(k) \\
 |y(k)| &\leq y_{\text{boundary}}
 \end{aligned} \tag{2.10}$$

where,

- $\lambda_{1..n}$  are the weighting factors that assign significance to some objectives over others
- $\sigma$  denotes the state number
- $m$  the number of possible states for the system
- $\tilde{X}_{1..n}$  the state variables being controlled
- $X_{1..n}^*$  the state references being tracked
- $x$  state variables
- $u$  input signals
- $y$  output signals
- $A$  state transition matrix
- $B$  input matrix
- $C$  output matrix
- $k$  discretized time steps

For each sampling period, the controller evaluates the cost function  $g$  for each valid  $m$  switch configuration. The switch configuration is chosen that minimizes the numerical value of the cost function  $g$ . In general, there can be multiple objectives and the MPC seeks to minimize the net contribution of each cost term. The MPC framework allows for the weighting of the different objectives to give priority or preference.

## 2.6. Cost function optimization

MPC is an optimization-based problem in which the cost function is minimized for a pre-defined prediction horizon of length  $N$ . When using a non-linear model or considering constraints, it is more challenging to use least squares as all the states along the trajectory  $x(T)$  need to be optimized simultaneously to obtain state variable estimates [73]. Such optimization technique is computationally taxing as  $T$  increases. Alternatively, only the measurements within the prediction frame  $y_N(T) = \{y(T - N), \dots, y(T)\}$  are accounted for and only the state variable estimates  $x_N(T) = \{x(T - N), \dots, x(T)\}$  in the prediction frame estimated. This principle is known as the moving horizon estimation or the receding horizon strategy and is illustrated in Figure 2.5 as adapted from [73].



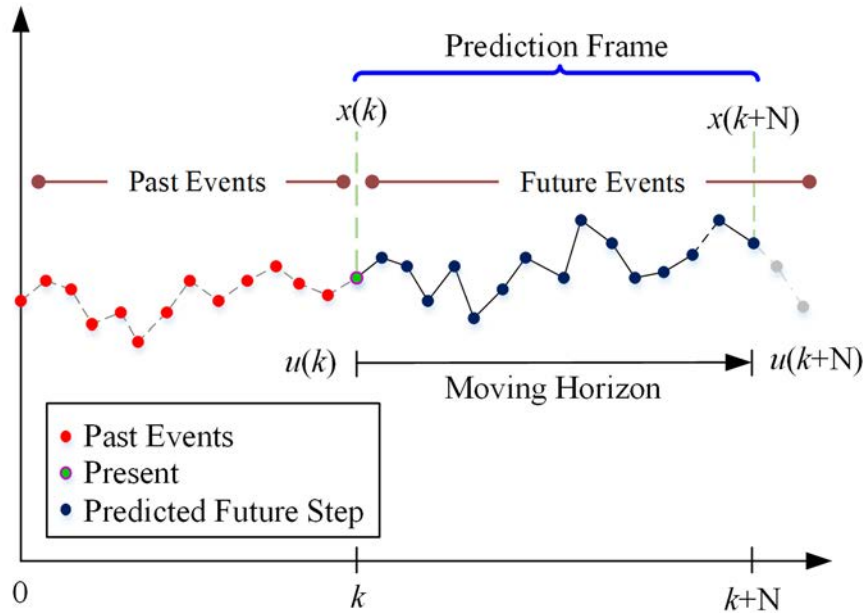


Figure 2.5 The concept of moving horizon estimation is a fundamental concept in understanding model predictive control adapted from [73].

This optimization is subject to the model of the system and the constraints defined in the cost function. The result of the optimization is a sequence of  $N$  optimal actuation. The time range on the resulting sequence is from  $(k + 1)$  to  $(k + N)$ . During time  $k$ , the controller only applies the first element of the sequence, receding strategy, as in:

$$\sigma(k) = [1 \ 0 \ \dots \ 0] \arg \min_{\sigma} g \quad (2.11)$$

At each sampling time, the optimization problem is solved again by using a new set of measured data to obtain a unique sequence of optimal actuation. The MPC principle of working is illustrated graphically in Figure 2.5. As it is shown by using the measured information and system model until time  $k$ , the future value of the system state is predicted until the time  $(k + N)$  in horizon. Then the optimal actuation is calculated by optimizing

the cost function (2.7). As the optimization is complete and the state function  $\sigma(k)$  at time  $k$ , the prediction horizon shifts forward.

## 2.7. Understanding the MPC control handler

In power electronics, the control handle is the switching configuration (i.e. turning the switches on or off). Such a concept may not be entirely intuitive to many classical control theorists. For example, the control handle of the rotation of an airplane about its vertical axis (yaw) is the rudder through adjusting the rudder angle. The control handle for cruise-controlled cars is the throttle to control the engine speed. In classical control techniques (i.e., PID controllers), the switching status can be commanded by adjusting the pulse width of the gating signal for the switch. The resulting pulse width is a percentage (ratio) of the overall sampling time which is analogous to well-known control handlers. The pulse width ratio is known as the duty ratio and is defined as  $t_{on}/T_s$  and is applied to a modulator to generate the switch gating signals. Using finite control set MPC facilitates the control of the switching configuration by turning the switches on or off without the need for a modulator.

The concept of the MPC handler in power electronics could be better explained with an example. Consider the buck converter circuit shown in Figure 2.6; the double-throw switch could either be in position ‘1’ or position ‘2’. The switching configuration on the left of Figure 2.7 ( $\sigma = 1$ ) occurs when the double-throw switch is in position ‘1’. The switching configuration on the right of Figure 2.7 ( $\sigma = 2$ ) occurs when the double-

throw switch is in position '2'. When the switch is in position 1 the currents and voltages using Kirchoff's current and voltage laws can be expressed as

$$i_C^{\sigma=1}(t) = C \frac{dv_{out}}{dt} = i_L(t) - \frac{v_{out}(t)}{R} \quad (2.12)$$

$$v_{L_n}^{\sigma=1}(t) = L \frac{di_L}{dt} = v_{in}(t) - v_{out}(t) \quad (2.13)$$

When the switch is in position '2' the currents and voltages using Kirchoff's current and voltage laws can be expressed as

$$i_C^{\sigma=2}(t) = C \frac{dv_{out}}{dt} = i_L(t) - \frac{v_{out}(t)}{R} \quad (2.14)$$

$$v_{L_n}^{\sigma=2}(t) = L \frac{di_L}{dt} = -v_{out}(t) \quad (2.15)$$

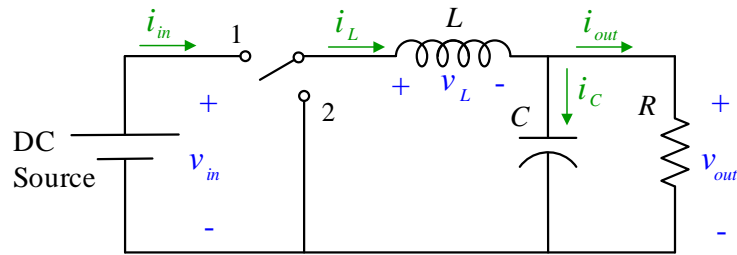


Figure 2.6 The buck converter circuit topology. The double-throw switch could be placed in position '1' or in position '2'.

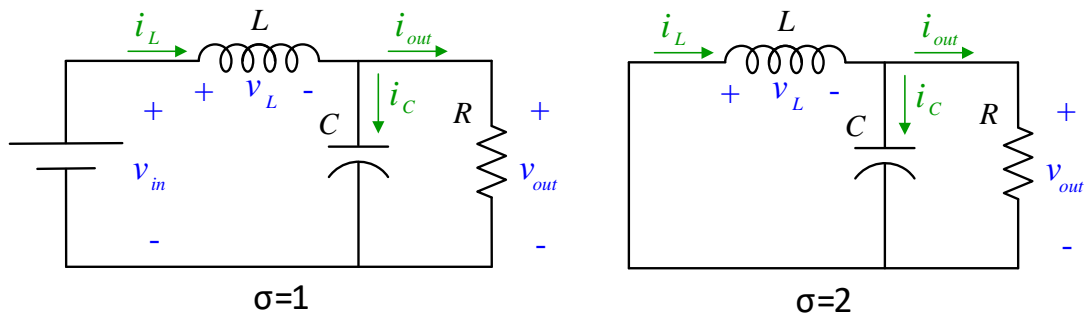


Figure 2.7 The buck converter switching configurations. The switching configuration on the left ( $\sigma = 1$ ) occurs when the double-throw switch is in position 1. The switching configuration on the right ( $\sigma = 2$ ) occurs when the double-throw switch is in position 2.

## 2.8. Fixed frequency MPC

Among the inherent challenges of finite control set MPC controllers is the variable switching frequency which necessitates careful consideration for the sizing of passive components [74] and could cause high input current ripple [75] which adversely affects PV system performance [76]. Some power converter applications need to be switched at high frequency. For example, flyback converters use a high-frequency, as flyback transformers saturate when the switching frequency drops [77]. Variable switching frequency requires switches and passive components to withstand high voltage stresses [78].

Fixed frequency MPC addresses this issue by incorporating some elements of the PWM modulator [36, 79-82]. The idea is to exploit the benefits of finite control set MPC such as online optimization and estimation, including constraints and straightforward control law while having a fixed frequency modulation. Therefore, techniques like explicit MPC and continuous control set MPC are not suitable.





Methods in [80, 81] propose the use of triangular carriers to adjust the size of the MPC generated pulse width. The approach presented in [82] uses the converter model to estimate a discrete-time formulation for duty ratio that is dependent on system measurements and uses pulse width modulation. The approach presented in [36] and employed in this paper uses the mean value of the generated MPC signals to obtain a duty ratio to be applied to a high-frequency PWM modulator. More details on fixed frequency MPC are discussed in Chapter 3.

## **2.9. Low-cost microcontroller implementation**

Control strategies for power converters and drives have been the subject of ongoing research for several decades in power electronics. Classical linear controllers combined with modulation schemes and nonlinear controllers based on hysteresis bounds have become the most used schemes in industrial applications [43]. Many of these concepts go back to research on analog hardware, which limited control complexity. Modern digital control platforms like DSPs have become state of the art and have been widely accepted as industrial standards [24]. The main digital control platforms used in industrial electronics are based on a fixed-point processor, due to the high computational power and low cost [83]. However, in the academic world, control platforms based on floating-point processors with high programming flexibility are more usually used [84]. Recently, hardware and software solutions implemented in field-programmable gate arrays (FPGAs) have received particular attention, mainly because of their ability to allow designers to build efficient and dedicated hardware architectures utilizing flexible

software. The main stream control platforms used in power electronics are summarized in Table 2.1 as modified from [85].

Table 2.1 Examples of digital control platforms as modified from [85].

DSP TMS320F2812	DSP TMS320F28379	FPGA Spartan-6 LX45	dSPACE DS1006
150 MHz Single-core Fixed-point 150 MMACS	200 MHz Dual-core Floating-point 400 MMACS	250 MHz 58 cores Fixed-point 14500 MMACS	2.8 GHz Quad-core Floating-point 11200 MMACS
			

MPC is a computationally intensive control algorithm as each state variable in the system is evaluated for each of the possible control actuates. Adding to the complexity of MPC is the multi-objective optimization of the penalty function. As such, plenty of research on the area of MPC in power electronics implement their algorithms on expensive platforms such as dSPACE and OPAL-RT. While such platforms are excellent rapid prototyping platforms, they are costly and may be impractical in product design. The use of MPC on low-cost microcontroller units (MCU) has been of particular interest in the literature. As is seen in Table 2.1, a comparison between different types of the controller shows that dSPACE and some DSPs use floating-point arithmetic, while FPGA and some DSP models use fixed-point arithmetic. Million multiply-accumulate cycles per second (MMACS) for each type of controller in Table 2.1 are computed as in (2.16) [87].

$$MMACS = \frac{\text{Clock speed (MHz)} \times \text{Number of processor cores}}{1 \text{ Clock cycle}} \quad (2.16)$$

Generally, the MMACS processor benchmark could indicate the speed of a particular processor. MMACS does not take into account the execution method and the different types of instructions among the different controllers. As can be seen from (2.16), the MMACS benchmark is directly proportional to processor clock speed. A low-cost implementation method is discussed in Chapter 3 in more detail.

## 2.10. Conclusion

Power electronics converters present unique challenges as hybrid systems that are inherently non-linear and use high switching frequencies. This chapter explained the general principles of MPC and how they apply to power converter analysis. A detailed step-by-step procedure on constructing the state variable model estimators, formulating the MPC cost function, and the cost function optimization was discussed. Some of the challenges with high switching frequency may require an addition of a modulator as has been considered. Additionally, the application of MPC using low-cost implementation methods is of interest and has been discussed in this chapter. The foundations established in this chapter are used in the following application chapters:

Chapter 3 – Maximum power point tracking of standalone dc power optimizers

- MPC-based sensorless current mode
- MPC-based adaptive perturbation MPPT

Chapter 4 – Maximum power point in a grid-interactive inverter – sub-multilevel inverter

- MPC based submodule MPPT converters for partial shading mitigation

- MPC based grid integration based on sub-multilevel inverter

#### Chapter 5 Maximum power point in a grid-interactive inverter – impedance source inverter

- MPC based MPPT control of a single-stage power processing systems
- MPC based MPPT integration with pre-existing PID based controller

#### Chapter 6 Double frequency power ripple controller for microinverters

- MPC-based control strategy for double frequency ripple on dc-link voltage reduction in microinverters
- Integrated multi-objective MPC controller for both grid current injection and dc-link voltage control



### 3. MAXIMUM POWER POINT TRACKING IN DC POWER OPTIMIZERS\*

#### 3.1. Introduction

Solar photovoltaic energy systems (PV) has had a consistently increasing market penetration over the past seven years, with a total global installed capacity of over 500 GW [8]. A PV installation must harvest the maximum possible electrical energy at the lowest cost to be economically justifiable [9, 10]. This presents many engineering challenges and opportunities within power electronics [11] amongst which are low-cost

---

\*Part of the data reported in this chapter is reprinted with permission from “MPPT of Photovoltaic Systems Using Sensorless Current-Based Model Predictive Control” by M. Metry, M. Shadmand, R. S. Balog, and H. Abu-Rub, 2017. IEEE Trans. Ind. Appl., vol. 53, pp. 1157-1167, Copyright © 2017 IEEE

\*Part of the data reported in this chapter is reprinted with permission from “A Model Parity Study on the Model Predictive Control Based Sensorless Current Mode” by M. Metry and R. S. Balog, 2018. Presented at the IEEE Int. Conf. on Compatibility, Power Electron. and Power Eng. Doha, Qatar, 10-12 Apr 2018, pp. 1-6, Copyright © 2018 IEEE

\*Part of the data reported in this chapter is reprinted with permission from “A Parameter Mismatch Study on Model Predictive Control Based Sensorless Current Mode” by M. Metry and R. S. Balog, 2018. presented at the IEEE Texas Power and Energy Conf. (TPEC), College Station, TX, 8-9 Feb 2018, pp. 1-6, Copyright © 2018 IEEE

\*Part of the data reported in this chapter is reprinted with permission from “A Variable Step-Size MPPT for Sensorless Current Model Predictive Control for Photovoltaic Systems” by M. Metry, M. B. Shadmand, R. S. Balog, and H. Abu-Rub, 2016. Presented at the IEEE Energy Convers. Congr. and Expo. (ECCE), Milwaukee, WI, 18-22 Sep 2016, p. 1-8, Copyright 2016 by IEEE

\*Part of the data reported in this chapter is reprinted with permission from “High efficiency MPPT by model predictive control considering load disturbances for photovoltaic applications under dynamic weather condition” by M. Metry, M. B. Shadmand, R. S. Balog, and H. Abu-Rub, 2015. Presented at the 41st Annual Conference of the IEEE Industrial Electronics Society, IECON 2015, Yokohama, Japan, 2015, pp. 4092-4097, Copyright © 2015 IEEE

\*Part of the data reported in this chapter is reprinted with permission from “Maximum power point tracking of photovoltaic systems using sensorless current-based model predictive control” by M. Metry, M. B. Shadmand, Yushan Liu, R. S. Balog and H. Abu Rub, 2015. Presented at the IEEE Energy Conversion Congress and Exposition (ECCE), Montreal, Quebec, 2015, pp. 6635-6641, Copyright 2020 © 2015 IEEE

\*Part of the data reported in this chapter is reprinted with permission from “Sensitivity analysis to model parameter errors of MPPT by model predictive control for photovoltaic applications” by M. Metry, M. B. Shadmand, R. S. Balog and H. Abu Rub, 2015. IEEE First Workshop on Smart Grid and Renewable Energy (SGRE), Doha, Qatar, 2015, pp. 1-6, Copyright © 2015 IEEE

power converter implementation [12], high reliability [13], grid-friendly integration [14], fast dynamic response to track the stochastic nature of the solar resource [15, 16], and disturbance rejection to grid transient [17, 18] and partial shading [19]. Maximum power point tracking (MPPT) is needed to achieve high-efficiency PV systems [88, 89].

This chapter utilizes the model-based framework of MPC to develop a MPPT algorithm that eliminates the input-side current sensor in a PV application. The implementation of MPC realizes the observer-based SCM being fundamentally model-based design, expressed within the cost function [90]. This chapter also utilizes constrained control and online auto-tuning of MPC to develop an adaptive perturbation MPPT to reduce steady-state oscillation and improve dynamic performance. The contribution of this chapter is that the observer model for the sensorless-current control and the adaptive perturbation MPPT are incorporated directly into the MPC formulation.

This chapter is organized as follows:

Section 3.2 introduces some of the challenges with maximum power point tracking.

Section 3.3 presents the background on the flyback converter with detailed circuit analysis.

Section 3.4 derives the MPC formulation.

Section 3.5 presents simulation results including dynamic standardized tests, a model parameter mismatch study and a model parity study.

Section 3.6 presents detailed experimental results analyzed in light of NREL data, and a comparative study to another well-known MPPT technique.

Section 3.7 details a low cost microcontroller implementation of the MPC based MPPT technique.

Section 3.8 concludes the contribution of this chapter.

### **3.2. Maximum power point tracking**

The MPPT subject has been well studied for PV applications and many control algorithms are known [24, 91, 92]. These include perturb and observe (P&O), incremental conductance (InCon), and fractional open circuit [31]. P&O and InCon attempt to track the maximum power point (MPP) by incrementing a reference signal (voltage or current) until the system reaches the MPP [93]. These techniques may exhibit large output power oscillations around the MPP and slow settling time in response to step changes [93-95].

A challenge with some well-known MPPT techniques is their dependency on accurate PV current measurement [96]. Specifications for temperature drift and aging-related drift in shunt-resistor sensor and current transducer measurements can be found in the respective datasheets [97, 98]. Accuracy of the current measurement using a hall-effect sensor is influenced by the position of the conductor within the sensor [99]. Hall effect-based sensor measurements may be compromised due to magnetic core offset [100] and magnetic interference from the surrounding environment [99, 101]. Merits of other contactless current sensor technologies such as anisotropic magneto-resistive effect based sensors and tunnel magneto-resistive effect based sensors are discussed [100, 101].

Sensorless current mode control (SCM) in power converters is a way to eliminate challenges of the current sensor [102]. Techniques for the MPPT application are discussed [102-106]. An observer-based model approach to SCM as a surrogate to the current measurement is discussed [102]. Estimation of the current using capacitor voltage ripple

is discussed [103, 104]. Solutions involving the use of the transcendental relations of the PV cell to attain MPP, using a voltage sensor are demonstrated [105, 106]. The observer-based SCM approach shows sizeable benefits on noise performance and load range [107] when compared to other known current-mode techniques [102]. Eliminating the current sensor, a fundamental component of the circuit, can reduce the cost and improves the reliability of the PV system especially when the system involves a cascaded or a multi-level topology [108].

Finite control set model predictive control (MPC) is a flexible model-based [36] control method that can include multi-objective optimization [37], constrained control [38], adaptive control [39] and online auto-tuning of weighting factors [40] all in a single controller that exhibits fast dynamic tracking [41]. Sensorless current tracking of the maximum power point, has been shown to alleviate the temperature and aging drift of the sensor. In this chapter, experimental results of the proposed algorithm were presented and compared to other well-known MPPT algorithms. The proposed algorithm showed good reference tracking with fast dynamic response and small ripple in steady-state. A study of parameter mismatch has demonstrated that the model-based design functions at high efficacy within a wide mismatch range. A model parity study of the current surrogate model has shown the fidelity of the proposed observer based technique. Dynamic testing of the proposed algorithm has shown fast tracking and robustness to disturbance. The formulation of the proposed ASC-MPPT, applied to a flyback converter, is explained and demonstrated experimentally on a PV system using actual meteorological data. However, the technique can be applied to other converter topologies by merely modifying the MPC

equations. The EN50530 European industrial test standards were used to demonstrate performance. Finally, the proposed algorithm has been implemented on a low cost microcontroller unit which presents a step closer to wide-scale production.

### 3.3. Background on the flyback converter topology

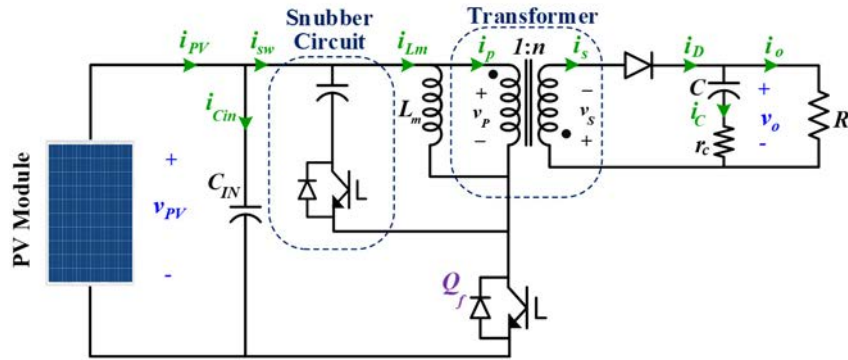


Figure 3.1 The flyback converter topology with snubber circuit for PV application.

An overview of the proposed ASC-MPPT for the flyback converter is demonstrated in Figure 3.1. The flyback converter is presented in this chapter for illustration as it provides electrical isolation, making it suitable for local-area dc micro-grid use [109, 110]. Also, the low component count and low cost supplemented with a high voltage gain make it suitable for PV module-integrated topologies [111, 112].

### 3.3.1. Circuit analysis

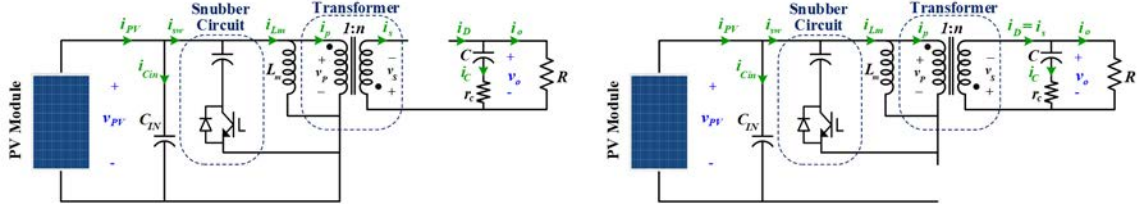


Figure 3.2 The flyback converter configuration when  $Q_f$  is turned on,  $\sigma=1$  (left), and when  $Q_f$  is turned off,  $\sigma=0$  (right).

Consider the flyback converter in Figure 3.1. Discontinuous conduction mode (DCM) maximizes the ripple PV current; hence, the flyback converter is analyzed in continuous conduction mode (CCM). The state equations are derived based on the switching of the converter: when the switch is closed ( $\sigma = 1$ ) and when the switch is open ( $\sigma = 0$ ) as shown in Figure 3.2.

$$i_c^{\sigma=1}(t) = C \frac{dv_o}{dt} = -i_o(t) = \frac{-v_o(t)}{R} \quad (3.17)$$

$$i_c^{\sigma=0}(t) = C \frac{dv_o}{dt} = i_D - i_o = \frac{i_{Lm}(t)}{n} - \frac{v_o(t)}{R} \quad (3.18)$$

$$v_{Lm}^{\sigma=1}(t) = L_m \frac{di_{Lm}}{dt} = v_{PV}(t) \quad (3.19)$$

$$v_{Lm}^{\sigma=0}(t) = L_m \frac{di_{Lm}}{dt} = \frac{-v_o(t)}{n} \quad (3.20)$$

The discrete-time estimation of (3.17)-(3.20) in steady-state is found using the Euler forward method for discretization.

$$\tilde{v}_o^{\sigma=1}(k+1) = \left(1 - \frac{T_s}{RC}\right) v_o(k) \quad (3.21)$$

$$\tilde{v}_o^{\sigma=0}(k+1) = \left(1 - \frac{T_s}{RC}\right) v_o(k) + \frac{T_s}{nC} i_{Lm}(k) \quad (3.22)$$

$$\tilde{i}_{Lm}^{\sigma=1}(k+1) = \frac{T_s}{L_m} v_{PV}(k) + i_{Lm}(k) \quad (3.23)$$

$$\hat{i}_{Lm}^{\sigma=0}(k+1) = \frac{-T_s}{nL_m} v_o(k) + i_{Lm}(k) \quad (3.24)$$

The magnetizing current can be expressed in terms of PV voltage and output voltage.

$$i_{Lm}^{\sigma=1}(t) = i_{PV}(t) - i_{Cin}(t) = i_{PV}(t) - C_{in} \frac{dv_{PV}}{dt} \quad (3.25)$$

$$i_{Lm}^{\sigma=0}(t) = ni_D(t) = n(i_o(t) - i_C(t)) = \frac{n}{R} v_o(t) - nC \frac{dv_o}{dt} \quad (3.26)$$

The discrete-time estimation of (3.25)-(3.26) in steady-state is found using the Euler backward method for discretization.

$$i_{Lm}^{\sigma=1}(k) = i_{PV}(k) - \frac{C_{in}}{T_s} (v_{PV}(k) - v_{PV}(k-1)) \quad (3.27)$$

$$i_{Lm}^{\sigma=0}(k) = \frac{n}{R} v_o(k) - \frac{nC}{T_s} (v_o(k) - v_o(k-1)) \quad (3.28)$$

Using equations (3.17) to (3.28) directly for MPPT implementation would require multiple sensors for the PV voltage, PV current and the output voltage. Without loss of generality, the load R in the expressions (3.17)-(3.28) could represent a model-based expression for any load-side connected component, as discussed in [113, 114].

### 3.3.2. Steady-state averaging

Assuming steady-state operation, the output voltage is related to the PV voltage.

$$V_o = V_{PV} \frac{nD}{1-D}, \text{ where } D = \frac{t_{\sigma=1}}{T_s} \quad (3.29)$$

The magnetizing current is related to the diode current by the transformer's turns ratio.

Hence, the expression of average  $i_{LM}$  is

$$I_{Lm}(t) = \frac{n V_o}{R(1-D)} \quad (3.30)$$

Relations (3.29) and (3.30) are applied to (3.21) and (3.22) to estimate the PV voltage at the next step, assuming that the PV voltage remains constant throughout the sampling period  $T_s$ .

$$\tilde{v}_{pV}^{\sigma=1}(k+1) = \left(\frac{1-D}{nD}\right) \left[1 - \frac{T_s}{RC}\right] v_o(k) \quad (3.31)$$

$$\tilde{v}_{pV}^{\sigma=0}(k+1) = \left(\frac{1-D}{nD}\right) \left[1 - \frac{T_s}{RC} + \frac{T_s}{RC(1-D)}\right] v_o(k) \quad (3.32)$$

### 3.4. The MPC formulation

#### 3.4.1. MPC implementation to the flyback converter

The proposed ASC-MPPT algorithm uses an observer model as a surrogate for the sensor measurement of current. Hence, the surrogate model is an estimated variable in the form  $\tilde{x}(k)$  and can be written as  $\tilde{i}_{pV}(k)$ . This estimate is used along with the measurements:  $v_{pV}(k)$  and  $v_o(k)$  to estimate the PV voltage state variable,  $\tilde{v}_{pV}(k+1)$ , at the next sampling time. The optimization process determines the appropriate actuation that will minimize the cost function in (3.33).

$$\begin{aligned} \min_{g_{\sigma \in \{0,1\}}} &= |\tilde{v}_{pV}^{\sigma}(k+1) - v_{pV.ref}^*(k)| \\ \text{subject to } &\tilde{v}_{pV}^{\sigma=1}(k+1) = \left(\frac{1-D}{nD}\right) \left[1 - \frac{T_s}{RC}\right] v_o(k) \\ &\tilde{v}_{pV}^{\sigma=0}(k+1) = \left(\frac{1-D}{nD}\right) \left[1 - \frac{T_s}{RC} + \frac{T_s}{RC(1-D)}\right] v_o(k) \end{aligned} \quad (3.33)$$

#### 3.4.2. MPC based load prediction

A drawback of model-based relations is its dependence on the system model parameters. Generally, load resistance ( $R$ ) is variable and sudden unpredicted perturbation in the load can render the full system unstable. Hence, a simple, yet effective solution is



proposed to provide better monitoring on the load using an observer-based approach, without PV current measurement. The proposed algorithm uses only the already existing sensors for the PV and the output capacitor voltages. Model relations for the load value can be inferred using the same flyback converter model (Figure 3.1). The relation between PV current and load current is given by:

$$i_o = i_{PV} \left( \frac{1-D}{D} \right) \frac{1}{n} \quad (3.34)$$

The resistive load observer model is given by:

$$\gamma = R(k) = \frac{v_c}{i_o} = \frac{v_c(k)}{i_{PV}(k) \left( \frac{1-D}{D} \right) \frac{1}{n}} \quad (3.35)$$

which can be used to improve the robustness of the system to load parameter mismatch of the system and is applied to the predictive model of the system in (3.31) and (3.32).

### 3.4.3. MPC based maximum power point tracking

MPC-MPPT relied on a parallel InCon or P&O algorithm to determine  $v_{PV,ref}^*(k)$  in (3.33). The sign of the expression  $\Delta i_{PV} / \Delta v_{PV}$  is used to determine the reference value  $v_{PV,ref}^*(k)$  as is shown in (3.36).

$$v_{PV,ref}^*(k) = \begin{cases} v_{PV}(k) - |\Delta \tilde{v}|, \mu < 0 \\ v_{PV}(k) + |\Delta \tilde{v}|, \mu > 0 \end{cases} \quad \text{for } \mu = \frac{i_{PV}(k) - i_{PV}(k-1)}{v_{PV}(k) - v_{PV}(k-1)} \quad (3.36)$$

where  $|\Delta \tilde{v}|$  is the perturbation size of the MPPT algorithm. The details on obtaining an estimate for  $i_{PV}$  and the details on estimating  $|\Delta \tilde{v}|$  are explained in later sections. Based on (3.36) the MPPT can be expressed within the MPC cost function as illustrated in (3.37).

$$\begin{aligned}
\min_{g_{\sigma \in \{0,1\}}} &= |\tilde{v}_{PV}^{\sigma}(k+1) - v_{PV.ref}^*(k)| \\
\text{subject to } & \tilde{v}_{PV}^{\sigma=1}(k+1) = \left(\frac{1-D}{nD}\right) \left[1 - \frac{T_s}{\gamma C}\right] v_o(k) \\
& \tilde{v}_{PV}^{\sigma=0}(k+1) = \left(\frac{1-D}{nD}\right) \left[1 - \frac{T_s}{\gamma C} + \frac{T_s}{\gamma C(1-D)}\right] v_o(k) \\
\text{where, } & v_{PV.ref}^*(k) = \begin{cases} v_{PV}(k) - |\Delta\tilde{v}|, \mu < 0 \\ v_{PV}(k) + |\Delta\tilde{v}|, \mu > 0 \end{cases} \text{ for } \mu = \frac{i_{PV}(k) - i_{PV}(k-1)}{v_{PV}(k) - v_{PV}(k-1)}
\end{aligned} \tag{3.37}$$

where  $v_{PV.ref}^*(k)$  is the MPPT reference. For this case, since there is only one penalty function in the MPC cost function, the weight factor  $\lambda=1$ .

#### 3.4.4. MPC sensorless current mode

An observer model for the PV current can be obtained by analyzing the converter (Figure 3.2) in continuous conduction mode during the two switching states  $\sigma \in \{0,1\}$ . Using Kirchoff's current law when the primary switch is closed ( $\sigma = 1$ ), the input capacitor current  $i_{Cin}(t)$  can be written as

$$i_{Cin}(t) = i_{PV}(t) - i_{sw}(t) \tag{3.38}$$

As the primary switch is closed, the snubber switch is open. Hence,  $i_{sw}(t) = i_{LM}(t)$ . Then  $i_{PV}(t)$  can be written as

$$i_{Cin}(t) = \frac{dv_{PV}(t)}{dt} = i_{PV}(t) - i_{LM}(t) \tag{3.39}$$

When the primary switch is open ( $\sigma = 0$ ), the snubber switch is closed to provide a freewheeling path for the magnetizing current. Hence,  $i_{sw} = 0$  and  $i_{Cin}(t)$  can be written as

$$i_{Cin}(t) = \frac{dv_{PV}(t)}{dt} = i_{PV}(t) \tag{3.40}$$

The PV current can be written as a function of the switching state  $\sigma \in \{0,1\}$  as

$$i_{PV}(t) = \frac{dv_{PV}(t)}{dt} + \sigma i_{LM}(t) \tag{3.41}$$

As the change in PV current is relatively slower than the sampling time of the MPC sampling time, the expression  $\sigma i_{LM}(t)$  can be approximated as

$$\sigma i_{LM}(t) \approx DI_{LM} \quad (3.42)$$

Substituting (3.30) and (3.42) into (3.41), an expression for the PV current is

$$i_{PV}(t) = \frac{nD}{(1-D)\gamma} v_o(t) + C_{IN} \frac{dv_{PV}(t)}{dt} \quad (3.43)$$

The discrete-time estimation of (3.43) in steady-state is found using the Euler backward method for discretization

$$\tilde{i}_{PV}(k) = \frac{nD}{(1-D)\gamma} v_o(k) + \frac{C_{IN}}{T_s} (v_{PV}(k) - v_{PV}(k-1)) \quad (3.44)$$

where  $T_s$  is the sampling period of the MPC; hence, (3.44) is used as an observer model for PV current to eliminate the current sensor. SCM is shown to be based on the model-based design principle, which integrates within the MPC framework as in (3.45).

$$\begin{aligned} \min_{g_{\sigma \in \{0,1\}}} &= |\tilde{v}_{PV}^{\sigma}(k+1) - v_{PV.ref}^*(k)| \\ \text{subject to} & \quad \tilde{v}_{PV}^{\sigma=1}(k+1) = \left(\frac{1-D}{nD}\right) \left[1 - \frac{T_s}{\gamma C}\right] v_o(k) \\ & \quad \tilde{v}_{PV}^{\sigma=0}(k+1) = \left(\frac{1-D}{nD}\right) \left[1 - \frac{T_s}{\gamma C} + \frac{T_s}{\gamma C(1-D)}\right] v_o(k) \\ & \quad \tilde{i}_{PV}(k) = \frac{nD}{(1-D)\gamma} v_o(k) + \frac{C_{IN}}{T_s} (v_{PV}(k) - v_{PV}(k-1)) \\ \text{where,} & \quad v_{PV.ref}^*(k) = \begin{cases} v_{PV}(k) - |\Delta\tilde{v}|, \mu < 0 \\ v_{PV}(k) + |\Delta\tilde{v}|, \mu > 0 \end{cases} \quad \text{for } \mu = \frac{\tilde{i}_{PV}(k) - \tilde{i}_{PV}(k-1)}{v_{PV}(k) - v_{PV}(k-1)} \end{aligned} \quad (3.45)$$

### 3.4.5. MPC adaptive cost function

The predictive control based MPPT methods in [36, 114-117] have shown dynamic performance improvement by reducing rising and settling times using ahead of time next step predictions. These improvements, however, were achieved using fixed step perturbation, which could be a hindrance to the performance of any MPPT method,

including the predictive control-based methods. Such problems include over-stepping during steady-state, causing a high ripple, and under-stepping during a transient leading to a slower rising time. While the status of the system, transient or steady-state, is primarily dependent on ambient conditions, obtaining a measurement of irradiance is not feasible and is costly. Hence, the MPPT perturbation size estimate needs to be determined without resorting to irradiance sensors. This section demonstrates the feasibility of implementing an adaptive perturbation MPPT using the MPC cost function.

To appropriately obtain an estimate of the MPPT step size, the average PV voltage value  $\tilde{v}_{pv,ave}(k+1)$ , which is the average predicted voltage over the whole period of the switching action when the switch is on and when in its off, is compared with the present time PV voltage  $v_{pv}(k)$ :

$$|\Delta\tilde{v}| = |\tilde{v}_{pv,ave}(k+1) - v_{pv}(k)| \quad (3.46)$$

where,  $\tilde{v}_{pv,ave}(k+1) = \frac{1}{2}(\tilde{v}_{pv}^{\sigma=0}(k+1) + \tilde{v}_{pv}^{\sigma=1}(k+1))$

The sign of the expression  $\Delta i_{PV}/\Delta v_{PV}$  is used to determine the reference value  $v_{PV,ref}^*(k)$  in (3.45) as is shown in (3.47).

$$v_{PV,ref}^*(k) = \begin{cases} v_{pv}(k) - |\Delta\tilde{v}|, \mu < 0 \\ v_{pv}(k) + |\Delta\tilde{v}|, \mu > 0 \end{cases} \text{ for } \mu = \frac{\tilde{i}_{PV}(k) - \tilde{i}_{PV}(k-1)}{v_{PV}(k) - v_{PV}(k-1)} \quad (3.47)$$

Combining equations (3.45), (3.46) and (3.47) along with the knowledge of cost function weighting factors in MPC, as mentioned earlier, an adaptive MPC cost function is formulated in (3.48).

$$g_{\sigma \in \{0,1\}} = \lambda_1 \left| \tilde{v}_{PV}^{\sigma}(k+1) - v_{PV}(k) + |\tilde{v}_{PV,ave}(k+1) - v_{PV}(k)| \right| + \lambda_2 \left| \tilde{v}_{PV}^{\sigma}(k+1) - v_{PV}(k) - |\tilde{v}_{PV,ave}(k+1) - v_{PV}(k)| \right| \quad (3.48)$$

$$\text{where, } \{\lambda_1, \lambda_2\} = \begin{cases} \{1,0\}, \mu < 0 \\ \{0,1\}, \mu > 0 \end{cases} \text{ for } \mu = \frac{\tilde{i}_{PV}(k) - \tilde{i}_{PV}(k-1)}{v_{PV}(k) - v_{PV}(k-1)}$$

The overall cost function encompasses the sensorless current mode, converter discrete-time modeling, adaptive perturbation, and MPPT functionalities within one integrated objective function, as shown in (3.49). The detailed control implementation is detailed in the flowchart Figure 3.3 and in the block diagram Figure 3.4.

$$\begin{aligned} \min g_{\sigma \in \{0,1\}} &= \lambda_1 \left| \tilde{v}_{PV}^{\sigma}(k+1) - v_{PV}(k) + |\tilde{v}_{PV,ave}(k+1) - v_{PV}(k)| \right| \\ &+ \lambda_2 \left| \tilde{v}_{PV}^{\sigma}(k+1) - v_{PV}(k) - |\tilde{v}_{PV,ave}(k+1) - v_{PV}(k)| \right| \\ \text{subject to } \tilde{v}_{PV}^{\sigma=1}(k+1) &= \left( \frac{1-D}{nD} \right) \left[ 1 - \frac{T_s}{\gamma C} \right] v_o(k) \\ \tilde{v}_{PV}^{\sigma=0}(k+1) &= \left( \frac{1-D}{nD} \right) \left[ 1 - \frac{T_s}{\gamma C} + \frac{T_s}{\gamma C(1-D)} \right] v_o(k) \\ \tilde{i}_{PV}(k) &= \frac{nD}{(1-D)\gamma} v_o(k) + \frac{C_{IN}}{T_s} (v_{PV}(k) - v_{PV}(k-1)) \\ \text{where, } \{\lambda_1, \lambda_2\} &= \begin{cases} \{1,0\}, \mu < 0 \\ \{0,1\}, \mu > 0 \end{cases} \text{ for } \mu = \frac{\tilde{i}_{PV}(k) - \tilde{i}_{PV}(k-1)}{v_{PV}(k) - v_{PV}(k-1)} \end{aligned} \quad (3.49)$$

A comparison is made in Table 3.1 based on the review paper [31] to provide a better perspective on the characteristics of ASC-MPPT relevant to other known MPPT techniques. ASC-MPPT is not dependent on PV array parameters, requires no periodic tuning and only senses PV voltage, yet it converges to true MPP at a high convergence speed.

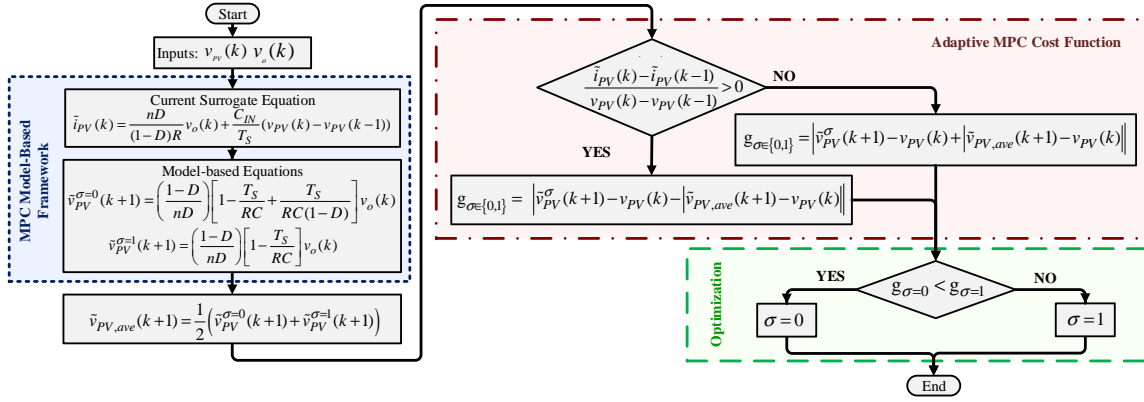


Figure 3.3 A flowchart of the proposed ASC-MPPT algorithm showing the control sequence of the proposed integrated MPC cost function.

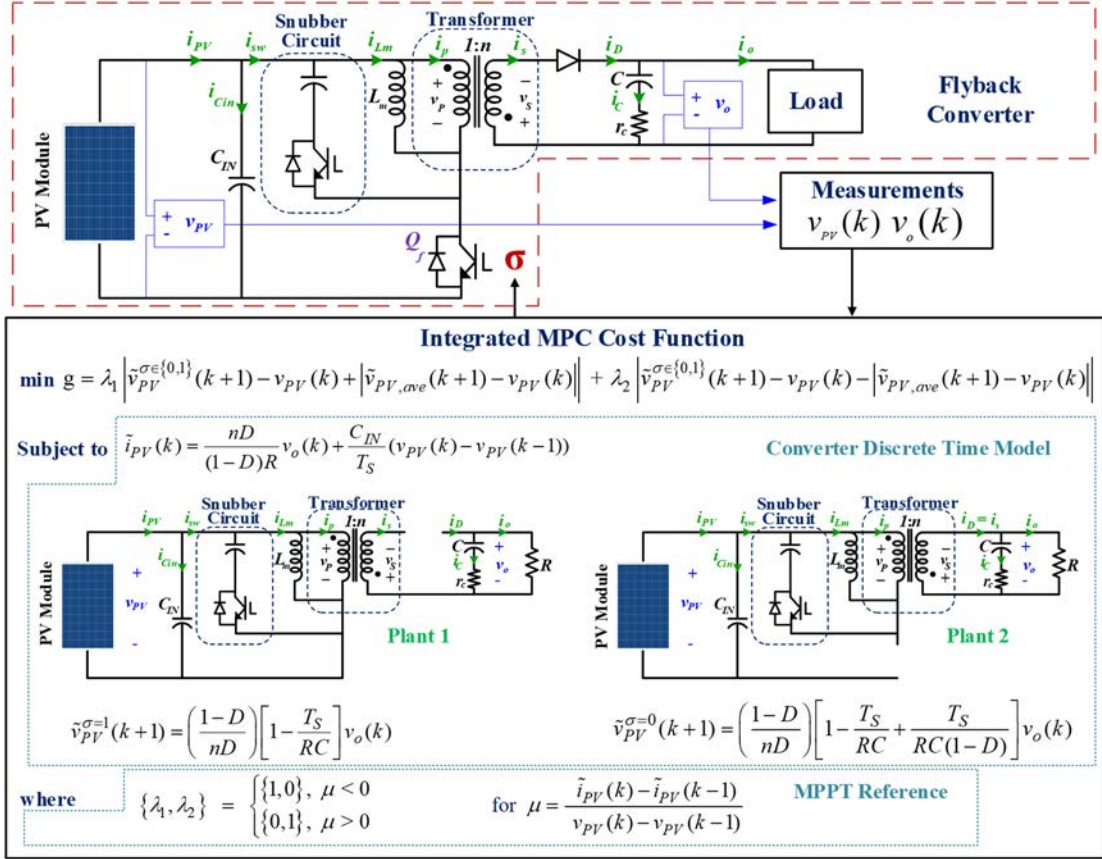


Figure 3.4 The flyback converter with snubber circuit for PV application and a detailed block diagram of the proposed ASC-MPPT algorithm.

Table 3.1 Major characteristics comparison of ASC-MPPT with other well-known MPPT techniques and a few more advanced algorithms.

Ref	MPPT Technique	PV Array Dependent?	True MPPT?	Analog Digital?	Perturbation	Convergence Speed	Implementation Complexity	Computational Loops	Sensed Parameters
[118]	Hill-climbing/P&O	No	Yes	Both	Fixed	Varies	Low	MPPT	V,I
[119]	Incremental Conductance	No	Yes	Digital	Fixed	Varies	Medium	MPPT	V,I
[120]	Fractional Voc	Yes	No	Both	Fixed	Medium	Low	MPPT	V
[121]	Fractional Isc	Yes	No	Both	Fixed	Medium	Medium	MPPT	I
[92]	Sliding Mode MPPT	No	Yes	Digital	Fixed	High	High	Voltage, MPPT	V,I
[122]	Adaptive P&O	No	Yes	Both	Variable	High	Medium	MPPT	V,I
[123]	Lock-In Amplifier	No	Yes	Digital	None	High	High	MPPT	V,I
Proposed Method	ASC-MPPT	No	Yes	Digital	Variable	High	High	Current, MPPT	Voltage

### 3.5. Simulation

#### 3.5.1. The real time simulation setup

The SUNPOWER SPR-305-WHT is used as PV module model. The PV module characteristics under standard test condition (STC: solar irradiance = 1 kW/m<sup>2</sup>, cell temperature = 25 deg. C) are tabulated in Table 2.1. Two modules are connected in parallel with the string I-V and P-V characteristics illustrated in Table 2.1. The control algorithm is implemented in Matlab/Simulink; the sampling time  $T_s$  is 10  $\mu$ s which corresponds to a sampling frequency of 100 kHz. This sampling time is chosen based on the capability of the dSPACE DS1007 platform processor which is used for real-time simulations in this chapter. Based on dSPACE implementation, the execution time for the proposed ASC-MPPT was found to be 8  $\mu$ s. dSPACE was used in this chapter for expedited prototyping; however, readily available and low priced microprocessors, such as the Altera DEO-Nano FPGA, are capable of handling the controller's execution time for the real application. In a fixed step model predictive control, unlike controllers with a pulse-width modulator, the switching signals are directly manipulated, thus the "switching frequency" can vary from one fixed sampling interval to the next. The sampling frequency should be much higher

than the switching frequency in order to get a good performance controller, such as 20 times higher according to the guidelines for accurate modeling of power electronics [124]. For well-behaved MPC systems, we can compute an “average switching frequency” which may offer some insight into the operation of other aspects of the system. In this chapter, the sampling frequency is 100 kHz which results in an average switching frequency of 5 kHz.

Table 3.2 Simulation model parameter table

System Model Parameter Table	
Average Switching Frequency (F)	5 kHz
Sampling Time (T <sub>s</sub> )	10 μs
Load Value (R)	10 ohm
Output Capacitor (C)	470 μF
Open-circuit voltage (V <sub>OC</sub> )	64.2 V
Short-circuit current (I <sub>SC</sub> )	5.96 A
Voltage at MPP (V <sub>MP</sub> )	54.7 V
Current at MPP (I <sub>MP</sub> )	5.58 A

### 3.5.2. Step response and dynamic response results

Using dSPACE DS1007 platform, a real time simulation of the proposed controller is examined under three test conditions: transient change in solar irradiance level, real sky condition, step change response to solar irradiance level, and performance evaluation in steady state condition. In the first experimental verification, the solar irradiance level was initially 750 W/m<sup>2</sup> then gradually decreased to 500 W/m<sup>2</sup> like the ramp rate in standard EN 50530 test. Figure 3.5 shows the performance of the proposed ASC-MPPT for this experiment; as it is shown the controller accurately tracks the MPP with average efficacy of 99.4%.



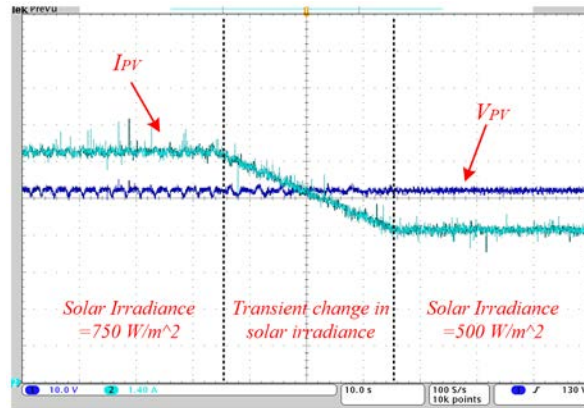


Figure 3.5 PV current and voltage under gradual change in solar irradiance.

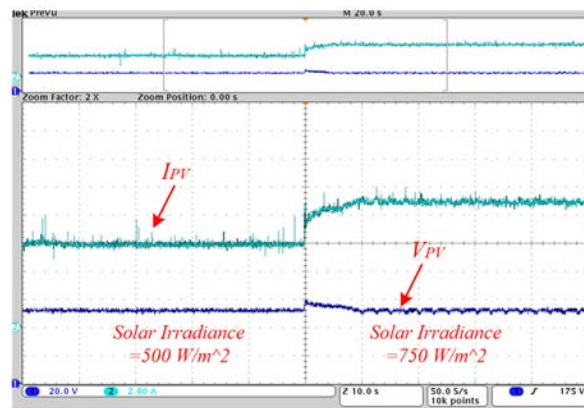


Figure 3.6 PV current and voltage under step change in solar irradiance level.

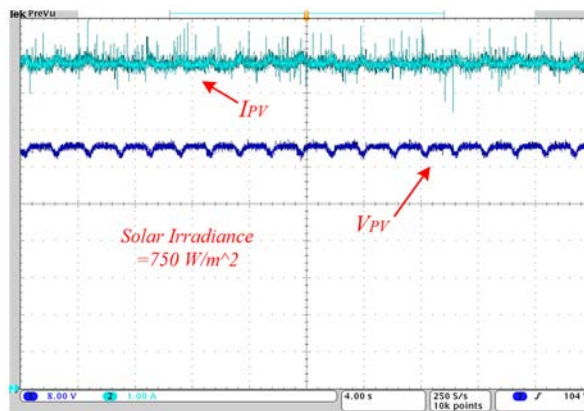


Figure 3.7 PV current and voltage ripple at 750 W/m<sup>2</sup> solar irradiance level.

The second experiment, Figure 3.6, verifies the stability and fast dynamic response of the ASC-MPPT to step change in solar irradiance level from 500 W/m<sup>2</sup> to 750 W/m<sup>2</sup>. Finally, the steady state performance at 750 W/m<sup>2</sup> of the proposed technique is shown in Figure 3.7. As shown the oscillation around MPP is negligible with PV voltage and current ripple of 3.556% and 2.353% respectively.

### 3.5.3. The EN50530 test standard

Performance evaluations of MPPT techniques depend largely on the test being conducted. Different literature suggests different test types like step changes. While, such tests may prove the effectiveness of the system, they fail to follow a standardized acceptance [125]. Therefore, using a globally accepted test for MPPT is essential to evaluate a system's performance.

To overcome the inconsistency in performance tests, an international working group was set up in late 2006 to develop a standardized test that takes into account both MPPT accuracy and conversion efficiency [125]. The test was accepted as a standard in the European Union by the end of 2009 and published as The Standard EN 50530 Test [125].

The dynamic EN 50530 standard tests are run under rapidly changing weather conditions. It combines rising and falling ramp profiles with different slopes to represent irradiation levels [125]. The principle of the test sequence is illustrated in Figure 3.8 parametrically. The slope of each ramp is named  $\zeta_n$  which is incrementally increasing by a factor of  $\varepsilon$ , this sequence is repeated  $n$  times during the period under the test. The test is comprised of three components as in Figure 3.8: (A) Low to medium irradiation (150-

500W/m<sup>2</sup>), (B) medium to high irradiation (300-1000W/m<sup>2</sup>) and (C) startup and shutdown irradiation (2-100W/m<sup>2</sup>). Slopes for (A) vary from 0.5 W/m<sup>2</sup>/s to 50 W/m<sup>2</sup>/s, while slopes for (B) vary from 10 W/m<sup>2</sup>/s to 100 W/m<sup>2</sup>/s.

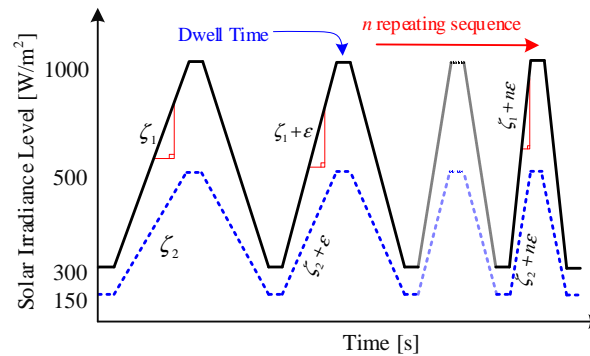


Figure 3.8 The EN 50530 test sequence used in this experiment is composed of two parts: 1- Medium to high solar irradiance level (black solid line) and 2- Low to medium solar irradiance level (blue dashed line).

### 3.5.4. EN50530 standardized test results

The EN 50530 test performance results for PV power, current and voltage are as shown in Figure 3.9, Figure 3.10 and Figure 3.11 respectively. While the overall test shows good MPP tracking, Figure 3.11 shows that the PV voltage deviates from its theoretical MPP value as the irradiance slopes become steeper. Such result motivates the model parity study performed later in 3.5.6.

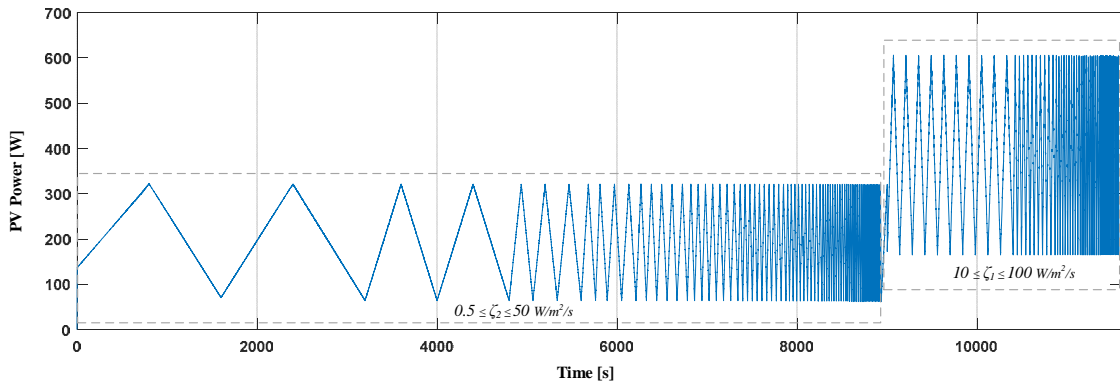


Figure 3.9 PV power under dynamic EN 50530 standard test.

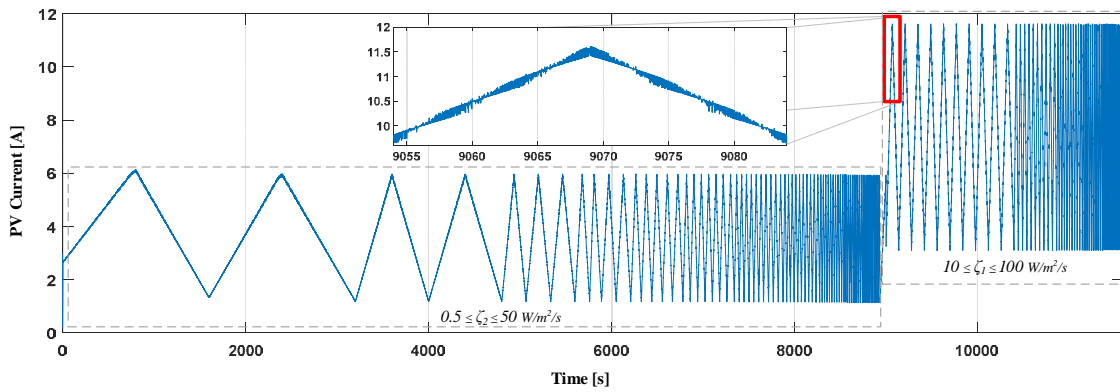


Figure 3.10 PV current under dynamic EN 50530 standard test.

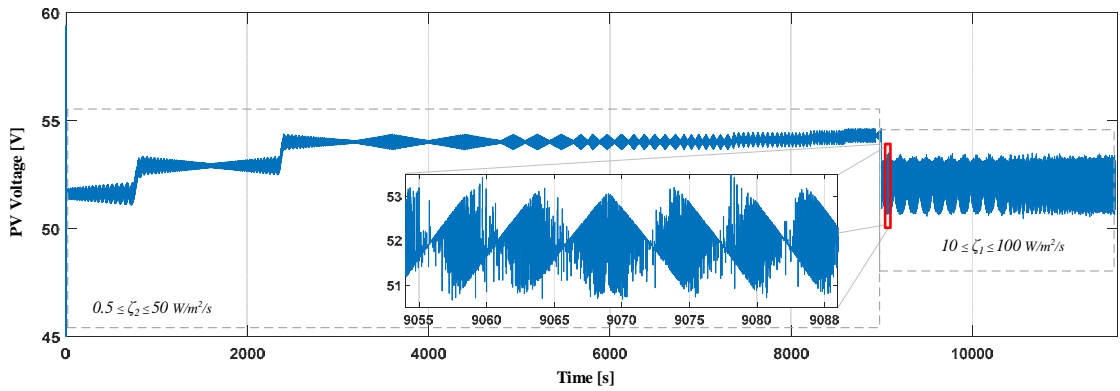


Figure 3.11 PV voltage under dynamic EN 50530 standard test.

### **3.5.5. Parameter mismatch study**

Modern controllers, particularly MPC that use model parameters in the optimization process, have the potential to be sensitive to parameter mismatch. Hence, the parity of such techniques could only be demonstrated through practical parameter mismatch analyses and control effectiveness results. Any system design is based on some nominal values and standard operation assumptions. For example, standard test conditions for a solar panel are  $1000 \text{ W/m}^2$  at  $25^\circ\text{C}$ ; however, the actual operation point will be different during the day. Similarly, the converter could be designed for a specific load, but load variability influences the performance of the system.

The parameter mismatch for the proposed algorithm is concerned with three different segments. First, the variability of the input parameter, solar irradiance as was discussed in the previous sections and in Figure 3.11. Second is the variability in the load. Third, is variability in the model. MPC performance depends on parameters in the circuit that cannot be monitored, yet change with time and usage. This includes the capacitor value and the equivalent series resistance.

#### **3.5.5.1. Output parameter mismatch**

According to Figure 3.12, the sensitivity of the system gets higher when the load mismatch is over 20% of the nominal value. This could be seen from (3.33), as the prediction model depends on value for  $R$ , the load. Hence, a prediction based on mismatching results, produces a lower control efficacy. This load may not be a simple resistor all the time, it could be a dc bus or a battery. Hence, a remedy to reduce such

sensitivity is to use an observer model, for the load, that is based on readily available measurements in the system, as has been proposed in [114].

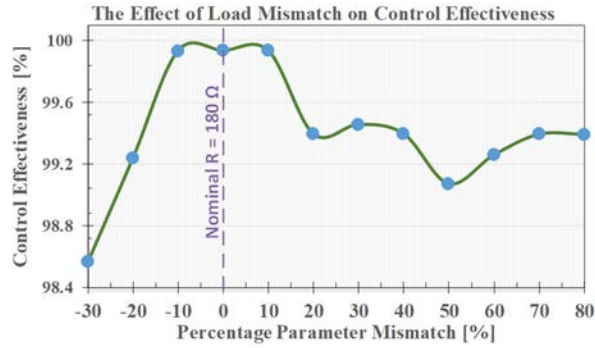


Figure 3.12 The control effectiveness of ASC-MPPT under load parameter mismatch.

### 3.5.5.2. Model parameter mismatch

The performance of any modern controller, like MPC, is as good as its model parity. The performance of the proposed ASC-MPPT algorithm depends on some parameters in the circuit that could not be monitored, yet they change with time and circuit operation modes. Model parameters that could vary are the capacitance value ( $C$ ) and its equivalent series resistance ( $ESR$ ) [77]. The capacitance is modeled as a model parameter in (3.31) and (3.32). However, the capacitance value changes as the capacitor ages. Also, some loads could add some capacitance in parallel; hence, altering the actual circuit capacitance and creating a model mismatch [77]. The capacitor modeled in the flyback circuit simulation is the 680  $\mu\text{F}$  Kemet capacitor with the part number [EST687M050AL8(1)]. The datasheet allows for a capacitance tolerance of 20%. In this study, the effect of a  $\pm 50\%$  parameter mismatch is observed. This means that the capacitance value could vary from 340  $\mu\text{F}$  to 1  $\text{mF}$ .

Similarly, the  $ESR$ , while not modeled in (3.31) and (3.32), has the effect of altering the load resistance. As could be inferred from Figure 3.12, the model is more sensitive to mismatch at lighter loads. The  $ESR$  of the capacitor of interest is valued at  $0.1 \Omega$ , according to the datasheet. In this study, a  $\pm 100\%$  parameter mismatch is observed. This means that  $ESR$  could vary from  $0 \Omega$  to  $0.2 \Omega$ .

The resulting control effectiveness from the parameter mismatch of  $C$  and  $ESR$  is shown in Figure 3.13. The vertical line that follows the nominal  $C$  value for varying  $ESR$ , indicates that the smaller the  $ESR$ , the better the performance of the proposed algorithm. High  $ESR$  values, increase the ripple on the output voltage, which is one of the important measurements in the model equations (3.31) and (3.32). The high voltage ripple in the output voltage, affects the parity of the measurement and hence increase the system's sensitivity to  $ESR$  mismatch.

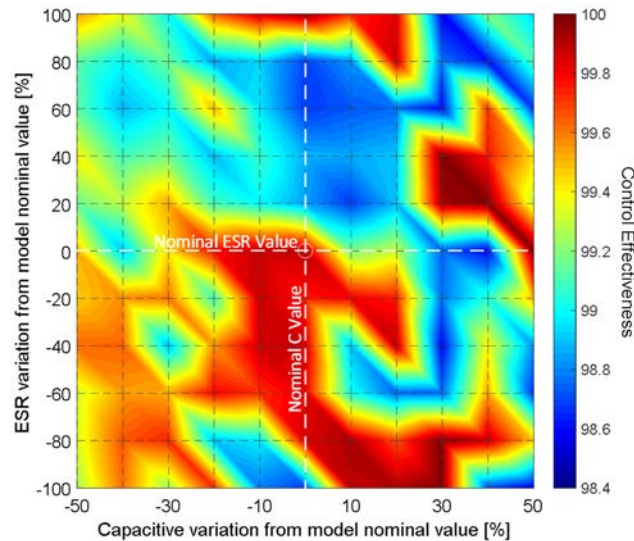


Figure 3.13 A model parameter mismatch, the output capacitance,  $C$  is tested for a mismatch of  $\pm 50\%$  of the nominal model value of  $C = 680 \mu F$ . The equivalent series resistance is tested for mismatch of  $\pm 50\%$  of the nominal datasheet value of  $ESR = 0.1 \Omega$ . The control effectiveness is recorded and statistically analyzed using a two-way ANOVA study.

The effect of the capacitor value mismatch on the system performance is not directly obvious. A larger capacitor size, in general, reduces the ripple on the output voltage measurement, hence improves the system performance. However, in this case the nominal  $C$  value is large, and hence the effect of  $C$  mismatch may not be inferred from Figure 3.13.

A better way to analyze the effect of the model sensitivity to  $C$  and  $ESR$  mismatch is through a two-way analysis of variance study (ANOVA). The two-way ANOVA compares the mean differences between two independent variables. By comparing the mean square sums of the variables by a Fisher's test ( $F$ -test), a  $p$ -value could be obtained [126]. In this study, it is assumed that a  $p$ -value of 0.05 differentiates the significance of the variables. In this case, the two factors are  $C$  and  $ESR$ .

The results of the two-way ANOVA study indicate that the  $p$ -value for  $C$  is 0.922 which is much larger than the significant  $p$ -value region of 0.05. Hence, it could be inferred that the capacitor size mismatch has no effect on the performance of the system in the study, if the  $p$ -value is 0.05.

On the other hand, the  $p$ -value for the  $ESR$  variable is 0.0376 which is smaller than 0.05. This indicates that the equivalent series resistor does worsen the system performance when varied if the  $p$ -value is 0.05. Another argument could be made for  $ESR$  being not significant for a smaller  $p$ -value. However, a  $p$ -value of 0.05 is the standard in engineering applications.



### 3.5.6. Model parity study

This section explores the parity of the current observer model by quantifying the current estimation error within the proposed algorithm. In this study, three different currents are considered: first, is the measured current ( $I_{\text{Measured}}$ ), which is the current measured at the PV side when the ASC-MPPT algorithm is running. The measured current is not used within the ASC-MPPT algorithm but is measured for evaluation purposes only. Second, is the estimated current ( $I_{\text{Estimated}}$ ), this is the observer model's estimation and is the surrogate to the measured current that is used to track the MPP in the ASC-MPPT algorithm. Finally, the MPP current ( $I_{\text{Theoretical}}$ ) is the theoretical current value that corresponds to specific irradiance values as determined from the PV module datasheet.

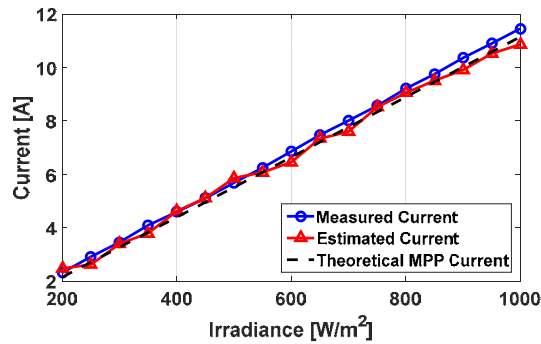


Figure 3.14 Measured current, observer-model estimated current and theoretical PV current compared for different irradiance values.

Throughout a range of irradiance values from 200 to 1000 W/m<sup>2</sup>, current values for  $I_{\text{Measured}}$ ,  $I_{\text{Estimated}}$ , and  $I_{\text{Theoretical}}$  are recorded and compared in Figure 3.14. The general pattern, seen in Figure 3.14, is  $I_{\text{Estimated}}$  tracks  $I_{\text{Theoretical}}$  for most of the irradiance values. However, there seems to be a steady-state error between  $I_{\text{Measured}}$  and  $I_{\text{Theoretical}}$ . This could also be seen clearly in error comparisons of Figure 3.15. Figure 3.15 (a), (b) and (c) show

$I_{\text{Estimated}} - I_{\text{Measured}}$ ,  $I_{\text{Estimated}} - I_{\text{Theoretical}}$  and  $I_{\text{Measured}} - I_{\text{Theoretical}}$  in amperes respectively. Based on those figures, it could be noted that the errors in Figure 3.15 (a) and (b) are almost indifferent. This is corroborated using Figure 3.15 (d) and (e) which show the magnitude of the error percentage between  $I_{\text{Estimated}}$  and  $I_{\text{Theoretical}}$ , and  $I_{\text{Measured}}$  respectively. The overall magnitude of error difference between  $I_{\text{Estimated}}$  and  $I_{\text{Theoretical}}$  over the whole range of irradiance is 1.41%; while the overall magnitude of error difference between  $I_{\text{Estimated}}$  and  $I_{\text{Measured}}$  over the whole range of irradiance is 2.07%. This means that  $I_{\text{Estimated}}$  tracks the MPPT reference ( $I_{\text{Theoretical}}$ ) with a lower error than the actual measurement. This result implies the controller perceives  $I_{\text{Estimated}}$  as tracking  $I_{\text{Theoretical}}$ , when in fact the actual  $I_{\text{Measured}}$  does not track  $I_{\text{Theoretical}}$ . This is evident from the larger  $I_{\text{Measured}}$  error relative to  $I_{\text{Theoretical}}$  in Figure 3.15 (c).

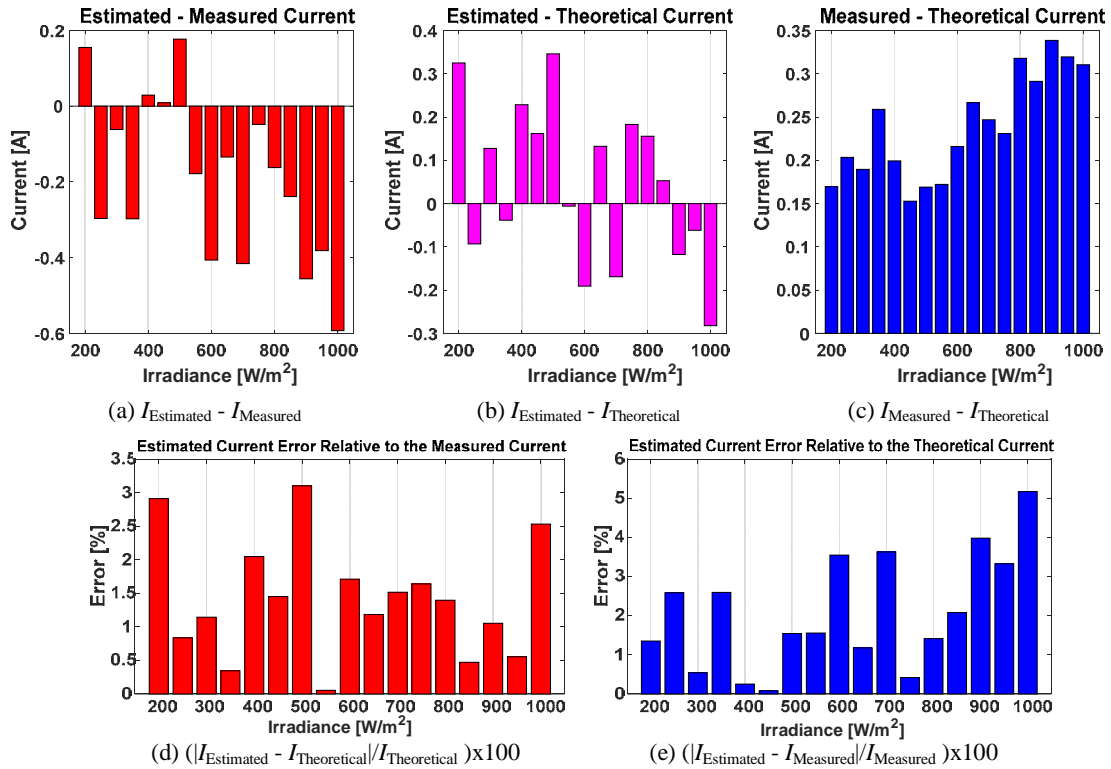


Figure 3.15 A comprehensive SCM parity study of ASC-MPPT estimated current. (a) The error between the estimated current and the measured current in Amperes. (b) The error between estimated current and the theoretical current in Amperes. (c) Error between measured current and theoretical current in Amperes. (d) The magnitude of the estimation error percentage relative to theoretical current. (e) The magnitude of the estimation error percentage relative to the measured current.

Figure 3.15 (c) shows  $I_{Measured}$  with a consistent error that resembles a steady-state constant offset from  $I_{Theoretical}$ . Hence, one way to overcome this hurdle, and improve parity of the estimation, is to quantify this constant error and feed into the SCM observer model as a constant disturbance. Ideally, we would like to have the  $I_{Estimated}$  error with respect to  $I_{Measured}$  minimized. Therefore, a parametric study of different constant error compensation values is shown in Figure 3.16 and the corresponding mean errors of the estimated current relative to  $I_{Theoretical}$  and  $I_{Measured}$ , over the whole range of irradiance values, are plotted

accordingly. When the compensation error is 0.18, the  $I_{\text{Theoretical}}$  relative to  $I_{\text{Measured}}$  is minimized to 1.57%, while the  $I_{\text{Estimated}}$  relative to  $I_{\text{Theoretical}}$  is found to be 2.13%.

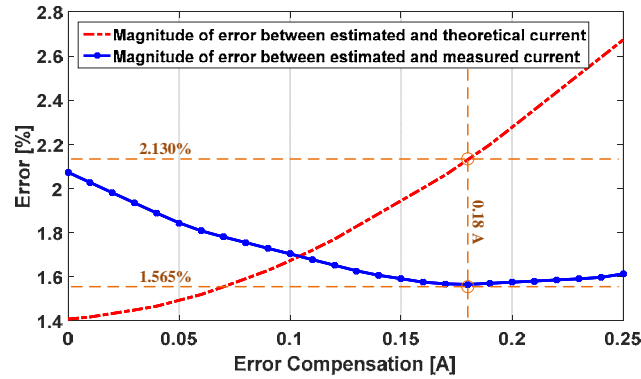


Figure 3.16 Parametric study of the error as a function of compensation. Selecting 0.18 A as a value for error compensation minimizes the error between the magnitude of error between the estimated current and the measured current. To minimize the error between the estimated current and the MPPT theoretical current, other techniques could be employed.

While a larger  $I_{\text{Estimated}}$  error relative to  $I_{\text{Theoretical}}$  worsens the efficacy results, shown in Figure 3.16, it could be considered an estimate with a higher parity, since it better reflects the actual measured current. Control effectiveness for the whole system could now be improved using other proposed techniques: one way is to perform a detailed parameter mismatch and selection study as presented in [127]. Another is to consider adaptive perturbation (variable MPPT step size) to reduce steady-state ripple and accurately track the MPP reference [39].

## **3.6. Experimental verification**

### **3.6.1. Experimental setup**

Detailed simulation results for portions of the proposed ASC-MPPT were presented in [39], this chapter includes experimental verification in hardware. The PV module characteristics used in the experimental setup are given in Table 3.3 at STC (Standard Test Condition: solar irradiance = 1 kW/m<sup>2</sup>, cell temperature = 25 deg. C). The PV module was modeled using two SL600-2.5 Magna-Power supplies in parallel and configured in solar array simulation (SAS) mode according to the manufacturer's recommendation. The SAS PC interface was used to implement EN50530 irradiance and temperature profiles. Sampling time of 10  $\mu$ s is used in the implementation of the control algorithm on the dSPACE DS1006 platform. This sampling time is chosen based on the dSPACE platform capability to handle the experimental verification, which is equivalent to the 100-kHz sampling frequency. The dSPACE platform was employed in this chapter for rapid prototyping. The execution time of the proposed ASC-MPPT using the dSPACE implementation was found to be 12  $\mu$ s, making it possible to use low cost and readily available microprocessors. The power converter hardware is a flyback converter assembled by Texas Instruments as an evaluation board for their C2000 microcontroller. The board model is TMDSSOLARUNIVKIT. To illustrate the functionality of the proposed ASC-MPPT algorithm, the TI controller board was bypassed, and the flyback converter is fully controlled within the dSpace environment. The details of the experimental setup are as shown in Table 3.3. A photograph of the full experimental setup used to verify the functionality of the proposed algorithm is shown in Figure 3.17.

Table 3.3 Details of the experimental setup

Photovoltaic Emulator	Two Magna-Power SL600-2.5 supplies connected in parallel
Open-circuit voltage ( $V_{OC}$ )	40 V
Short-circuit current ( $I_{SC}$ )	5.0 A
Voltage at MPP ( $V_{MP}$ ) - STC	30 V
Current at MPP ( $I_{MP}$ ) - STC	4.0 A
Controller Platform	dSpace 1006 for ASC-MPPT TI C2000 for InCon MPPT
Sampling Time ( $T_S$ )	10 $\mu$ s
Load	Resistive, 500 Ohms
Flyback Converter	TI TMDSSOLARUNIVKIT Evaluation Board
Output Capacitor (C)	100 $\mu$ F
Input Capacitor ( $C_{in}$ )	94 $\mu$ F
Primary Switch	MOSFET, IRFB4227PBF
Secondary Switch	Diode, CSD10060G
Transformer	ViTEC, 53PR105
Snubber Circuit	Active Clamp technique
Ave. Switching Frequency	100 kHz

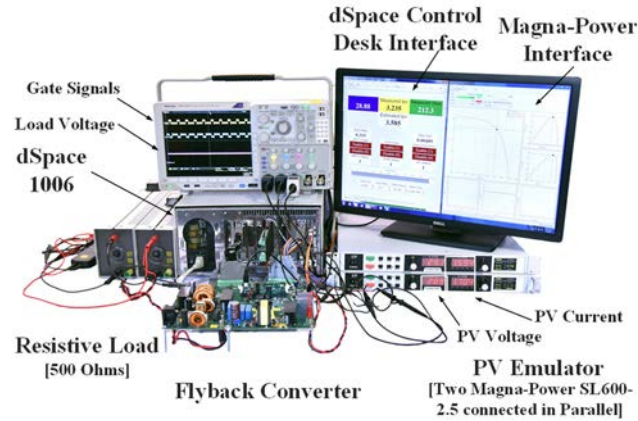


Figure 3.17 The experimental setup while running the EN50530 standardized test on the proposed ASC-MPPT algorithm.

The dynamic EN50530 test procedure agreed upon in the European Union has gained wide acceptance as a standardized test for photovoltaic systems' MPPT accuracy and conversion efficiency [125]. The test sequence principle is demonstrated in Figure 3.8. Ramp slopes  $\zeta_n$  are gradually increased by a factor of  $\varepsilon$ . Over the period of the test, the ramps are repeated  $n$  times. The EN 50530 irradiance profile of Figure 3.8 is used to

assess the performance of the flyback converter PV system controlled using the proposed ASC-MPPT algorithm.

### **3.6.2. Experimental results**

Figure 3.18 (a) shows oscilloscope waveforms of the experimental setup running the proposed ASC-MPPT algorithm for an hour and ten minutes long portion of the EN50530 standardized test. PV voltage, PV current, and load voltage do show the tracking throughout the timeframe of the test. The actual circuit operation power waveform calculated for the experimental setup running the proposed ASC-MPPT algorithm is shown in Figure 3.18 (b) and is compared to the theoretical MPP curve. The resulting control efficacy of the proposed algorithm throughout the portion of the test is shown in Figure 3.18 (c). Upper and lower boundaries are calculated by accounting for instrumentation precision. Results shown, in general, indicate lower controller efficacy at lower insolation operation points.

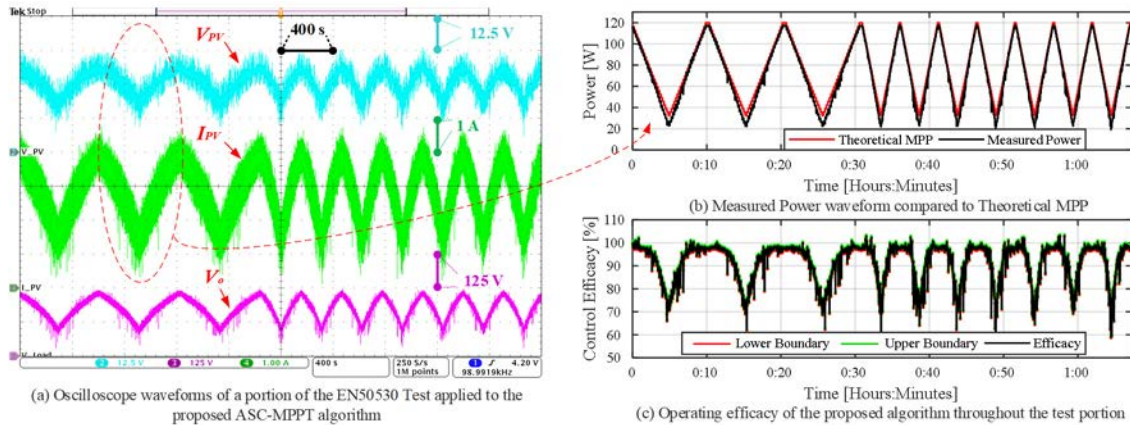


Figure 3.18 Portion of the EN 50530 standardized test applied to the experimental setup. (a) Oscilloscope waveforms of the experimental setup running the proposed ASC-MPPT algorithm for an hour and ten minutes long portion of the EN50530 standardized test. PV voltage, PV current and Load voltage do show the tracking throughout the timeframe of the test. (b) Actual circuit operation power waveform calculated for the experimental setup running the proposed ASC-MPPT algorithm and compared to the theoretical MPP. (c) Control efficacy of the proposed algorithm throughout the portion of the test. Upper and lower boundaries are calculated by accounting for instrumentation precision.

### 3.6.3. Analysis of results based on NREL data

The total energy captured over a whole year arranged by insolation ranges is illustrated in Figure 3.19. Each point on the curve represents a bin of  $20 \text{ W/m}^2$  irradiance range. The insolation and temperature data used were based on the 2018 NREL data for the State of Arizona [128]. The captured energy in kWh is based on theoretical MPP for the setup used in this chapter. The top lines show a cumulative distribution function of the percentage of energy captured over specific ranges of insolation values throughout the year. The total amount of available energy captured is 23.5% for irradiance values less than  $500 \text{ W/m}^2$ . Hence, achieving high overall system effectiveness is plausible even with more reduced system performance at low insolation profiles.



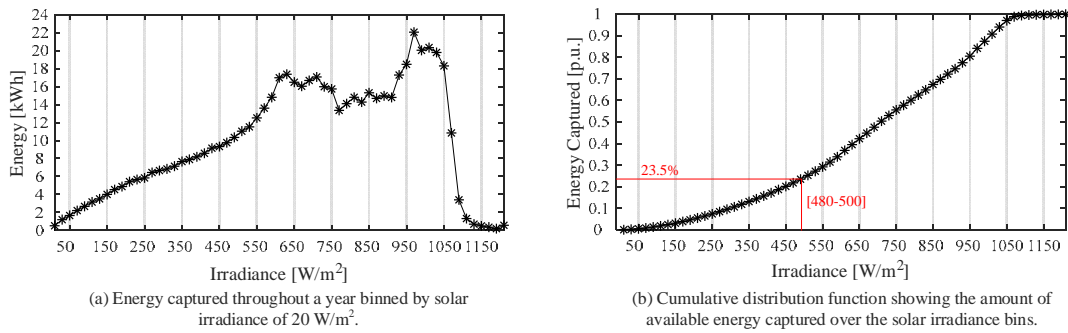


Figure 3.19 The insolation and temperature data used were based on the 2018 NREL data for the State of Arizona. The captured energy in kWh is based on theoretical MPP for the setup used in this chapter. (a) Total energy captured throughout a year binned by solar irradiance of 20 W/m<sup>2</sup>. (b) Cumulative distribution function showing the amount of available energy captured over the solar irradiance bins. The total amount of available energy captured is 23.5% for irradiance values less than 500 W/m<sup>2</sup>.

### 3.6.4. Comparative analysis of results

To further understand the performance of the proposed ASC-MPPT, a 10-minute portion that is shown in Figure 3.20 (a) is evaluated in detail. The insolation range used is between 500 and 1000 W/m<sup>2</sup>, which has been shown to encompass 83% of the overall energy captured (Figure 3.19).

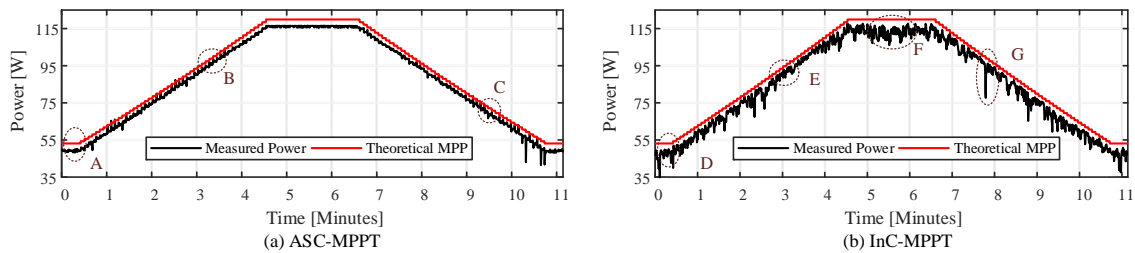


Figure 3.20 An experimental comparison based on hardware tests for the proposed ASC-MPPT in comparison to Incremental Conductance (Inc) MPPT based on portion of the EN50530 testing sequence from irradiance 500 W/m<sup>2</sup> to 1000 W/m<sup>2</sup>. (a) Power waveform for the experimental setup running the proposed ASC-MPPT algorithm. (b) Power waveform calculated from a ten-minute portion of the test measurements for the experimental setup running Incremental conductance MPPT. Waveform in (a) shows similar efficacy like (b), but with significantly less oscillations.

A comparative study is utilized using the built-in InC-MPPT on the TI evaluation board as an illustrative reference to evaluate performance. Figure 3.20 (b) shows the power waveform calculated from a ten-minute portion of the test measurements for the experimental setup running InC-MPPT. Waveforms show very high oscillations around the MPP. The overall efficacy of the built-in InC-MPPT was found to be in the range of 94.8-95.6% when accounting for measurement precision. Reported fully tuned InC-MPPT performance within the literature is shown to be in the range of 97-98% [119, 122]. The proposed ASC-MPPT power waveforms shown in Figure 3.20 (c), also demonstrate an overall MPPT efficacy in the range of 95.8-96.6%. These efficacy results are illustrative and could be improved upon by improving the fidelity of the model. The model presented in this chapter solely considers first order circuit effects. Model fidelity of MPC has been studied with a detailed parameter mismatch study performed [127]. A model parity of the proposed sensorless current algorithm is also studied in detail to assess the fidelity of the current observer model in comparison to the actual current sensor measurement [107].

Results illustrated in Figure 3.20 compare the performance of the proposed algorithm with InC-MPPT. Figure 3.20 (a) and (b) generally show similarly effective performance results. In InC-MPPT, Figure 3.20 (b) detail D, the measured power exhibits high oscillations that have peaks closer to the theoretical MPP when compared to Figure 3.20 (a) detail A. The mean Inc-MPPT efficacy at  $500 \text{ W/m}^2$  is 90.7%, while the mean efficacy for ASC-MPPT is 88.8% at  $500 \text{ W/m}^2$ . InC-MPPT shows higher oscillation than ASC-MPPT, which is an inherent feature of any extremum seeking algorithm. ASC-MPPT shows better settling time in comparison to InC-MPPT in response to step changes

as is evident at points Figure 3.21 (a) detail A and Figure 3.21 (b) detail D. Figure 3.20 (b) detail F and Figure 3.21 (b) detail E show that InC-MPPT exhibits vigorous oscillations at  $1000 \text{ W/m}^2$  when compared to the ASC-MPPT (Figure 3.21 (a) detail B). Mean efficacy of InC-MPPT at  $1000 \text{ W/m}^2$  is 97.1%, and is 97.5% for ASC-MPPT. Figure 3.20 (b) detail G and Figure 3.21 (b) detail F also shows a very long settling time, and an undershoot in the InC-MPPT. While this phenomenon occurs in the ASC-MPPT, such as on Figure 3.21 (a) detail C, it is not as pronounced.

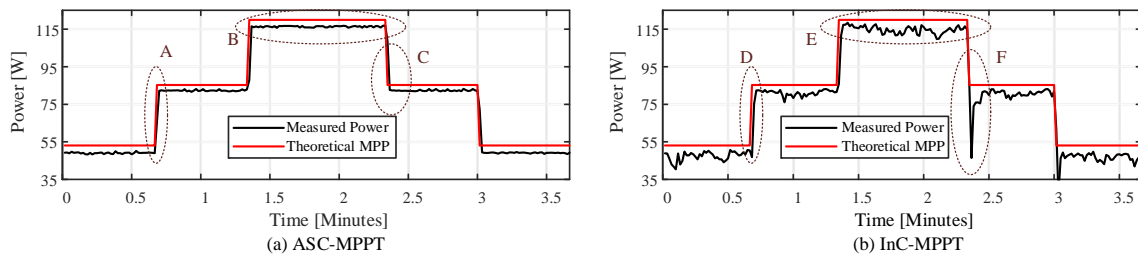


Figure 3.21 An experimental comparison based on hardware tests for the proposed ASC-MPPT in comparison to Incremental Conductance (Inc) MPPT based on a step change test from irradiance  $500 \text{ W/m}^2$  to  $750 \text{ W/m}^2$  to  $1000 \text{ W/m}^2$  and back to  $750 \text{ W/m}^2$  then  $500 \text{ W/m}^2$ . (a) Power waveform for the experimental setup running the proposed ASC-MPPT algorithm. (b) Power waveform calculated from a ten-minute portion of the test measurements for the experimental setup running Incremental conductance MPPT. The waveform in (a) shows lower settling time, lower steady-state error and less oscillations than (b).

### 3.6.5. Results discussion

The impact temperature changes have on the module  $P$ - $V$  characteristics occurs over a longer time interval when compared to irradiance changes. Figure 3.22 is a contour plot showing control effectiveness results for the proposed ASC-MPPT corresponding to different temperature and insolation data as independent variables. According to Figure 3.22, the proposed algorithm shows a broad region of high efficacy operating conditions when considering data in Figure 3.19.

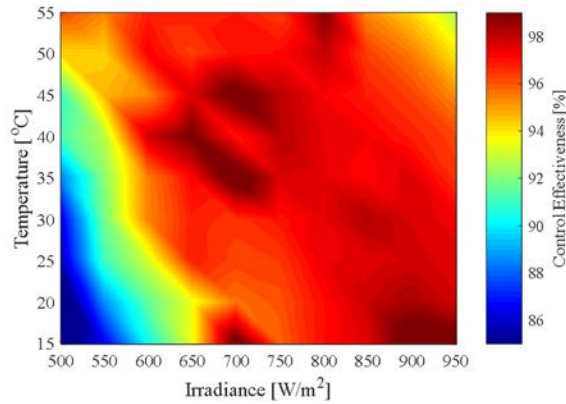


Figure 3.22 A contour plot showing control effectiveness results for the proposed ASC-MPPT corresponding to different temperature and insolation data.

Overall the proposed ASC-MPPT has shown similar performance to InC-MPPT while achieving additional benefits. First, ASC-MPPT does not have the oscillations that are inherent to the InC-MPPT algorithm due to the adaptive perturbation feature. ASC-MPPT settles faster due to the predictive nature of MPC. ASC-MPPT does not use any current sensor, making it ideal for hot temperatures, as higher temperature environments do impact the sensor measurements, temperature drift [97, 98]. Additionally, the eliminated current sensor is a fundamental circuit component that is compensated for by code, which has the potential of reducing the overall cost of the MPPT converter.

### 3.7. Implementation in a low cost microcontroller unit

MPC is a computationally intensive control algorithm as each state variable in the system is evaluated for each of the possible control actuates. Adding to the complexity of MPC is the multi-objective optimization of the penalty function. As such, plenty of research on the area of MPC in power electronics implement their algorithms on expensive

platforms such as dSPACE and OPAL-RT. While such platforms are excellent rapid prototyping platforms, they are expensive and may be impractical in product design. This chapter demonstrated a cost-saving method of using MPC to eliminate a fundamental hardware component in the MPPT converter, the current sensor. However, the rapid prototyping platform, dSPACE used is expensive and not practical for such an application.

This section explores the use of a low-cost microcontroller unit (MCU) to illustrate the MPC based sensorless current mode application proposed in this chapter. Experimental results using the dSPACE 1106 and the TMS320F28379D MCU showing steady-state performance and dynamic response are illustrated and compared. Comparative results show the implemented MCU offers similar performance with dSPACE.

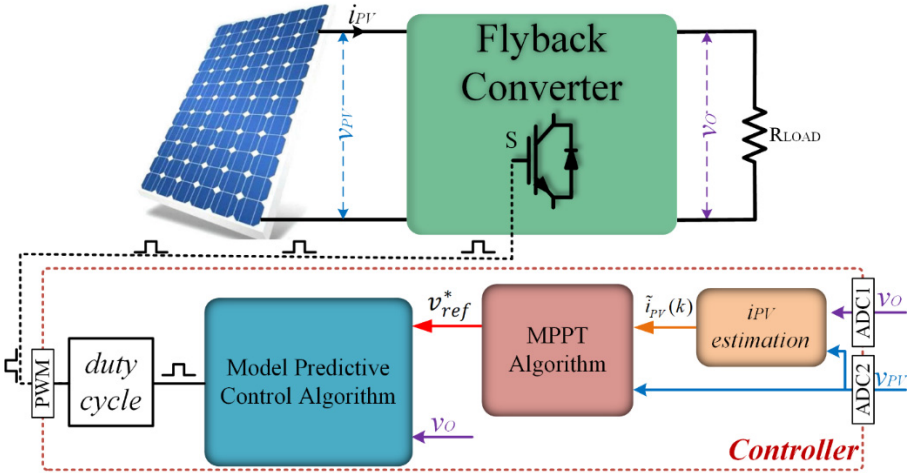


Figure 3.23 Implementation schema of the control algorithm.

The control algorithm demonstrated in Figure 3.4 and Figure 3.3 is presented in Figure 3.23 in terms of the needed MCU hardware resources. The MPC based MPPT code has been carried out in MATLAB function code blocks and is demonstrated in Appendix A, Table A.1. The ADC and PWM blocks specific to dSPACE were connected to the

function block code as is illustrated in Figure 3.23. The advantage of using the MATLAB/Simulink platform is its ease of use. Matlab is generally used by power electronics engineers and researchers which allows for collaboration and easier sharing of knowledge. Furthermore, some MCUs, DSPs, FPGAs and dSPACE can be programmed via MATLAB by using code conversion environments. MATLAB uses Simulink Coder, Embedded Coder and HDL Coder to convert Simulink models to any programming language such as C and VHDL.

For example, using the code generation feature of MATLAB a compact relational database (SDF) file is created from the Simulink model that could be imported to dSPACE Control Desk software to be implemented within the dSPACE environment. Another example, Texas Instruments (TI) compiler, Code Composer Studio (CCS) is used within the MATLAB environment to generate a programming file for TI digital signal processing boards DSP. MATLAB converts the Simulink model to C language and CCS compiles the codes for generating the programming file. Texas Instruments provides a special embedded coder library for TI C2000 MCUs. The libraries for both the controllers include hardware specifications such as ADC, PWM and logic IO. Figure 3.24 clarifies the structure of the control software. The same control structure (Figure 3.23) is used for both the controller by only changing special controller blocks (ADCs and PWM).

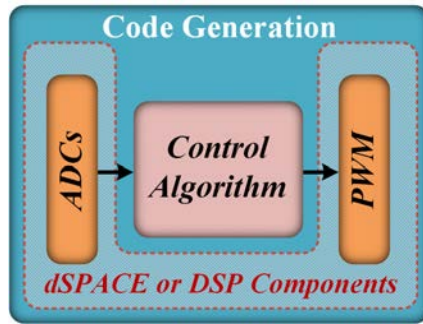


Figure 3.24 Implementation schema of the control algorithm.

The control algorithm has been implemented on both dSPACE 1006 and DSP TMS320f28379D MCU to compare the performance of the controllers. Figure 3.23 shows the block schema of the implemented control algorithm. As seen from the figure, output voltage and PV voltage are used as measured system parameters. The input current of the converter is estimated and is used in the MPPT algorithm. The MPPT algorithm generates a reference voltage by depending on the maximum power point. MPC algorithm generates a digital signal to control the converter by depending on the reference voltage. The average value of the logic signal is calculated to obtain the duty ratio of the logic signal. The control signal that has fixed frequency is obtained by applying the duty ratio to PWM channel.

Experimental results using the experimental setup in Table 3.3 for the dSPACE implementation were shown in Figure 3.18. Experimental using the TI DSP implementation are as shown in Figure 3.25. Figure 3.25 (a) shows oscilloscope waveforms of the experimental setup running the proposed ASC-MPPT algorithm for an hour and ten minutes long portion of the EN50530 standardized test. PV voltage, PV current, and load voltage do show the tracking throughout the timeframe of the test. The

actual circuit operation power waveform calculated for the experimental setup running the proposed ASC-MPPT algorithm is shown in Figure 3.25 (b) and is compared to the theoretical MPP curve. The resulting control efficacy of the proposed algorithm throughout the portion of the test is shown in Figure 3.25 (c). Upper and lower boundaries are calculated by accounting for instrumentation precision. Results in Figure 3.18 and Figure 3.25, in general, illustrate the viability of the low cost MCU implementation of the MPC based MPPT algorithm.

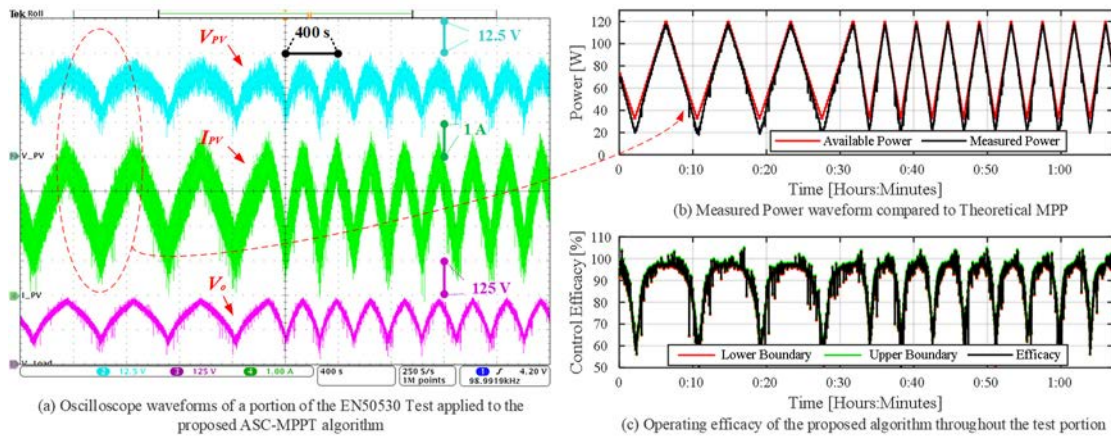


Figure 3.25 Portion of the EN 50530 standardized test applied to the experimental setup using TI C2000. (a) Oscilloscope waveforms of the experimental setup running the proposed ASC-MPPT algorithm for an hour and ten minutes long portion of the EN50530 standardized test. PV voltage, PV current and Load voltage do show the tracking throughout the timeframe of the test. (b) Actual circuit operation power waveform calculated for the experimental setup running the proposed ASC-MPPT algorithm and compared to the theoretical MPP. (c) Control efficacy of the proposed algorithm throughout the portion of the test. Upper and lower boundaries are calculated by accounting for instrumentation precision.

A closer performance comparison between the dSPACE implementation the low cost MCU implementation based on TI C2000 include a step response as is shown in Figure 3.26 and a ramp response as is shown in Figure 3.27. Some undershoot anomalies are noted in Figure 3.27(a) at the 13<sup>th</sup> minute and Figure 3.27(b) at the 16<sup>th</sup> minute. Such



anomalies are attributed to instrumentation errors. Overall the performance of the control algorithm using low-cost MCU has not been compromised.

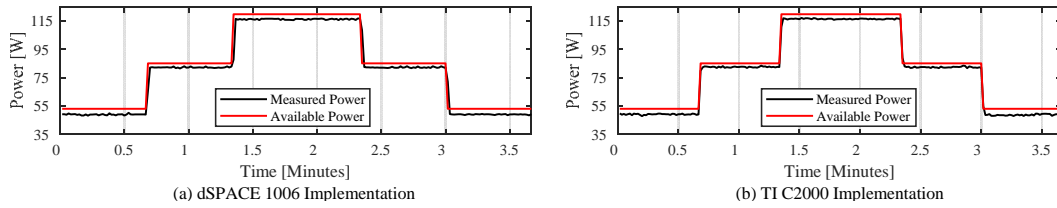


Figure 3.26 An experimental comparison based on hardware tests for the proposed ASC-MPPT in comparison to Incremental Conductance (Inc) MPPT based on a step change test from irradiance 500 W/m<sup>2</sup> to 750 W/m<sup>2</sup> to 1000 W/m<sup>2</sup> and back to 750 W/m<sup>2</sup> then 500 W/m<sup>2</sup>. (a) Power waveform for the experimental setup running the proposed ASC-MPPT algorithm. (b) Power waveform calculated from a ten-minute portion of the test measurements for the experimental setup running Incremental conductance MPPT. The waveform in (a) shows lower settling time, lower steady-state error and less oscillations than (b).

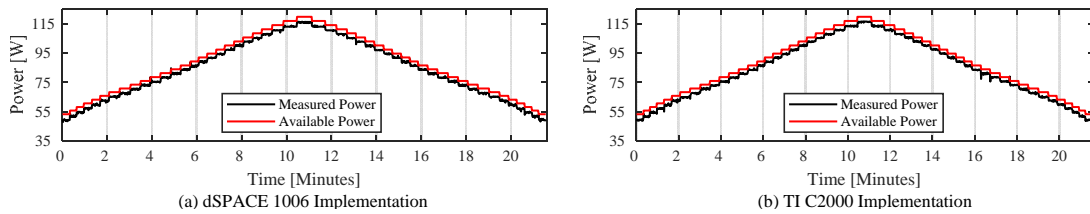


Figure 3.27 An experimental comparison based on hardware tests for the proposed ASC-MPPT in comparison to Incremental Conductance (Inc) MPPT based on realistic NREL data. (a) Power waveform for the experimental setup running the proposed ASC-MPPT algorithm. (b) Power waveform calculated from a ten-minute portion of the test measurements for the experimental setup running Incremental conductance MPPT. The waveform in (a) shows lower settling time, lower steady-state error and less oscillations than (b).

As has been established in the previous section, ASC-MPPT does not use any current sensor, making it ideal for hot temperatures, as higher temperature environments do impact the sensor measurements, temperature drift [97, 98]. Additionally, the eliminated current sensor is a fundamental circuit component that is compensated for by code, which has the potential of reducing the overall cost of the MPPT converter. Previous

results were demonstrated using a \$30,000 rapid prototyping platform which is expensive and impractical for mass production. This section demonstrated the same code functionality and performance can be implemented on a \$17 low-cost F28379D MCU. While this section demonstrated the general possibility of low cost implementation, further engineering of the code could reduce the cost of the required MCU even further.

### **3.8. Conclusion**

This chapter utilized the model-based framework of MPC to develop a MPPT algorithm that eliminates the input-side current sensor in a PV application. The implementation of MPC realizes the observer-based SCM being fundamentally model-based design, expressed within the cost function. This chapter also utilized constrained control and online auto-tuning of MPC to develop an adaptive perturbation MPPT to reduce steady-state oscillation and improve dynamic performance. The contribution of this chapter is that the observer model for the sensorless-current control and the adaptive perturbation MPPT are incorporated directly into the MPC formulation. Eliminating the current sensor, a fundamental component of the circuit, can reduce the cost and improves the reliability of the PV system especially when the system involves a cascaded or a multi-level topology. The sensorless current tracking of the maximum power point, has been shown to alleviate the temperature and aging drift of the sensor. In this chapter, the experimental results of the proposed algorithm were presented and compared to other well-known MPPT algorithms. The proposed algorithm showed good reference tracking with a fast dynamic response and small ripple in steady-state. A study of parameter mismatch has demonstrated that the model-based design functions at high efficacy within

a wide mismatch range. A model parity study of the current surrogate model has shown the fidelity of the proposed observer-based technique. Dynamic testing of the proposed algorithm has shown fast-tracking and robustness to disturbance. Finally, the proposed algorithm has been implemented on a low-cost microcontroller unit which presents a step closer to wide-scale production.

## 4. MAXIMUM POWER POINT TRACKING IN A GRID-INTERACTIVE INVERTER – SUB-MULTILEVEL INVERTER\*

### 4.1. Introduction

The purpose of this chapter is to demonstrate an application example of the interaction between the proposed standalone MPPT algorithm in Chapter 3 with other grid-interactive converters. One identified challenge in the area of MPPT is the partial shading effects on the photovoltaic energy harvest. PV modules are typically connected in series strings to increase their total voltage. However, factors like partial shading, manufacturing variability, cell aging, and thermal gradients result in mismatch [129, 130]. Such factors cause the MPP algorithm to be stuck at a local MPP causing a hindered system-level energy capture [129, 131]. There are many proposed remedies for the partial shading problem, and the simplest is adding a bypass diode. Conventionally bypass diodes are used in series-connected PV modules to allow for a current path around the shaded

---

\*Part of the data reported in this chapter is reprinted with permission from “Sensorless Current Model Predictive Control for Maximum Power Point Tracking of Single-Phase subMultilevel Inverter for Photovoltaic Systems” by M. Metry, S. Bayhan, M. B. Shadmand, R. S. Balog, and H. Abu-Rub, 2016. Presented at the IEEE Energy Convers. Congr. and Expo. (ECCE), Milwaukee, WI, 18-22 Sep 2016, p. 1-8, Copyright © 2016 IEEE

\*Part of the data reported in this chapter is reprinted with permission from “Model Predictive Control for PV Maximum Power Point Tracking of Single-Phase subMultilevel Inverter” by M. Metry, S. Bayhan, R. S. Balog, and H. Abu Rub, 2016. Presented at the IEEE Power and Energy Conference at Illinois (PECI), Illinois, Urbana, Illinois, 2016, p. 1-6, Copyright © 2016 IEEE

\*Part of the data reported in this chapter is reprinted with permission from “An Effective Model Predictive Control for Grid Connected Packed U Cells Multilevel Inverter” by M. Trabelsi, S. Bayhan, M. Metry, H. Abu Rub, L. Ben-Brahim, and R. S. Balog, 2016. Presented at the IEEE Power and Energy Conference at Illinois (PECI), Illinois, Urbana, Illinois, 2016, p. 1-6, Copyright © 2016 IEEE

module; hence, increase the overall energy harvest. However, efficiency losses with bypass diodes are considerably large [132].

Another approach is to use submodule integrated converters as in [133] and [134]. Such an approach, Figure 4.1, allows the first stage converters to identify the MPP for each module/submodule separately. Without loss of generality, the submodules in Figure 4.1 could also be PV modules or PV arrays. Such topology provides the advantage of localized MPPT, increased reliability of the whole power system as the failure of one cell won't cause the whole system to fail, and lower ratings for components [133]. Submodule power processing significantly improves efficiency when compared to the bypass diode approach [135].

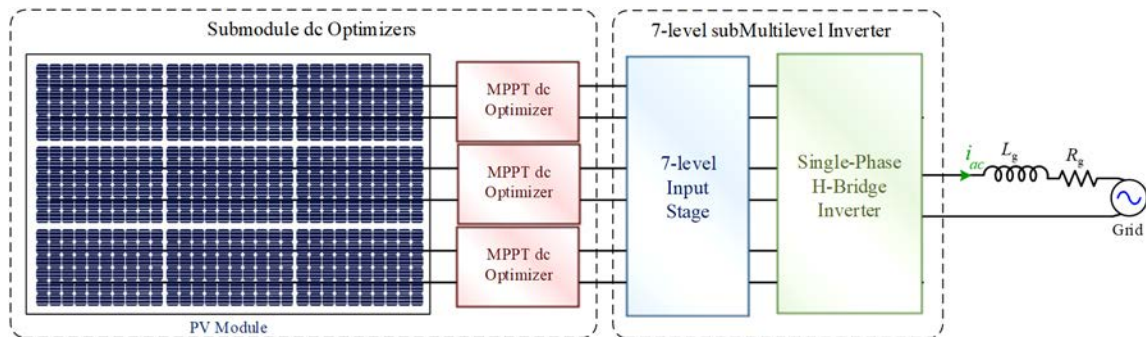


Figure 4.1 Submodule PV power processing for MPPT to reduce the effect of partial shading. The output of the dc power optimizer stage is connected to a single-phase 7-level SMI.

The development and use of Multilevel Inverter (MI) topologies [136-138], such as in Figure 4.1, with renewable energy sources such as wind, solar, and fuel-cell have increased rapidly due to the rising demand for high power and medium voltage applications. The MIs are an attractive alternative to the traditional inverters due to their

high-quality output voltage, lower switching losses, less voltage stress on power switches, and higher efficiency.

This chapter explores the use of a 7-level sub-multilevel inverter (sMI). The sMI uses fewer switches than conventional multilevel inverters (MI), which is more significant at higher number of levels. The single-phase H-bridge inverter in the sMI topology uses the line frequency, which allows for lower switching losses when compared to conventional MIs. Also, the 7-level output voltage is not affected by the mismatch in the submodule voltages for the dc optimizer, making it suitable for PV application.

The current control technique of the sMI plays a vital role to guarantee the reliable and efficient operation of the grid-connected generation systems. Traditionally, a proportional-integral (PI) based cascaded control structure has been used. The use of optimization-based MPC for current control improves the steady-state and transient behavior of the system [139]. Moreover, system constraints and uncertainties can be incorporated systematically into the MPC design in such a way that they are included in the optimization problem formulation [116, 140].

This chapter is organized as follows:

Section 4.2 presents the background on the submultilevel inverter

Section 4.3 presents the background on the boost converter with detailed circuit analysis

Section 4.4 derives the MPC formulation

Section 4.5 presents simulation results including dynamic tests and real-time implementation results

Section 4.6 concludes the contribution of this chapter.

## 4.2. Background on the sub-multilevel inverter

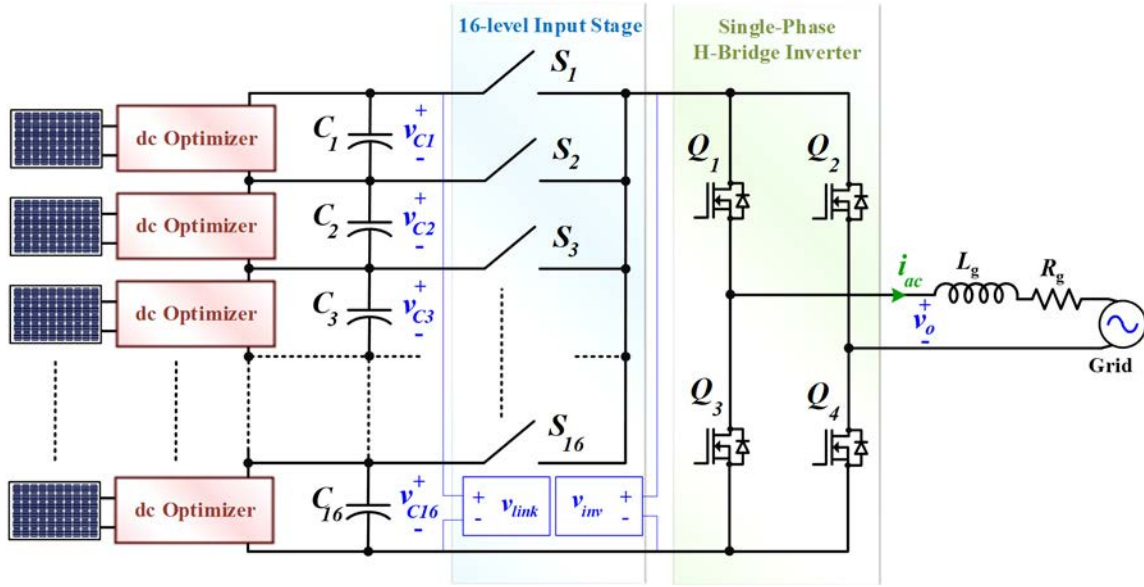


Figure 4.2 The block diagram of single-phase 16-level SMI in a PV generation system.

### 4.2.1. Circuit analysis

Consider the 16-level sub-multilevel inverter topology in Figure 4.2. The switches in the input stage  $S_1 - S_{16}$  are switched sequentially. Switches  $S_1 - S_{16}$  could be bidirectional switches to allow 4-quadrant operation [141, 142]. For example, in the case  $S_1$  is turned on, while the other arms are turned off, the inverter voltage  $v_{inv} = \sum_{n=1}^{16} v_{Cn}$ , where  $n$  refers to the capacitor number as  $n \in \{1, 16\}$ . Let the switch being turned-on be labeled  $S_m$ , where  $m \in \{1, 16\}$ . The values for  $v_{inv}$ , as the switches  $S_1 - S_{16}$  are gated sequentially, is  $v_{inv} = \sum_{n=m}^{16} v_{Cn}$ . Let the link voltage  $v_{link}$  be the sum of all the capacitor voltages  $v_{link} = \sum_{n=1}^{16} v_{Cn}$ . Assuming all the capacitor voltages are balanced, the inverter voltage can be written as  $v_{inv} = v_{link}/m$ . The 16-level input stage is capable of producing the voltage levels, as shown in Figure 4.3.

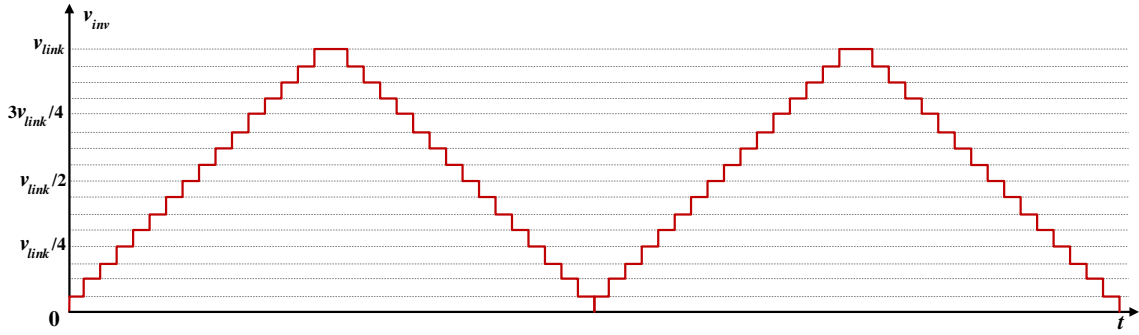


Figure 4.3 The output voltage levels produced by the 16-level input stage ( $v_{inv}$ ) as a function of the link voltage ( $v_{link}$ ).

The inverter H-bridge stage in Figure 4.2 allows for the generation of positive, negative, and zero levels. In such case the output voltage  $v_o$  is  $v_o = +v_{inv}$ ,  $v_o = -v_{inv}$  or  $v_o = 0$ . The possible voltage level for the single-phase H-bridge is as shown in Table 4.1.

Table 4.1 Switching table for the single-phase H-bridge.

$Q_1$	$Q_2$	$Q_3$	$Q_4$	$v_o$
0	0	1	1	0
1	0	0	1	$+v_{inv}$
0	1	1	0	$-v_{inv}$
1	1	0	0	0

The sMI is expandable to higher levels (i.e., 33-level). In this chapter, the control of a 7-level sMI is discussed to facilitate the detailed study of the system behavior. Without loss of generality, the control formulation discussed in this chapter could be expanded to any number of levels.



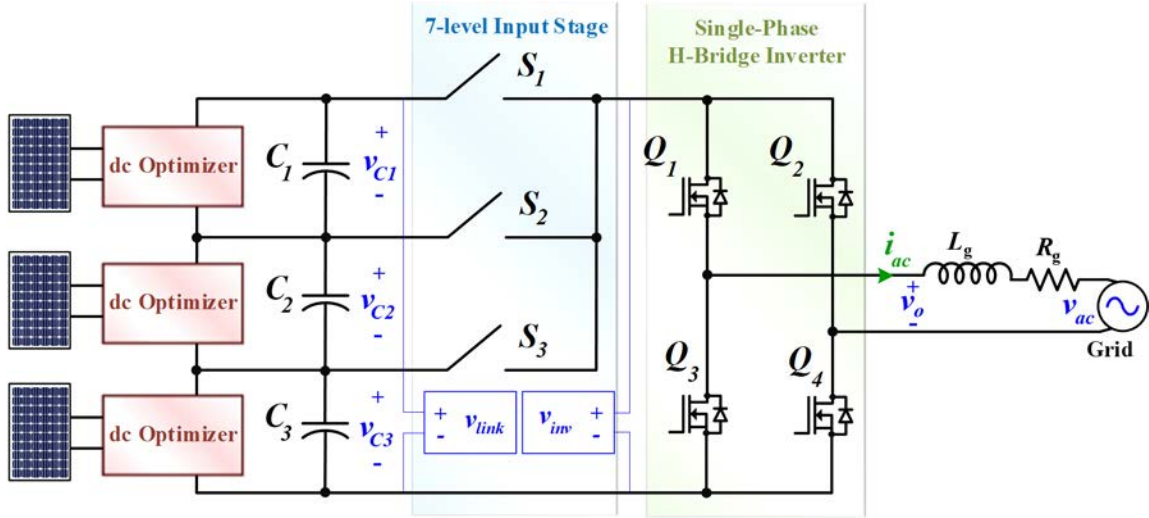


Figure 4.4 The block diagram of single-phase 7-level SMI in a PV generation system.

The 7-level sub-multilevel inverter topology is illustrated in Figure 4.4. The switches in the input stage  $S_1 - S_3$  are switched sequentially. In the case  $S_1$  is turned on, while the other arms are turned off, the inverter voltage  $v_{inv} = \sum_{n=1}^3 v_{Cn}$ , where  $n$  refers to the capacitor number as  $n \in \{1,3\}$ . Let the switch being turned-on be labeled  $S_m$ , where  $m \in \{1,3\}$ . The values for  $v_{inv}$ , as the switches  $S_1 - S_3$  are gated sequentially, is  $v_{inv} = \sum_{n=m}^3 v_{Cn}$ . Let the link voltage  $v_{link}$  be the sum of all the capacitor voltages  $v_{link} = \sum_{n=1}^3 v_{Cn}$ . Assuming all the capacitor voltages are balanced, the inverter voltage can be written as  $v_{inv} = v_{link}/m$ . The 7-level input stage and the H-bridge stage output voltage  $v_o$  is capable of producing the voltage levels, as shown in Table 4.2, where  $\sigma$  denotes the state number.

Table 4.2 Switching table for the 7-level sMI.

$\Omega$	$S_1$	$S_2$	$S_3$	$Q_1$	$Q_2$	$Q_3$	$Q_4$	$v_{inv}$	$v_o$
1	1	0	0	0	0	1	1	$v_{link}$	0
2				1	0	0	1		$+v_{link}$
3				0	1	1	0		$-v_{link}$
4				1	1	0	0		0
5	0	1	0	0	0	1	1	$\frac{2v_{link}}{3}$	0
6				1	0	0	1		$+\frac{2v_{link}}{3}$
7				0	1	1	0		$-\frac{2v_{link}}{3}$
8				1	1	0	0		0
9	0	0	1	0	0	1	1	$\frac{v_{link}}{3}$	0
10				1	0	0	1		$+\frac{v_{link}}{3}$
11				0	1	1	0		$-\frac{v_{link}}{3}$
12				1	1	0	0		0

### 4.3. The boost converter

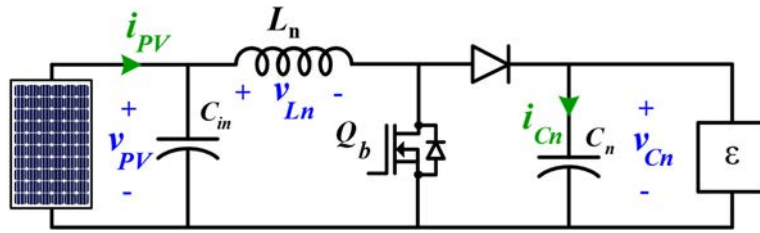


Figure 4.5 The block diagram of the boost converter.

#### 4.3.1. Circuit analysis

Consider the boost converter in Figure 4.5. The load side is connected to some variable  $\varepsilon$ . The load expression  $\varepsilon$  could represent a resistive load, a battery, or another power converter circuit. Discontinuous conduction mode (DCM) maximizes the ripple PV current; hence, the boost converter is analyzed in continuous conduction mode (CCM). The state equations are derived based on the switching of the converter: when the switch ( $Q_b$ ) is closed ( $\sigma = 1$ ) and when the switch ( $Q_b$ ) is open ( $\sigma = 0$ ) as is shown in Figure 4.6.

The load model  $\varepsilon$  could be a resistive load, and in this chapter is an estimated model of the power conversion stage following the boost converter (sMI input stage).

$$i_{C_n}^{\sigma=1}(t) = C_n \frac{dv_{C_n}}{dt} = -i_{\varepsilon}(t) = \frac{-v_{C_n}(t)}{\varepsilon} \quad (4.50)$$

$$i_{C_n}^{\sigma=0}(t) = C_n \frac{dv_{C_n}}{dt} = i_{L_n}(t) - i_{\varepsilon}(t) = i_{L_n}(t) - \frac{-v_{C_n}(t)}{\varepsilon} \quad (4.51)$$

$$v_{L_n}^{\sigma=1}(t) = L_n \frac{di_{L_n}}{dt} = v_{PV}(t) \quad (4.52)$$

$$v_{L_n}^{\sigma=0}(t) = L_n \frac{di_{L_n}}{dt} = v_{PV}(t) - v_{C_n}(t) \quad (4.53)$$

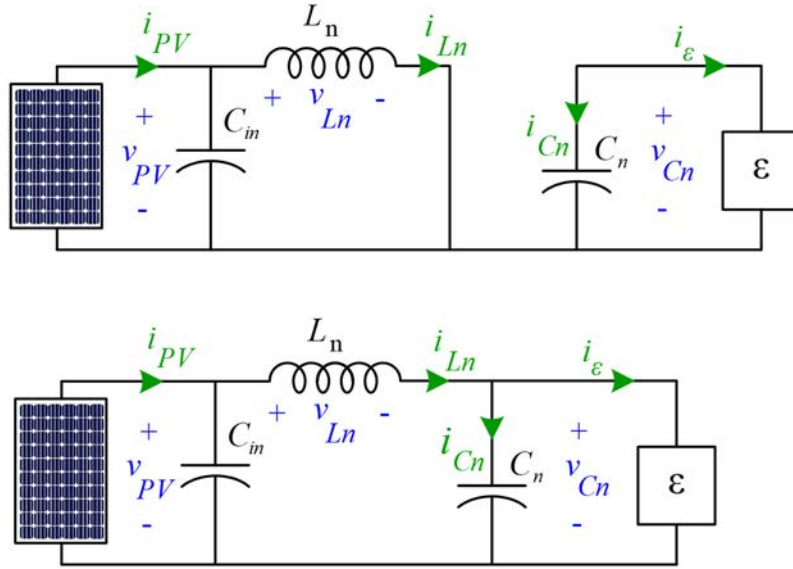


Figure 4.6 The boost converter configuration when  $Q_b$  is turned on,  $\sigma=1$  (top), and when  $Q_b$  is turned off,  $\sigma=0$  (bottom).

The discrete-time estimation of (4.50)-(4.53) in steady-state is found using the Euler forward method for discretization.

$$\tilde{v}_{C_n}^{\sigma=1}(k+1) = \left(1 - \frac{T_s}{C_n \varepsilon}\right) v_{C_n}(k) \quad (4.54)$$

$$\tilde{v}_{C_n}^{\sigma=0}(k+1) = \frac{T_s}{C_n} i_{L_n}(k) + \left(1 - \frac{T_s}{C_n \varepsilon}\right) v_{C_n}(k) \quad (4.55)$$

$$\tilde{i}_{L_n}^{\sigma=1}(k+1) = \frac{T_s}{L_n} v_{PV}(k) - i_{L_n}(k) \quad (4.56)$$

$$\tilde{i}_{L_n}^{\sigma=0}(k+1) = \frac{T_s}{L_n} v_{PV}(k) - \frac{T_s}{L_n} v_{C_n}(k) + i_{L_n}(k) \quad (4.57)$$

The inductor current can be expressed in terms of the PV current and the PV voltage as follows

$$\tilde{i}_{L_n}(t) = i_{PV}(t) - i_{C_{in}}(t) = i_{PV}(t) - C_{in} \frac{dv_{PV}}{dt} \quad (4.58)$$

The discrete-time estimation of (4.58) in steady-state is found using the Euler backward method for discretization.

$$\tilde{i}_{L_n}(k) = i_{PV}(k) - \frac{C_{in}}{T_s} (v_{PV}(k) - v_{PV}(k-1)) \quad (4.59)$$

In light of (4.59), (4.54) and (4.55) can be written as

$$\tilde{v}_{C_n}^{\sigma=1}(k+1) = \left(1 - \frac{T_s}{C_n \varepsilon}\right) v_{C_n}(k) \quad (4.60)$$

$$\tilde{v}_{C_n}^{\sigma=0}(k+1) = \frac{T_s}{C_n} \left[ i_{PV}(k) - \frac{C_{in}}{T_s} (v_{PV}(k) - v_{PV}(k-1)) \right] + \left(1 - \frac{T_s}{C_n \varepsilon}\right) v_{C_n}(k) \quad (4.61)$$

Using equations (4.50) to (4.61) directly for MPPT implementation would require multiple sensors for the PV voltage, PV current, and the output voltage. Without loss of generality, the load expression  $\varepsilon$  in (4.50) to (4.61) could represent a model for any load-side connected component, as discussed in [113, 114].

### 4.3.2. Steady-state averaging

The output voltage is related to the PV voltage, assuming a steady-state operation:

$$V_{C_n} = \frac{V_{PV}}{D'}, \text{ where } D' = \frac{t_{\Omega=0}}{T_s} \quad (4.62)$$

Relation (4.62) is applied to (4.60) and (4.61) to estimate the PV voltage at the next step, assuming that the PV voltage remains constant throughout the sampling period  $T_s$ .

$$\tilde{v}_{PV}^{\sigma=1}(k+1) = D' \left(1 - \frac{T_s}{C_n \varepsilon}\right) v_{Cn}(k) \quad (4.63)$$

$$\tilde{v}_{PV}^{\sigma=0}(k+1) = \frac{D'T_s}{C_n} \left[ i_{PV}(k) - \frac{C_{in}}{T_s} (v_{PV}(k) - v_{PV}(k-1)) \right] + D' \left(1 - \frac{T_s}{C_n \varepsilon}\right) v_{Cn}(k) \quad (4.64)$$

## 4.4. Developing the MPC formulation for the sub-multilevel inverter

### 4.4.1. MPC-based grid current controller

The switching table for the operation of switches for the 7-level sMI is as shown in Table 4.2. To control 7-level sMI's output current ( $i_0$ ), a discrete-time model of the grid-side is analyzed based on Figure 4.4. Based on Kirchhoff's voltage law, the continuous-time expression for the output current ( $i_{ac}$ ) can be described by the following equation

$$v_{Lg}(t) = L_g \frac{di_{ac}}{dt} = v_o(t) - R_g i_{ac}(t) - v_{ac}(t) \quad (4.65)$$

where  $v_o$  is the voltage generated by the 7-level input stage,  $R_g$  is the sum of the load and filter resistances and  $L_g$  is the sum of the load and filter inductances. Accordingly, the discrete-time model for  $i_{ac}$  based on Euler's forward method can be obtained as

$$\tilde{i}_{ac}^{\Omega}(k+1) = \frac{T_s}{L_g} v_o(k) - \left(1 - \frac{R_g T_s}{L_g}\right) i_{ac}(k) - \frac{T_s}{L_g} v_{ac}(k) \quad (4.66)$$

where  $\tilde{i}_{ac}^{\Omega}(k+1)$  is the predicted output current at the next sampling time. Note  $v_o(k)$  can be expressed by  $\mathbf{v}_o$  which is the voltage vector encompassing the seven possible voltage levels from the input stage based on Table 4.2 and is written as

$$\mathbf{v}_o^{\Omega} = \left[ 0 \quad v_{link} \quad -v_{link} \quad 0 \quad 0 \quad \frac{2v_{link}}{3} \quad \frac{-2v_{link}}{3} \quad 0 \quad 0 \quad \frac{v_{link}}{3} \quad \frac{-v_{link}}{3} \quad 0 \right]^T \quad (4.67)$$

The selection of the cost function is a vital part of the MPC technique. The output current cost function is defined as

$$g_1 = |i_{ac}^*(k+1) - \tilde{i}_{ac}^\Omega(k+1)| \quad (4.68)$$

where  $i_{ac}^*(k+1)$  is the reference output current, and  $\tilde{i}_o^\Omega(k+1)$  is the predicted output current in the next step. The reference output current amplitude could be determined based on the grid voltage amplitude and the PV side power, using the expression  $I_{ac}^* = \frac{\sum_{n=1}^3 v_{PVn} i_{PVn}}{V_{ac}}$ . The frequency and phase shift of  $i_{ac}^*$  are based on the frequency and phase shift of the grid voltage  $v_{ac}(t)$ . The reference phase shift of  $i_{ac}^*$  could also be determined using a PQ decoupling controller.

#### 4.4.2. MPC-MPPT for PV side

##### 4.4.2.1. MPC implementation to boost converter

The proposed ASC-MPPT algorithm, proposed in Chapter 3, uses an observer model as a surrogate for the sensor measurement of current. Hence, the surrogate model is an estimated variable in the form  $\tilde{x}(k)$  and can be written as  $\tilde{i}_{PV}(k)$ . This estimate is used along with the measurements:  $v_{PV}(k)$  and  $v_o(k)$  to estimate the PV voltage state variable,  $\tilde{v}_{PV}(k+1)$ , at the next sampling time. The optimization process determines the appropriate actuation that minimizes the cost function in (4.69).

$$\begin{aligned} \min_{g_{2,\sigma \in \{0,1\}}} &= |\tilde{v}_{PV}^\sigma(k+1) - v_{PV.ref}^*(k)| \\ \text{subject to } &\tilde{v}_{PV}^{\sigma=1}(k+1) = D' \left(1 - \frac{T_s}{C_n \varepsilon}\right) v_{Cn}(k) \\ &\tilde{v}_{PV}^{\sigma=0}(k+1) = \frac{D' T_s}{C_n} \left[ i_{PV}(k) - \frac{C_{in}}{T_s} (v_{PV}(k) - v_{PV}(k-1)) \right] + D' \left(1 - \frac{T_s}{C_n \varepsilon}\right) v_{Cn}(k) \end{aligned} \quad (4.69)$$

#### 4.4.2.2. Load model

Since the boost converter is connected to the input stage of the sMI, the load model  $\varepsilon$  can be written in terms of grid voltage and current as follows

$$\varepsilon = \frac{v_c^2}{v_{ac,rms} i_{ac,rms}} \quad (4.70)$$

#### 4.4.2.3. MPC based maximum power point tracking

Previously published work on MPC-MPPT relied on a parallel InC or P&O algorithm to determine  $v_{PV,ref}^*(k)$  in (4.68). The sign of the expression  $\Delta i_{PV}/\Delta v_{PV}$  is used to determine the reference value  $v_{PV,ref}^*(k)$  as is shown in (4.71).

$$v_{PV,ref}^*(k) = \begin{cases} v_{PV}(k) - |\Delta \tilde{v}|, \mu < 0 \\ v_{PV}(k) + |\Delta \tilde{v}|, \mu > 0 \end{cases} \quad \text{for } \mu = \frac{i_{PV}(k) - i_{PV}(k-1)}{v_{PV}(k) - v_{PV}(k-1)} \quad (4.71)$$

where  $|\Delta \tilde{v}|$  is the perturbation size of the MPPT algorithm. The details on obtaining an estimate for  $i_{PV}$  and the details on estimating  $|\Delta \tilde{v}|$  are explained in later sections. Based on (4.71), the MPPT can be expressed within the MPC cost function, as illustrated in (4.72).

$$\begin{aligned} \min_{g_{2,\sigma \in \{0,1\}}} &= |\tilde{v}_{PV}^\sigma(k+1) - v_{PV,ref}^*(k)| \\ \text{subject to } &\tilde{v}_{PV}^{\sigma=1}(k+1) = D' \left(1 - \frac{T_s}{C_n \varepsilon}\right) v_{Cn}(k) \\ &\tilde{v}_{PV}^{\sigma=0}(k+1) = \frac{D' T_s}{C_n} \left[ i_{PV}(k) - \frac{C_{in}}{T_s} (v_{PV}(k) - v_{PV}(k-1)) \right] + D' \left(1 - \frac{T_s}{C_n \varepsilon}\right) v_{Cn}(k) \\ \text{where, } v_{PV,ref}^*(k) &= \begin{cases} v_{PV}(k) - |\Delta \tilde{v}|, \mu < 0 \\ v_{PV}(k) + |\Delta \tilde{v}|, \mu > 0 \end{cases} \quad \text{for } \mu = \frac{i_{PV}(k) - i_{PV}(k-1)}{v_{PV}(k) - v_{PV}(k-1)} \end{aligned} \quad (4.72)$$

$v_{PV,ref}^*(k)$  is the MPPT reference. For this case, since there is only one penalty function in the MPC cost function, the weight factor  $\lambda=1$ .

#### 4.4.2.4. MPC based sensorless current mode

An observer model for the PV current can be obtained by analyzing the boost converter (Figure 4.6) in continuous conduction mode during the two switching states  $\sigma \in \{0,1\}$ . Using Kirchhoff's current law it can be observed that the PV current  $i_{PV}(t)$  is always

$$i_{PV}(t) = i_{Ln}(t) + i_{Cin}(t) = i_{Ln}(t) + C_{in} \frac{dv_{PV}(t)}{dt} \quad (4.73)$$

Based on (4.50) and (4.51), the dc components of the inductor current is derived using the principle of capacitor charge balance [77]. During the first subinterval, the capacitor supplies the load current, and the capacitor is partially discharged. During the second subinterval, the inductor current supplies the load and, additionally recharges the capacitor. The net change in capacitor charge over one switching period is found by integrating  $i_{Cn}(t)$  as follows

$$\int_0^{T_s} i_{Cn}(t)dt = -\left(\frac{V_{Cn}}{\varepsilon}\right)DT_s + \left(1 - \frac{V_{Cn}}{\varepsilon}\right)D'T_s \quad (4.74)$$

Collecting terms, and equating the results to zero, as the net current stored on a capacitor in steady-state during the full period is zero, the steady-state results become

$$-\frac{V_{Cn}}{\varepsilon}(D + D') + I_{Ln}D' = 0 \quad (4.75)$$

By noting that  $(D + D') = 1$ , and by solving for the inductor current dc component  $I_{Ln}$  one obtains

$$I_{Ln} = \frac{V_{Cn}}{D'\varepsilon} \text{ where } D' = \frac{t_{\sigma=0}}{T_s} \quad (4.76)$$

Equation (4.76) can be expressed in terms of the PV voltage as



$$I_{Ln} = \frac{V_{PV}}{D'^2 \varepsilon} \text{ where } D' = \frac{t_{\sigma=0}}{T_s} \quad (4.77)$$

As the change in PV current is relatively slower than the MPC sampling time, the expression  $i_{Ln}(t)$  can be approximated as

$$i_{Ln}(t) \approx I_{Ln} = \frac{V_{PV}}{D'^2 \varepsilon} \quad (4.78)$$

Substituting (4.78) into (4.73), one obtains

$$i_{PV}(t) = \frac{V_{PV}}{D'^2 \varepsilon} + C_{in} \frac{dv_{PV}(t)}{dt} \quad (4.79)$$

The discrete-time estimation of (4.79) is obtained by using the Euler backward method for discretization:  $\sigma$

$$\tilde{i}_{PV}(k) = \frac{V_{PV}}{D'^2 \varepsilon} + \frac{C_{in}}{T_s} [v_{PV}(k+1) - v_{PV}(k)] \quad (4.80)$$

Therefore, (4.80) is used as a model for current, to eliminate the current sensor. SCM is shown to be based on the model-based design principle, which integrates within the MPC framework as in (4.81), and the process is illustrated in the block diagram in Figure 4.7.

$$\begin{aligned} \min_{g_{2,\sigma \in \{0,1\}}} &= |\tilde{v}_{PV}^{\sigma}(k+1) - v_{PV.ref}^*(k)| \\ \text{subject to } &\tilde{v}_{PV}^{\sigma=1}(k+1) = D' \left(1 - \frac{T_s}{C_n \varepsilon}\right) v_{Cn}(k) \\ &\tilde{v}_{PV}^{\sigma=0}(k+1) = \frac{D' T_s}{C_n} \left[ \tilde{i}_{PV}(k) - \frac{C_{in}}{T_s} (v_{PV}(k) - v_{PV}(k-1)) \right] + D' \left(1 - \frac{T_s}{C_n \varepsilon}\right) v_{Cn}(k) \\ &\tilde{i}_{PV}(k) = \frac{V_{PV}}{D'^2 \varepsilon} + \frac{C_{in}}{T_s} [v_{PV}(k+1) - v_{PV}(k)] \end{aligned} \quad (4.81)$$

$$\text{where } v_{PV.ref}^*(k) = \begin{cases} v_{PV}(k) - |\Delta \tilde{v}|, \mu < 0 \\ v_{PV}(k) + |\Delta \tilde{v}|, \mu > 0 \end{cases} \text{ for } \mu = \frac{i_{PV}(k) - i_{PV}(k-1)}{v_{PV}(k) - v_{PV}(k-1)}$$

$$\text{and } \varepsilon = \frac{v_c^2}{v_{ac,rms} i_{ac,rms}}$$

The current surrogate model is derived from within the converter discrete-time model. The use of this sensorless current MPPT adds sizeable benefits for the cascaded dc

optimizer illustrated in Figure 4.1. These benefits include reduced hardware cost and improved reliability, especially so when considering 16-level sMI, as in Figure 4.2.

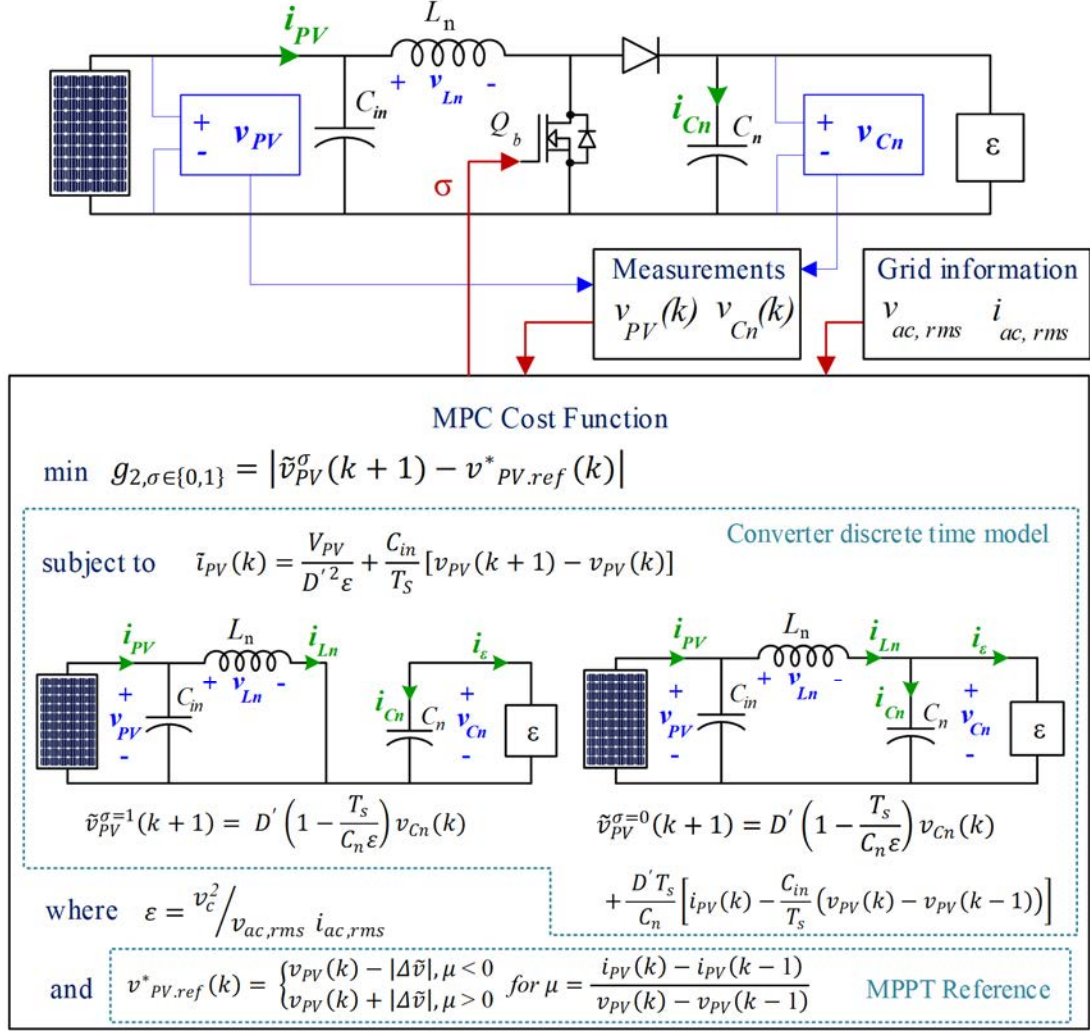


Figure 4.7 The block diagram of the sensorless current MPPT algorithm applied to the boost converter. The current surrogate model is derived from within the converter discrete-time model. The use of this sensorless current MPPT adds sizeable benefits for the cascaded dc optimizer illustrated in Figure 4.1. These benefits include reduced hardware cost and improved reliability, especially so when considering 16-level sMI, as in Figure 4.2.

### 4.4.3. Overall MPC framework for sMI

The overall controller for the 7-level sMI is illustrated in the block diagram of Figure 4.8. The grid-side cost function  $g_1$  is based on (4.68), and the grid-side predictive model is based on (4.66). The PV-side MPPT cost function  $g_2$  is based on (4.81), and the PV-side predictive model is based on (4.63), (4.64), and (4.80).

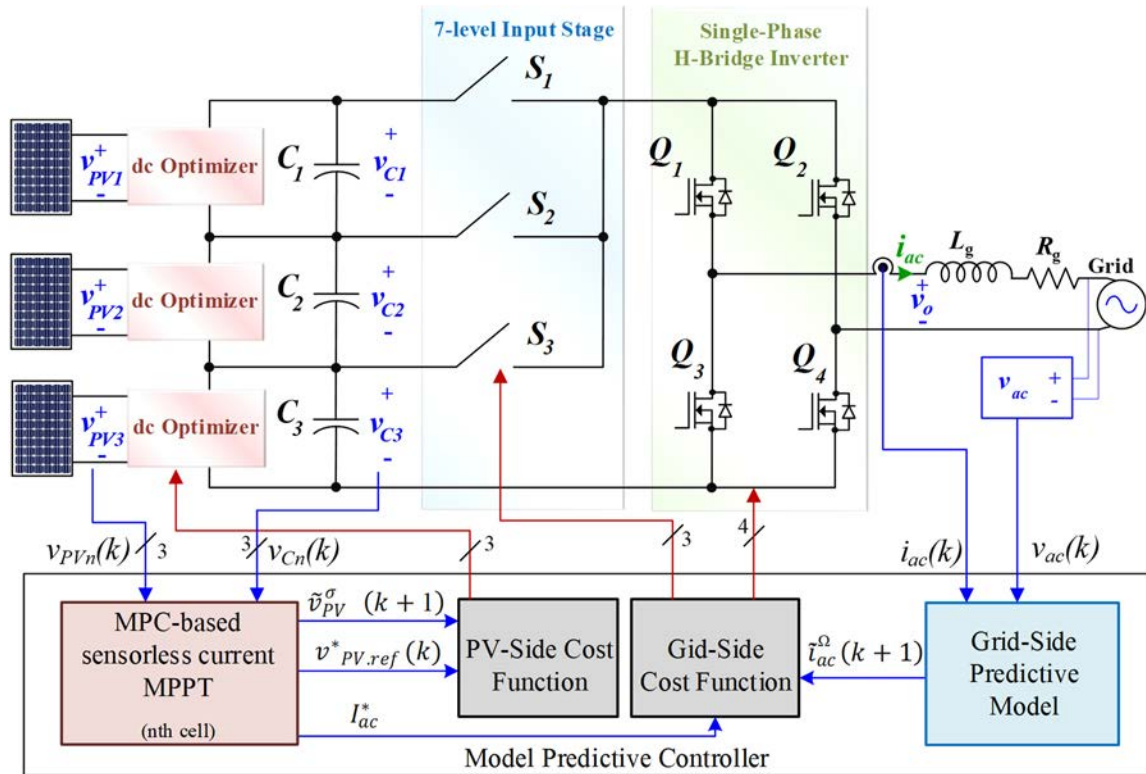


Figure 4.8 The block diagram of single-phase 7-level SMI in the PV generation system.

## 4.5. Simulation results

The SUNPOWER SPR-305-WHT is used as a PV module. In this simulation, an array of six PVs are simulated. Two parallel-connected modules are connected to each of the three dc optimizer cells of the 7-level sMI in Figure 4.8. The PV module characteristics

per dc optimizer (two parallel PV modules) under standard test condition (STC: solar irradiance = 1 kW/m<sup>2</sup>, cell temperature = 25 deg. C) is illustrated in Figure 4.9.

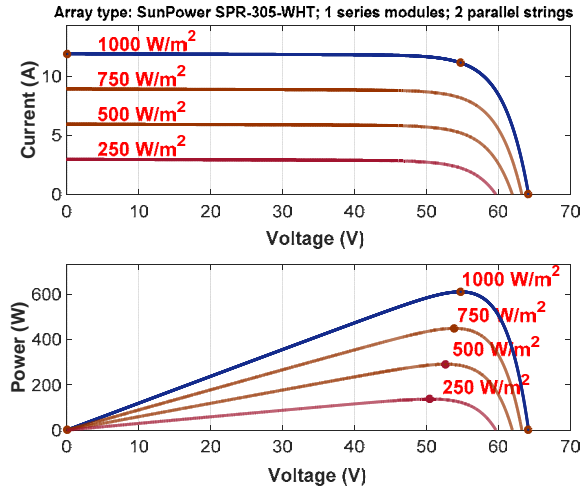


Figure 4.9 PV characteristics used in the simulation.

The control algorithm is implemented in Matlab/Simulink; the sampling time  $T_s$  is 10  $\mu$ s which corresponds to a sampling frequency of 100 kHz. This sampling time is chosen based on the capability of the dSPACE DS1007 platform processor, which is used for real-time implementation in this chapter. In a fixed step model predictive control, unlike controllers with a pulse-width modulator, the switching signals are directly manipulated. Thus the “switching frequency” can vary from one fixed sampling interval to the next. The sampling frequency should be much higher than the switching frequency to get a suitable performance controller, such as 20 times higher according to the guidelines for accurate modeling of power electronics [124, 143]. For well-behaved MPC systems, an “average switching frequency” could be estimated to offer some insights into

the operation of other aspects of the system. In this paper, the sampling frequency is 100 kHz, which results in an average switching frequency of 5 kHz for the dc optimizer blocks.

Using Matlab/Simulink, the irradiance profile in Figure 4.10 was applied to the PV-connected dc optimizers. The system is tested under two irradiance level changes. Figure 4.11, Figure 4.12 and Figure 4.13 demonstrate the simulation results for current, voltage, and power, respectively, of the proposed sensorless current MPC-based MPPT algorithm. As shown in the figures, the performance of the sensorless current MPC-based MPPT algorithm tracked the expected maximum power (Figure 4.13). Steady-state current ripple in Figure 4.11 is 1.5%, while voltage ripple in Figure 4.12 is 3.9%. The power plot during the transient response, Figure 4.13, shows a settling time of 0.055 seconds. The current injected to the grid, shown in Figure 4.14 during step change in solar irradiance, shows grid current tracking of the reference current provided by the current MPC. The total harmonic distortion (THD) of the grid current is 3.6%, Figure 4.15, which is within the IEEE 519 recommended practice for harmonic control [144]. The 7-level voltage is shown in Figure 4.16 for the output voltage, before filtering, of the sMI.

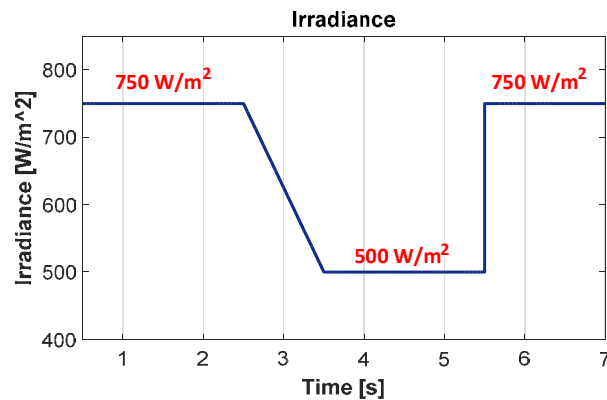


Figure 4.10 Solar irradiance profile.

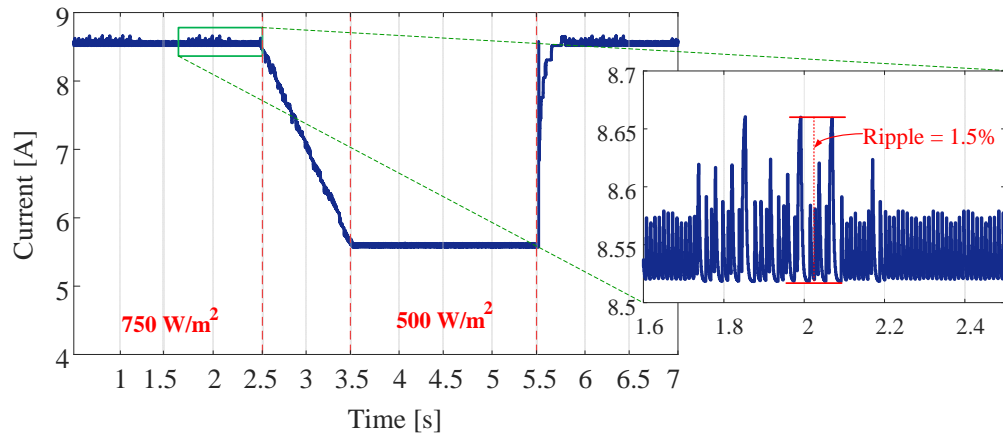


Figure 4.11 PV current using SC-MPC-MPPT and the current ripple.

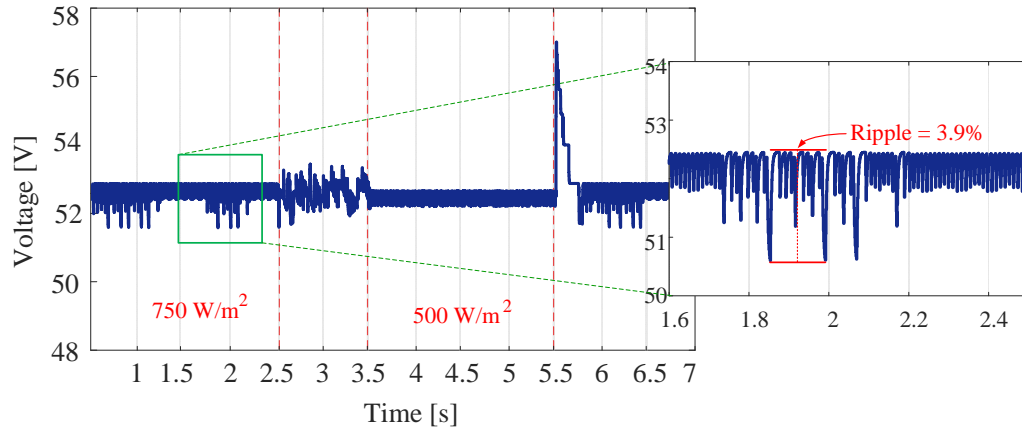


Figure 4.12 PV voltage using SC-MPC-MPPT and the voltage ripple.

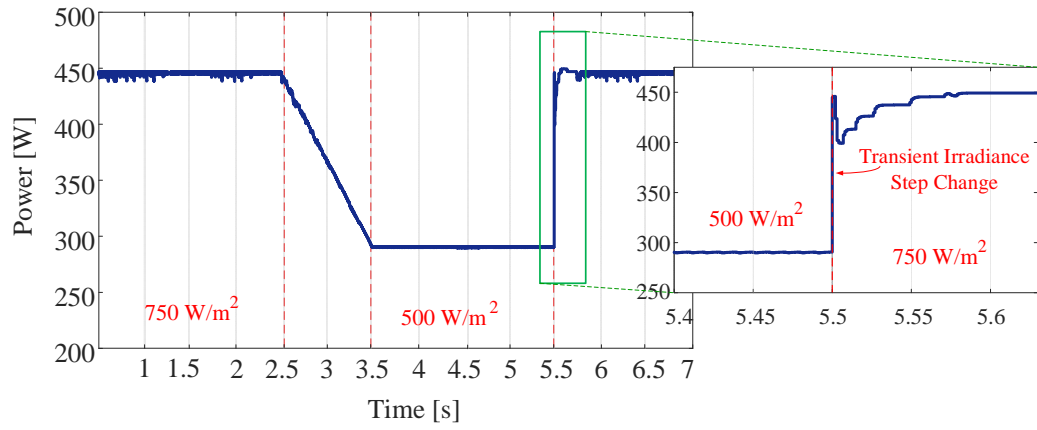


Figure 4.13 PV power using SC-MPC-MPPT and a zoomed-in plot of the PV power during transient step response.

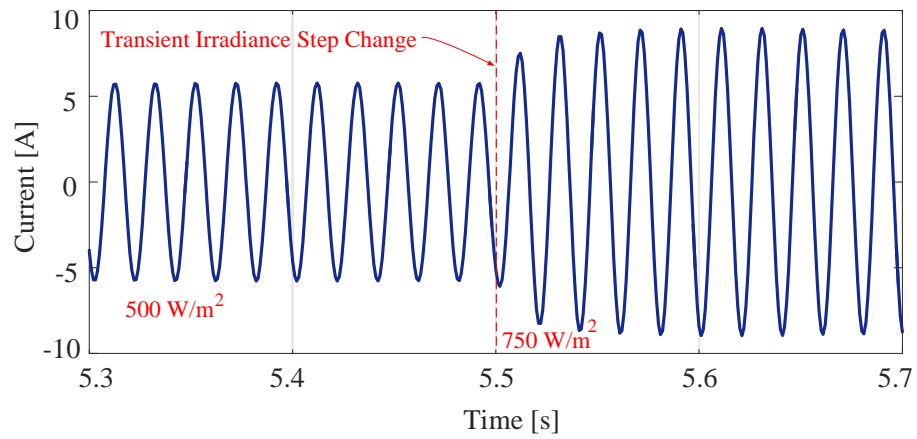


Figure 4.14 The response of the current fed to the grid by SMI to step-change in solar irradiance level.

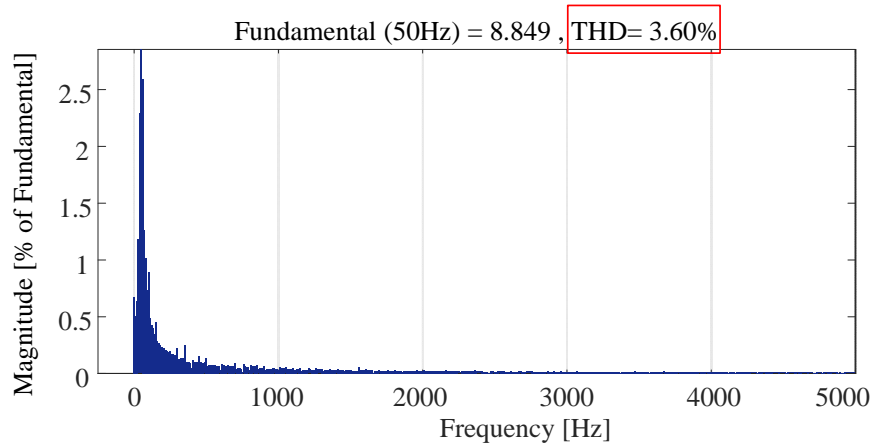


Figure 4.15 Total harmonic distortion in current fed to grid by sMI.

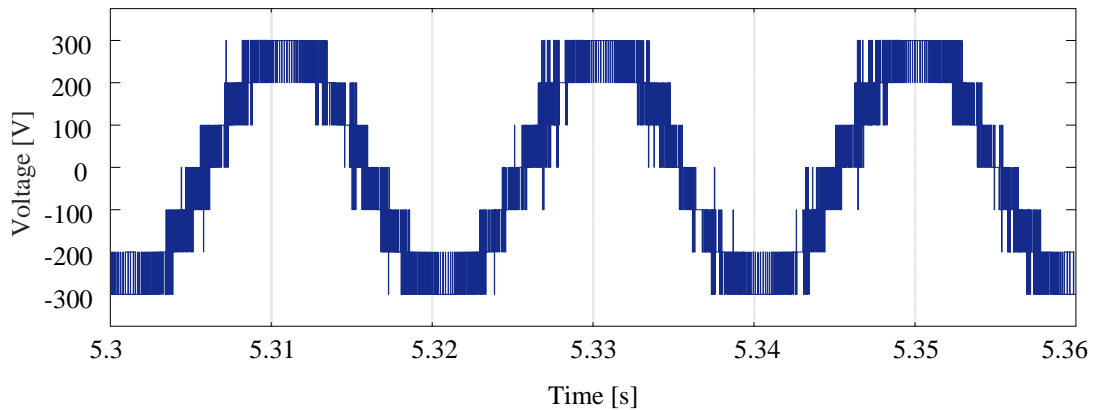


Figure 4.16 The output voltage of the sMI before the inductive filter.

Using the dSPACE DS1007 platform, the proposed MPPT controller was implemented in real-time, a step change response to solar irradiance level was applied to the system. The stability and fast dynamic response of the SC-MPC-MPPT to step-change in solar irradiance level from  $500 \text{ W/m}^2$  to  $750 \text{ W/m}^2$  were verified as in Figure 4.17. Figure 4.17 also shows zoomed-in plots of the steady-state performance at  $750 \text{ W/m}^2$  of the proposed technique. The oscillation around MPP for PV voltage and the current was observed to be 4.2% and 2.3%, respectively.



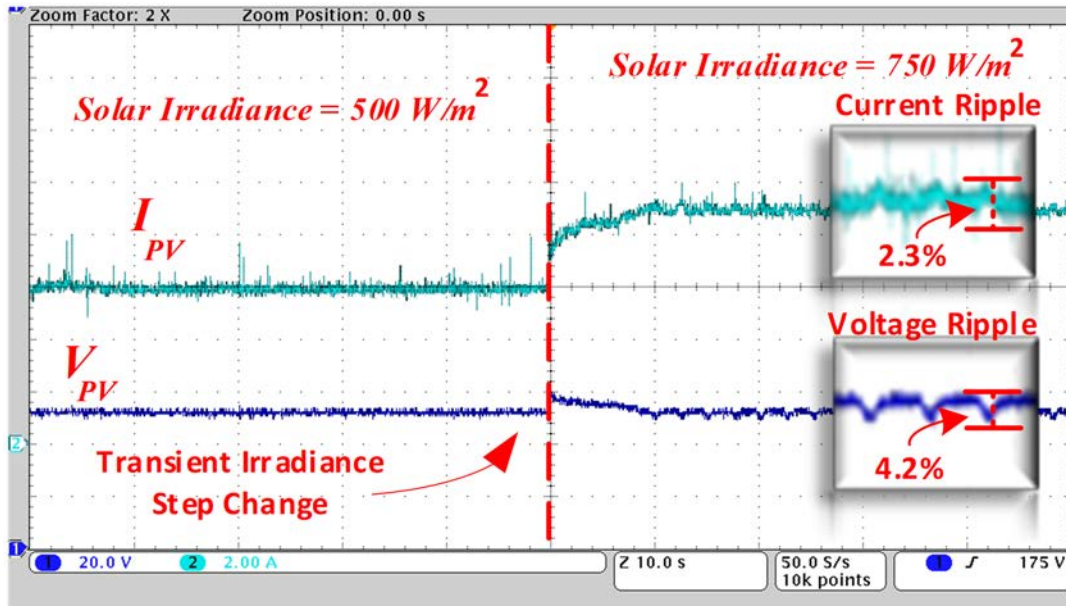


Figure 4.17 PV current and voltage under step change in solar irradiance level, along with zoomed-in plots of the ripples. Both the current and voltage track the MPP reference.

#### 4.6. Conclusion

This chapter looked into the application of the sensorless current MPPT algorithm within submodule PV power processing. The topology of the sub-multilevel inverter was considered as it uses less number of switches than conventional multilevel inverters (MI), which is noticeable at larger number of levels. The single-phase H-bridge inverter in the sMI topology uses the line frequency, which allows for lower switching losses when compared to conventional MIs. Also, the 7-level output voltage is not affected by the mismatch in the submodule voltages for the dc optimizer, making it suitable for the application in this chapter. This chapter demonstrated an MPC framework for both the MPPT controller for the cascaded dc optimizers and the inverter side grid current controller. The use of the developed sensorless current MPPT in this chapter for the cascaded dc power optimizers proved advantageous as a current sensor was eliminated for

each dc/dc converter. The topology running the proposed controller was presented, and the performance met the IEEE standards. The proposed controller for the sMI is extendable to higher levels (i.e., 16-level or 33-level).

## 5. MAXIMUM POWER POINT TRACKING IN A GRID-INTERACTIVE INVERTER – QUASI-Z-SOURCE INVERTER\*

### 5.1. Introduction

This chapter demonstrates an application example of the interaction between the proposed standalone MPPT algorithms in Chapter 3 with other grid-interactive converters. To comply with present ac grid standards, an inverter stage is used after the MPPT dc-dc converter to convert the voltage and current from dc to ac. This means that the PV power is passed through a two-stage system to be delivered to the grid, which can impose efficiency and integration issues, and increase the cost of the system [27]. The Z-source inverter (ZSI) is capable of overcoming this limitation as it can adjust the voltage level and invert the power in a single-stage [145] as shown in Figure 5.1. But while the ZSI can handle the wide voltage variation associated with PV, it also draws current discontinuously [146]. This aspect of the ZSI creates a problem for the PV array, which needs a constant output path for its dc current to avoid shortening its lifetime [147]. The quasi-ZSI (qZSI) is a modification of the ZSI which draws continuous dc current, which meets this criterion without the need for extra filtering capacitors [148]. The qZSI handles both the wide input voltage range and avoids current discontinuity in the PV modules [149].

---

\*Part of the data reported in this chapter is reprinted with permission from “Model Predictive Control for Maximum Power Point Tracking of Quasi-Z-Source Inverter Based Grid-Tied Photovoltaic Power System” by M. Metry, Y. Liu, R. S. Balog, and H. Abu-Rub, 2016. Presented at the IEEE Int. Symp. on Ind. Electron., Edinburgh, Scotland, UK, 19-21 Jun 2017, p. 1-6, Copyright © 2017 IEEE

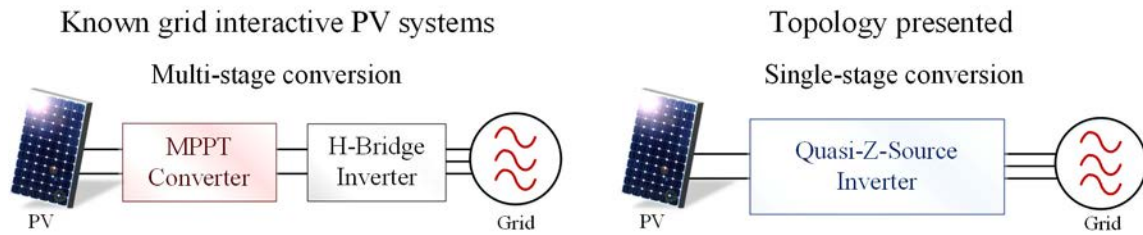


Figure 5.1 Known grid interactive PV systems (left) are comprised of multiple stage power processing which impacts system efficiency. The qZSI (right) is capable of both power conditioning of the PV input and grid current injection to the grid.

This chapter illustrates an approach to integrating MPC based MPPT controllers within the existing control loop of a three-phase grid-connected qZSI [150]. The topology of qZSI has an inherent advantage that allows two different control objectives to be achieved simultaneously. The use of an MPC-based MPPT controller reduces the settling time and significantly reduces steady-state ripple.

This chapter is organized as follows:

Section 5.2 presents the background on the quasi-Z-source inverter

Section 5.3 derives the MPC formulation

Section 5.4 presents simulation results including dynamic tests

Section 5.5 concludes the contribution of this chapter.

## 5.2. Background on the quasi-Z-source inverter topology

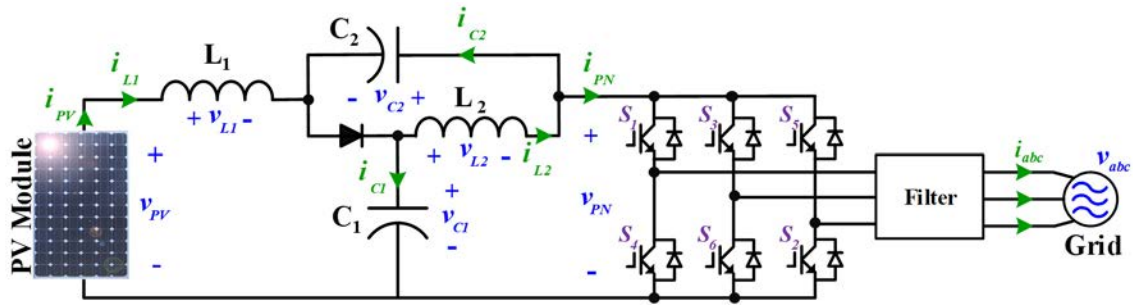


Figure 5.2 Three-phase grid-connected quasi-Z-source inverter topology for PV application.

### 5.2.1. Circuit analysis

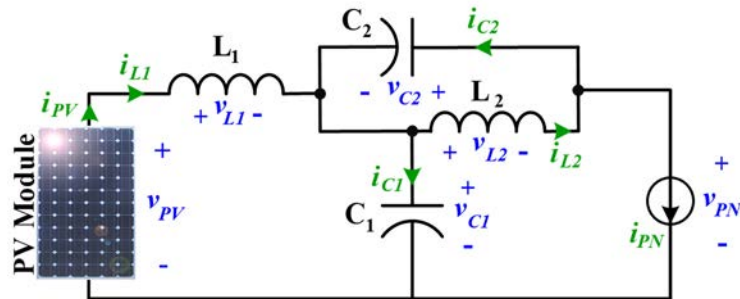


Figure 5.3 Analysis of qZSI in non-overlap mode.

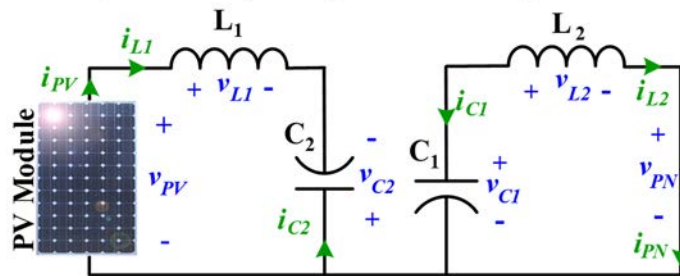


Figure 5.4 Analysis of qZSI in overlap mode.

Consider the qZSI topology in Figure 5.2, the qZSI operates in two main modes. The first mode corresponds to the period of non-overlap when current flows from the PV module, through the inverter bridge, to the ac output. The second mode involves the conduction overlap of two transistors on the same phase leg of the inverter bridge. This

restricts the input current to the  $LC$  network within the qZSI, but provides voltage boost. Taking a closer look at non-overlap mode, Figure 5.3 shows the equivalent circuit with the conducting diode shorted out and current  $i_{PN}$  representing the current from the qZSI into the inverter bridge leg. Relevant equations of analyzing the non-overlap mode are [149, 151, 152]:

$$v_{L1}(t) = v_{PV} - v_{C1} \quad (5.82)$$

$$i_{C1}(t) = i_{L1} - i_{PN} \quad (5.83)$$

$$i_{C2}(t) = i_{L2} - i_{PN} \quad (5.84)$$

During overlap mode, Figure 5.4, a short-circuit path allows capacitor  $C_1$  to charge inductor  $L_2$ . At the same time, the input voltage source,  $V_{PV}$ , and capacitor  $C_2$  charge  $L_1$ .

Relevant equations of analyzing overlap mode are:

$$v_{L1}(t) = v_{PV} + v_{C2} \quad (5.85)$$

$$i_{C1}(t) = -i_{L2} \quad (5.86)$$

$$i_{C2}(t) = -i_{L1} \quad (5.87)$$

Further analysis leads to the following relations:

$$i_{L1} = i_{L2} = i_{PV} \quad (5.88)$$

$$\frac{v_{PV}}{v_{PN}} = 1 - 2D \quad (5.89)$$

$$v_{PV} = v_{C1} - v_{C2} \quad (5.90)$$

where  $D$  is the overlap period proportion to the sampling period  $T$ .

### 5.3. Developing the MPC formulation

The block diagram of the proposed qZSI control strategy is shown in Figure 5.6. The control algorithm is divided into two segments: first, the PV generation system that uses MPC-MPPT algorithm to determine the appropriate overlap period required to operate at MPP. Second is the grid-side active-reactive power control, so-called PQ decoupling control, to ensure unity power factor integration into the grid. The active power reference is determined by the MPC-MPPT. Then the PV power delivered to the grid is achieved through regulating the modulation signals, which are fed along with the overlap duty cycle,  $D$ , to a simple boost PWM that determines the switching state for the six inverter switches. The focus of this chapter is on the integration of the MPC based MPPT method with the qZSI existing controllers. MPC based PQ decoupling has been explained in [153] In other words, MPC-MPPT determines the overlap period,  $D$ , while the grid-side PQ decoupling control determines the modulation index,  $M$  (Figure 5.5).

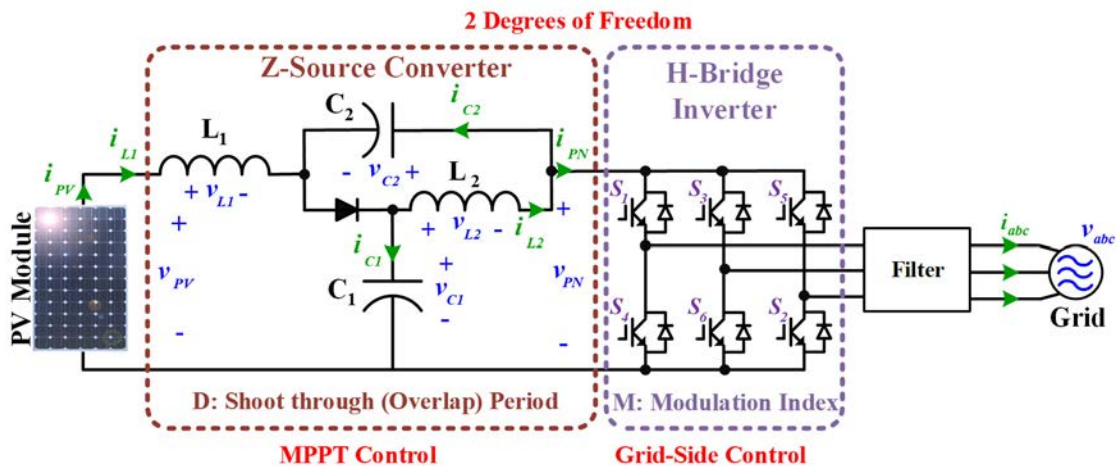


Figure 5.5 MPC-MPPT determines the overlap period, while the grid-side PQ decoupling control determines the modulation index,  $M$ . The advantage of qZSI topology is its single-stage power processing of PV systems. The single-power processing is made possible as the control of a qZSI has two degrees of freedom.

### 5.3.1. MPC-MPPT for PV side

MPPT is used to ensure the maximum available solar energy harness from the solar module [115, 154, 155]. MPPT algorithm, using predicted values from model equations, determines the reference current for the cost function, which determines the next switching state. The prediction is based upon minimizing the cost function  $g$ , illustrated in Figure 5.6, so as the switching state (plant 1: non-overlap mode or plant 2: overlap mode) that results in the suitable control actuation is selected. The inputs to the predictive controller are the PV voltage, PV current, and capacitor voltages.

The discrete-time set of equations enables the behavior of the system in response to the selected control actuation to be predicted for the next sampling time  $k+1$ . The proposed methodology is based on the fact that the slope of the PV array power curve is zero at the predicted MPP, positive on the left, and negative on the right of the predicted MPP.

The discrete-time voltage and current set of equations for the qZSI, in non-overlap mode ( $\sigma = 1$ ) are based on (5.82), (5.83), (5.84) and (5.88), and are given by (5.91), (5.92) and (5.93). In overlap mode ( $\sigma = 0$ ), relations are based on (5.85), (5.86), (5.87) and (5.88), and are given by (5.94), (5.95) and (5.96).

$$i_{PV}(k+1) = \frac{v_{PV}(k) - v_{C1}(k)}{L_1}(DT) + i_{PV}(k) \quad (5.91)$$

$$v_{C1}(k+1) = \frac{i_{PV}(k) - i_{PN}(k)}{C_1}(DT) + v_{C1}(k) \quad (5.92)$$

$$v_{C2}(k+1) = \frac{i_{PV}(k) - i_{PN}(k)}{C_2}(DT) + v_{C2}(k) \quad (5.93)$$

$$i_{PV}(k+1) = \frac{v_{PV}(k) + v_{C2}(k)}{L_2}(1-D)T + i_{PV}(k) \quad (5.94)$$



$$v_{C1}(k+1) = \frac{i_{PV}(k) - i_{PN}(k)}{C_1}(1-D)T + v_{C1}(k) \quad (5.95)$$

$$v_{C2}(k+1) = \frac{i_{PV}(k) - i_{PN}(k)}{C_2}(1-D)T + v_{C2}(k) \quad (5.96)$$

Since  $D$  represents the average time for the overlap mode, it can be replaced by the switching state in the average model during operation of MPC-MPPT. The average PV voltage and current models are necessary for the cost function and are based on (5.90) to (5.91):

$$i_{PV}(k+1) = i_{PV}(k) + (v_{PV}(k) - v_{C1}(k))\frac{S}{L_1} + (v_{PV}(k) + v_{C2}(k))\frac{1-S}{L_2} \quad (5.97)$$

$$v_{PV}(k+1) = v_{C1}(k+1) - v_{C2}(k+1) = \frac{i_{PV}(k) - i_{PN}(k)}{C_1} - \frac{i_{PV}(k) - i_{PN}(k)}{C_2} + v_{PV}(k) \quad (5.98)$$

The predicted PV voltage and current are used to determine the  $d$ -axis reference current, as shown in Figure 5.6. Now after determination of the reference current and the predicted PV current, the cost function subject to minimization can be obtained as follows

$$g_{\sigma \in \{0,1\}} = \left| I_{PV, \sigma \in \{0,1\}}(k+1) - I_{ref, PV}(k+1) \right| \quad (5.99)$$

where  $\sigma \in \{0,1\}$  presents the switching state.

### 5.3.2. Grid-side PQ decoupling control

The predicted active power reference  $P_{ref-PV}(k+1)$ , obtained from the MPC-MPPT algorithm using the predicted voltage and current values, is then used to obtain the  $d$ -axis current reference  $i_d^*$  through  $i_d^* = (2/3)P_{ref-PV}/v_d$ ; meanwhile, the  $i_q^*$  is set to zero to have unity power factor. As shown in Fig. 3, the three-phase actual grid voltage  $v_{abc}$  and grid-tie current  $i_{abc}$  are transferred to the two-phase rotating coordinates in  $d$  and  $q$  components,

respectively. The Phase-Locked Loop (PLL) is applied to obtain the phase of grid voltage, in order to make the grid-tie current in phase with the grid voltage.

The error between the reference and actual currents going through the proportional-integral (PI) controller determines the voltage references  $u_d^*$  and  $u_q^*$  in  $d$  and  $q$  components. Then, through the  $dq-abc$  transformation, the voltage references  $u_a^*$ ,  $u_b^*$ , and  $u_c^*$  in per unit value and the overlap duty cycle from the proposed MPC-MPPT are applied to generate gate drive signals by the simple boost control of the qZSI.

### **5.3.3. Overall controller**

The MPC based MPPT controller is integrated within the qZSI as shown in Figure 5.6. The predictive model for the PV side controller is shown in (5.97) and (5.98). The cost function for the PV side controller is shown in (5.99).

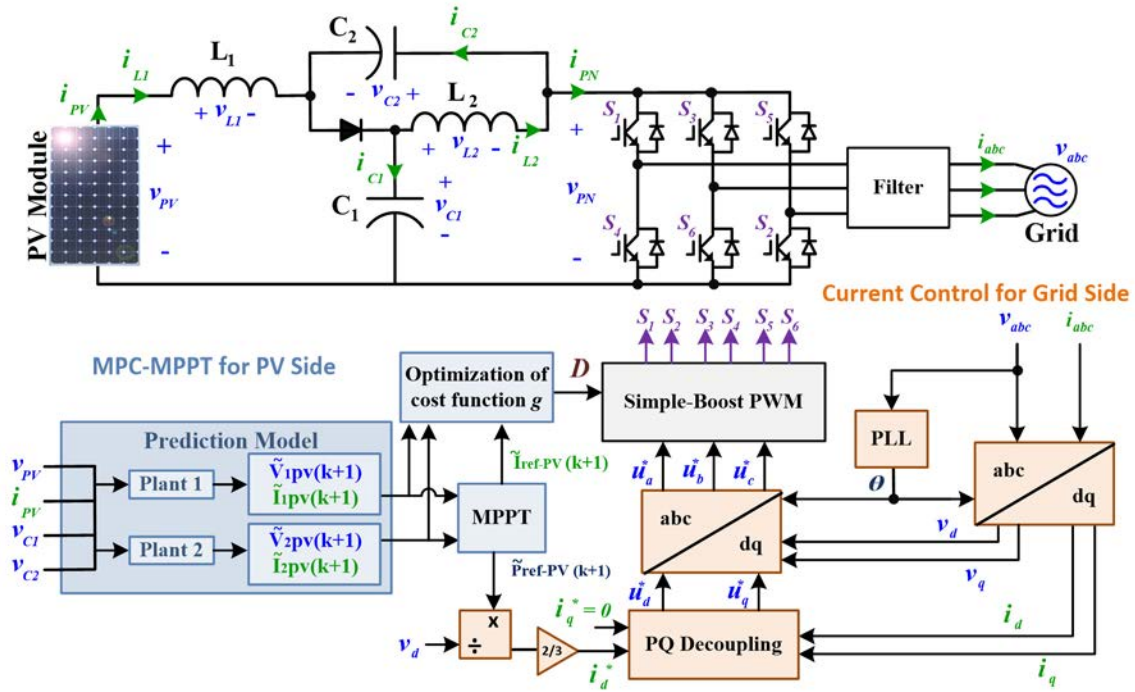


Figure 5.6 The control block diagram of three-phase qZSI in PV generation system.

#### 5.4. Simulation results

In the investigations, the SUNPOWER SPR-305-WHT is used as PV module. Two modules are connected in parallel under standard test condition (STC: solar irradiance = 1 kW/m<sup>2</sup>, cell temperature = 25 deg. C). The control algorithm is simulated using Matlab/Simulink software; the sampling time  $T_s$  is 10  $\mu s$ , which corresponds to a sampling frequency of 100 kHz. In a fixed-step model predictive control unlike controllers with pulse-width modulator, the switching signals are directly generated, thus the “switching frequency” can vary from one fixed sampling interval to the next. The sampling frequency should be much higher than the switching frequency in order to get good performance controller, such as 20 times higher according to the guidelines for accurate modeling of power electronics [124, 143]. For well-behaved MPC systems, we can compute an

“average switching frequency”, which may offer some insights into the operation of other aspects of the system. In this paper, the sampling frequency is 100 kHz, which results in an average switching frequency of 5 kHz.

Table 5.1 Simulation parameters of the qZSI system

Parameter	Value
PV power at 750 W/m <sup>2</sup>	4000 W
Capacitors ( $C_1$ & $C_2$ )	470 $\mu$ F
Inductors ( $L_1$ & $L_2$ )	500 $\mu$ H
Nominal frequency ( $f_o$ )	50 Hz
Average Switching Frequency	5 kHz
RMS grid ph-ph voltage	208 V
Sampling time ( $T_s$ )	10 $\mu$ s

System parameters are as shown in Table 5.1. Three-phase qZSI was connected to two parallel strings of 10 arrays of PVs in simulation and a step change in irradiance was applied once for the qZSI with P&O MPPT and again for the qZSI with MPC-MPPT. The comparison of performance is as shown in Figure 5.7. The PV current, voltage and power of the MPC-MPPT in Figure 5.7 (d), (e) and (f) has a smaller settling time, a lower ripple and smaller steady state error than the PV current, voltage and power of the P&O MPPT in Figure 5.7 (a), (b) and (c). The transient effect on grid current is as shown in Figure 5.7 (g). A zoomed-in plot of the grid current at steady state is shown in Figure 5.7 (h). The total harmonic distortion in the grid current is 1.16% as shown in Figure 5.7 (i), this meets with the IEEE 519 standard [144].

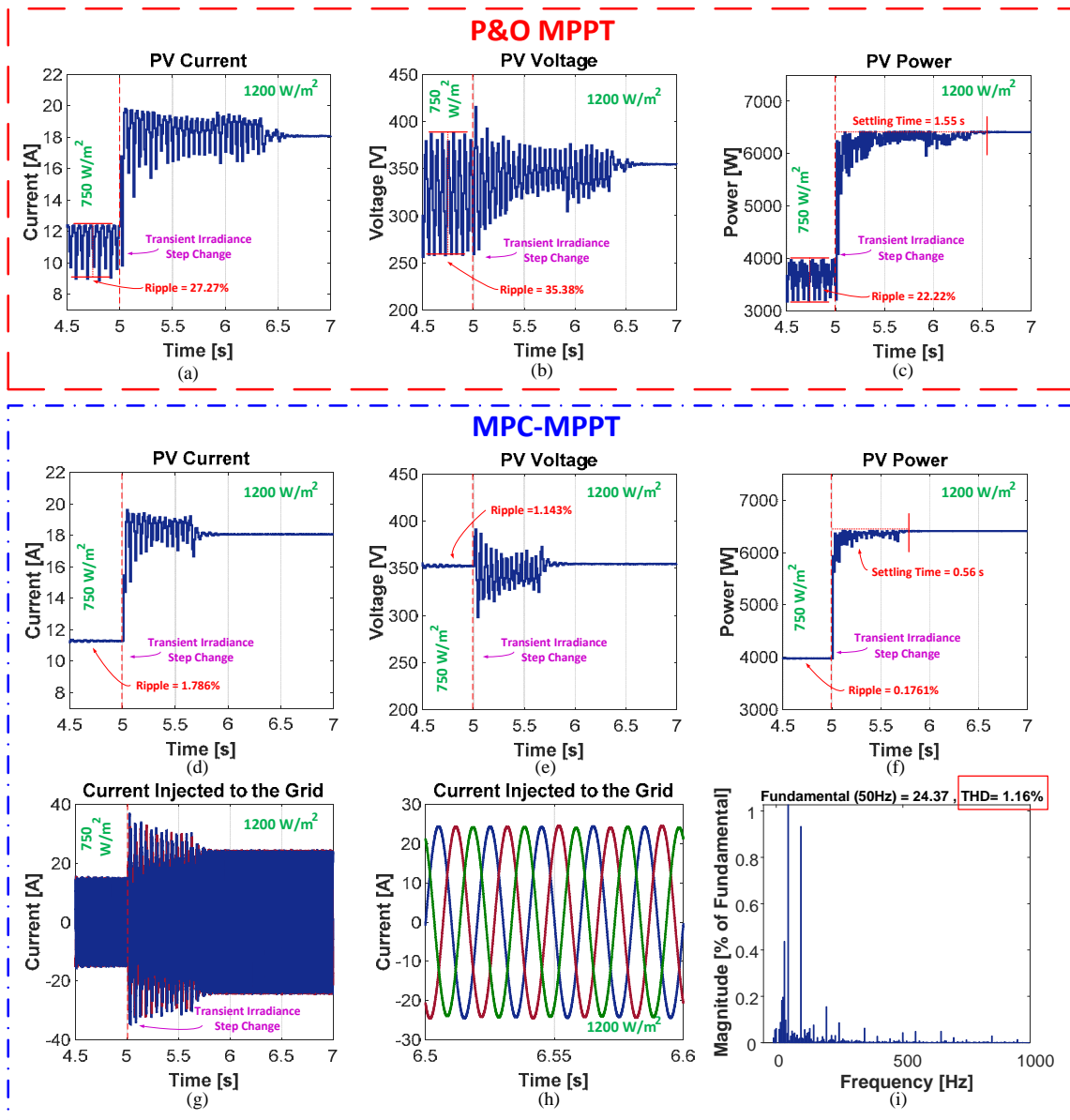


Figure 5.7 Simulation results. (a) PV current using P&O MPPT. (b) PV voltage using P&O MPPT. (c) PV power using P&O MPPT. (d) PV current using MPC-MPPT. (e) PV voltage using MPC-MPPT. (f) PV power using MPC-MPPT. (g) Response of the current fed to grid by qZSI to step change in solar irradiance level. (h) Zoomed in plot of the current fed to grid by qZSI. (i) Total harmonic distortion in current fed to grid by qZSI.

## **5.5. Conclusion**

This chapter illustrated an approach to integrating MPC based MPPT controllers within the existing control loop of a three-phase grid-connected qZSI. The topology of qZSI has an inherent advantage that allows two different control objectives to be achieved simultaneously. Such an advantage, in turn, eliminates the need for two-stage power processing for PV applications. The use of an MPC-based MPPT controller reduces the settling time and significantly reduces steady-state ripple. The results of the qZSI running the proposed controller presented complied with IEEE standards.

## 6. DOUBLE-FREQUENCY POWER RIPPLE CONTROLLER\*

### 6.1. Introduction

Rooftop solar and utility-scale photovoltaic (PV) installations are becoming very popular, which made it necessary to produce highly efficient and low-cost single-phase inverters. Single-phase grid-tied inverters have a characteristic double frequency power ripple. This low-frequency ripple could negatively impact the maximum power point tracking (MPPT) of the converter and reduce energy harvested from the PV source [127].

A capacitor is designed at the dc bus to filter out this double frequency ripple. However, since the ripple is double the grid frequency (100-120 Hz), which is a relatively low cutoff frequency compared to the inverter switching frequency, the bus capacitor ought to be of large value. Such huge capacitance is usually made available by electrolytic capacitors, which suffer in terms of reliability [156].

Power decoupling techniques have been of interest in the literature, and some are discussed in [157]. Active filtering techniques are discussed widely because they are known to handle a larger amount of ripple by redirecting the ripple power flow through another circuit [158-164]. One of the active filtering techniques, the ripple-port module integrated inverter (RP-MII), is proposed in [162-164]. The ripple port is essentially an H-bridge that is attached to the link capacitor and is modulated with pulse width modulation (PWM). Such a ripple port integrated inverter provides the advantage of significantly

---

\*Part of the data reported in this chapter is reprinted with permission from “A Hill-Climbing Optimization Approach for Closed-Loop Auto-Tuning of the Grid-Connected Ripple-Port Inverters” by M. Metry, M. Kim, and R. S. Balog, 2019. Presented at the IEEE Int. Conf. on Power Electron. – ECCE Asia (ICPE 2019-ECCE Asia), Busan, Korea, 27-30 May 2019, p. 1-6, Copyright © 2019 IEEE

reducing the amount of maximum voltage and the maximum power that the dc-link capacitor has to store. Hence, the capacitor size required to regulate the double frequency ripple to the desired percentage is reduced. Henceforth, the link capacitor employed can be a high-reliability ceramic capacitor instead of the short-life electrolytic capacitors. This argument is well established with reliability assessments, experimental setups and minimum energy capacitance requirements explained in [158] and [159]. In [160], this ripple port is implemented on a power factor correction (PFC) rectifier.

These papers, however, do not discuss all the factors that affect the effectiveness of the ripple port inverter, such as changes in grid dynamics, and ac filter and the ripple port LC filter phase angle. Also, these references do not provide a closed-loop controller that guarantees continuous ripple cancellation throughout the circuit's operation. Designing a closed-loop controller for the RP-MII using PID controllers proves challenging for multiple control loops concurrently; i.e. grid current injection, power quality regulation, dc-link voltage regulation, and maximum power point tracking.

This chapter provides a mathematical formulation of the different factors that affect the ripple port inverter tuning. This chapter also presents a closed-loop framework based on model predictive control (MPC) to automatically tune the ripple port inverter to minimize the dc-link dual-frequency ripple. Using the multi-objective optimization of MPC, it is demonstrated that the RP-MII achieves low dc-link voltage ripple while using small dc-link capacitor values, while the grid current is regulated [165].

This chapter is organized as follows:

Section 6.2 presents the background on the ripple port microinverter



Section 6.3 demonstrates the motivation for the closed-loop controller of the ripple port

Section 6.4 derives the MPC formulation

Section 6.5 presents simulation results including dynamic tests

Section 6.6 concludes the contribution of this chapter.

## 6.2. Background on the ripple port microinverter topology

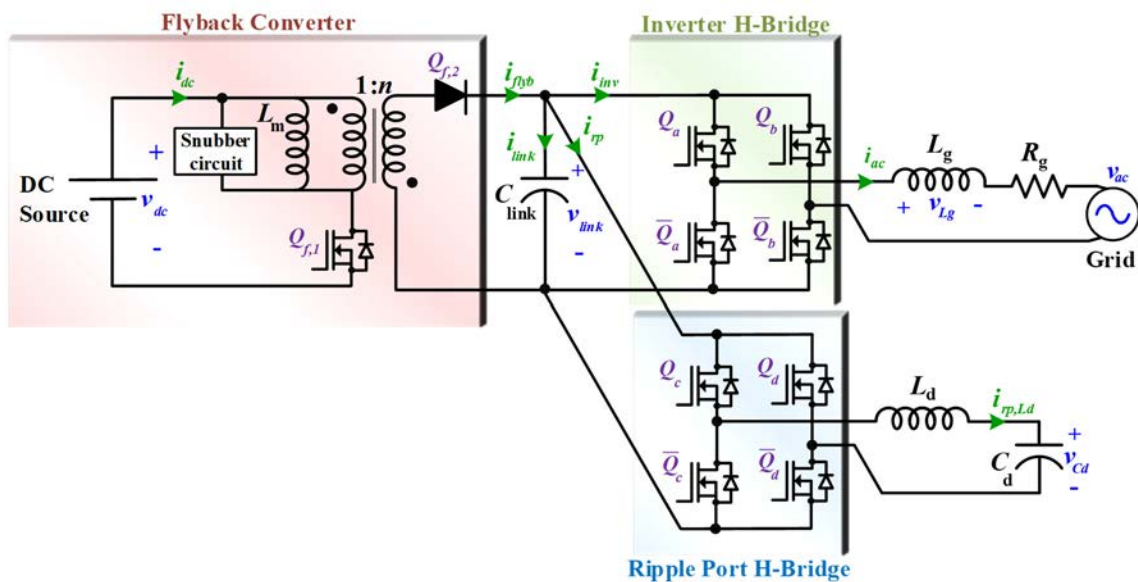


Figure 6.1 Ripple port circuit schematic.

The equations for the ripple port for a single-phase grid-tied inverter, shown in Figure 3.3, were discussed in [162] and [163]. This section aims to provide a more in-depth formulation of the concept developed in those papers. For example, [162] and [163] do not show the link capacitor value that is required by the topology. Also, [162] and [163] neither discuss the effect the LC filter has on the ripple cancellation nor the phase delay of the output current. Therefore, in this chapter, new equations, which can help the user

understand the ripple port behavior more clearly, are discussed. The instantaneous output power can be represented by an arbitrary displacement power factor with voltage and current phase angles,  $\theta_{vg}$  and  $\theta_{ig}$  respectively.

$$v_g = V_g \cos(\omega t - \theta_{vg}) \quad (6.100)$$

$$i_g = I_g \cos(\omega t - \theta_{ig}) \quad (6.101)$$

$$p_g = \frac{V_g I_g}{2} \cos(\theta_{vg} - \theta_{ig}) + \frac{V_g I_g}{2} \cos(2\omega t - \theta_{vg} + \theta_{ig}) \quad (6.102)$$

Assuming the amplitude change of the LC filter is negligible, only the phase shift of the voltage ( $\theta_{vo} - \theta_{vg}$ ) and the phase shift of the current, ( $\theta_{io} - \theta_{ig}$ ) are considered.

The output power before the LC filter can be written as

$$v_o = V_g \cos(\omega t - \theta_{vo}) \quad (6.103)$$

$$i_o = I_g \cos(\omega t - \theta_{io}) \quad (6.104)$$

$$p_o = \frac{V_g I_g}{2} \cos(\theta_{vo} - \theta_{io}) + \frac{V_g I_g}{2} \cos(2\omega t - \theta_{vo} - \theta_{io}) \quad (6.105)$$

dc power is supplied by power source, so the dc part of  $p_g$  is  $P_{dc}$ . Therefore,

$$P_{dc} = \frac{V_g I_g}{2} \cos(\theta_{vo} - \theta_{io}) \quad (6.106)$$

The ac part of  $p_g$  should be filtered by the ripple port capacitor. Whereas, the ripple port adds some phase angle  $\theta_{rp}$ , assuming the ripple port inductor value is much smaller than that of the capacitor, the power in the ripple port is

$$v_{cd} = V_{cd} \cos(\omega t + \theta_{rp}) \quad (6.107)$$

$$i_{rp,Ld} = \omega C_d V_{cd} \sin(\omega t + \theta_{rp}) \quad (6.108)$$

$$p_{cd} = -\frac{\omega C_d V_{cd}^2}{2} \sin(2\omega t + 2\theta_{rp}) \quad (6.109)$$

where the subscript  $d$  refers to the decoupling ripple port,  $p_{Cd}$ , refers to the ripple port power, and  $v_{Cd}$  is the voltage across the ripple port capacitor.

The ac part of  $p_o$  should be the same as the ripple port power and the power in the dc-link capacitor  $C_{link}$ . Therefore,

$$p_o - P_{dc} = p_{Cd} + p_{C,link} \quad (6.110)$$

$$\frac{V_g I_g}{2} \cos(2\omega t - \theta_{vo} - \theta_{io}) = -\frac{\omega C_d V_{Cd}^2}{2} \sin(2\omega t + 2\theta_{rp}) + p_{C,link} \quad (6.111)$$

where  $p_{C,link}$  refers to the instantaneous power across the dc-link capacitor  $C_d$ . Thus,  $\theta_{rp}$  can be determined from equation (6.112)

$$\cos(2\omega t - \theta_{vo} - \theta_{io}) = -\sin(2\omega t + 2\theta_{rp}) \quad (6.112)$$

$$2\omega t - \theta_{vo} - \theta_{io} = 2\omega t + 2\theta_{rp} + \pi/2 \quad (6.113)$$

$$\theta_{rp} = -\frac{\theta_{vo}}{2} - \frac{\theta_{io}}{2} - \frac{\pi}{4} \quad (6.114)$$

From (6.111) and (6.114),

$$V_{Cd} = \sqrt{\frac{V_g I_g}{\omega C_d}} + \text{ripple voltage on } C_{link} \quad (6.115)$$

the maximum voltage ripple amplitude at  $C_{link}$  is  $\Delta V_{link}$ . Thus, the ripple value on  $V_{Cd}$  can be estimated from equation (6.115)

$$\sqrt{\frac{V_g I_g}{\omega C_d}} - \Delta V_{link} \leq V_{C,d} \leq \sqrt{\frac{V_g I_g}{\omega C_d}} + \Delta V_{link} \quad (6.116)$$

The amplitude of the voltage ripple at the link capacitor is determined by this equation

$$\Delta V_{link} = \frac{P_{dc}}{\omega V_{dc} C_{link}} \quad (6.117)$$

Therefore, from equation (6.116) and (6.117), the maximum voltage at the ripple port is

$$\sqrt{\frac{V_g I_g}{\omega C_d} - \frac{P_{dc}}{\omega V_{dc} C_{link}}} \leq V_{C,d} \leq \sqrt{\frac{V_g I_g}{\omega C_d} + \frac{P_{dc}}{\omega V_{dc} C_{link}}} \quad (6.118)$$

### 6.3. The motivation for a closed-loop controller for ripple port

Factors that change the grid-tied inverter characteristics during operation are various, as outlined in the formulation of the previous section. These factors include grid dynamics, filter phase shift, and the H-bridge switching action. Since the RP-MII operates in an open-loop as in [162] and [163], such factors are not accounted for, which could lead to suboptimal performance. The main objective of the closed-loop controller of the RP-MII is to minimize the dual-frequency ripple on the dc-link capacitor. The challenge with designing the controller is for the commutation to be done precisely to reduce the double frequency ripple without impacting other performance measures – power factor (PF) and total harmonic distortion (THD).

#### 6.3.1. Parametric sweep study

One way to quantify this dc-link voltage ripple is to use a rectifier figure of merit: Form Factor (FF), which is defined as the RMS value of the signal divided by its average value [60]. In this chapter, however, the inverse FF is used and is defined as in (6.119), whereas  $FF^{-1}$  is a value in the set (0,1]. The objective of the controller is to achieve the ideal  $FF^{-1} = 1$ . Without loss of generality, if the grid voltage is distorted (e.g. a third-harmonic distortion), the objective of the controller is simply to maximize the  $FF^{-1}$  term.

$$FF^{-1} = \frac{V_{ave,dc}}{V_{RMS,dc}} \quad (6.119)$$

To develop a better understanding of the characteristics of the ripple port  $FF^{-1}$  related to the phase angle and modulation index, a full parametric sweep was performed as in Figure 6.2. The parametric sweep was performed on the modulation index, and phase angle of a pulse-width modulated H-bridge inverter. The objective is to determine whether the combination of modulation index ( $Mod(k)$ ) and phase angle ( $Ang(k)$ ) within the ripple port generate a unique extremum at which the dc-link voltage ripple ( $V_{Link}$ ) is minimized. Hence, the ripple port inverter  $Mod(k)$  is varied from 0.1 to 0.7 and the inverter  $Ang(k)$  is varied from 30 to 60 degrees. Figure 6.2(a) and (b) indicate the presence of a global minimum point at which the capacitor link voltage ripple is minimized to 2% at a modulation index of 0.38 and a phase angle of 49 degrees. Such a result was achieved by manually tuning ripple port parameters without the addition of any bulky capacitors at the dc link.

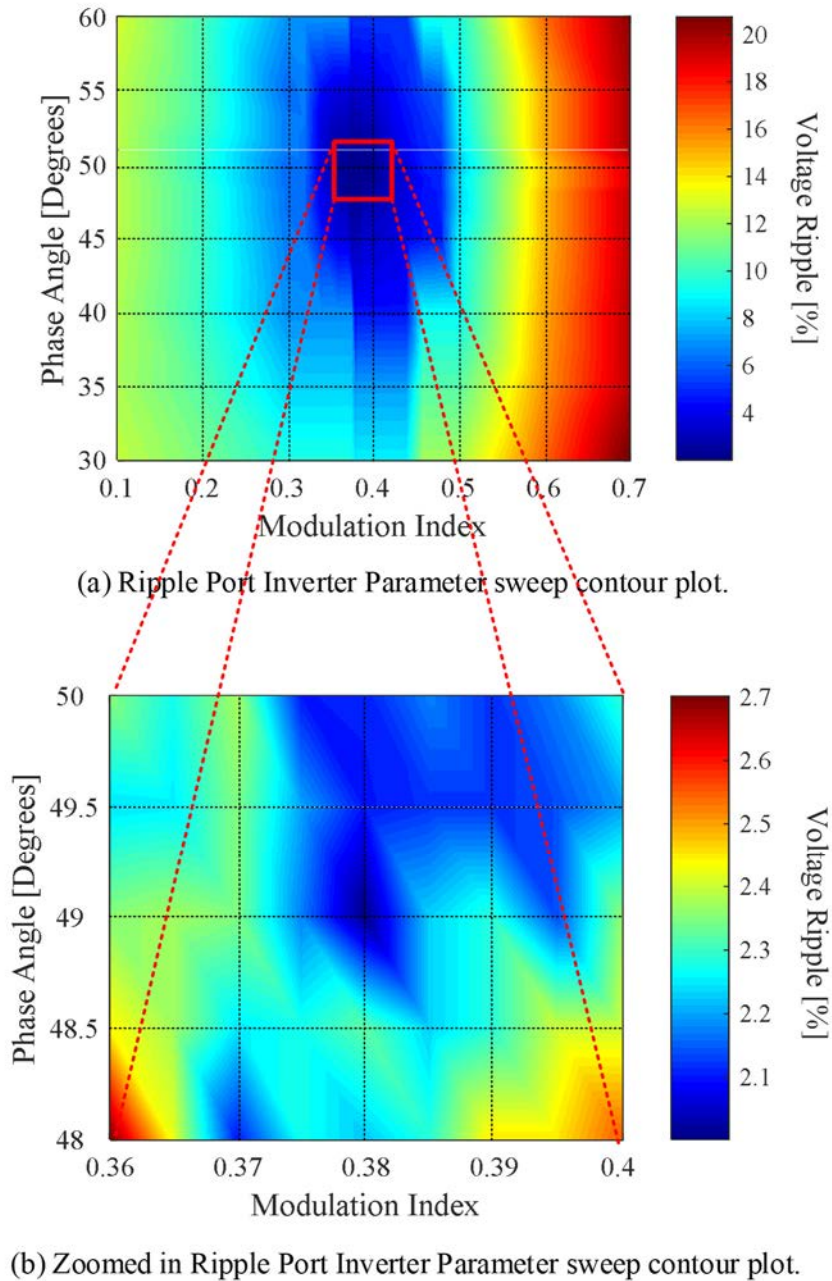


Figure 6.2 Full parametric sweep. (a) Ripple Port Inverter Parameter sweep contour plot with modulation index varied from 0.1 to 0.7, and the inverter phase angle varied from 30 to 60 degrees. (b) Zoomed in Ripple Port Inverter Parameter sweep contour plot with modulation index varied from 0.36 to 0.4, and the inverter phase angle varied from 48 to 50 degrees. This parametric sweep indicates the presence of a global minimum point at which the capacitor link voltage ripple is minimized to 2% at a modulation index of 0.38 and a phase angle of 49 degrees.

The conclusion is drawn from Figure 6.2 (a) and (b) indicates that an extremum-seeking/hill-climbing algorithm can be used to locate the set  $[Mod(k), Ang(k)]$  at which the  $V_{Link}$  ripple is minimized ( $FF^{-1}$  is maximized). Such a conclusion indicates that the RP-MII control characteristics are convex in nature.

### 6.3.2. Modulator based closed-loop controller based on the hill-climbing algorithm

A modulator based closed-loop controller is developed based on extremum seeking algorithm using the form factor of the dc-link voltage as a control variable. Based on Figure 6.1, the  $FF^{-1}$  for  $V_{Link}$  is calculated as

$$FF^{-1}(k) = \frac{V_{Link,ave}}{V_{Link,RMS}} \quad (6.120)$$

Then the difference between the present value  $FF^{-1}(k)$  and the previous step value  $FF^{-1}(k - 1)$  is calculated as

$$\Delta FF = FF^{-1}(k) - FF^{-1}(k - 1) \quad (6.121)$$

The objective of this algorithm is to maximize  $FF^{-1}(k)$ . Hence, if  $\Delta FF$  is a negative value, then  $Mod(k - 1)$  and  $Ang(k - 1)$  are incremented by some small value  $\Delta Mod$  and  $\Delta Ang$  respectively. Otherwise, they are decremented. The resulting  $[Mod(k), Ang(k)]$  set is then used to generate the reference signals for the ripple port H-bridge controller. This algorithm is based on the hill-climbing optimization method and is as shown in Figure 6.3.

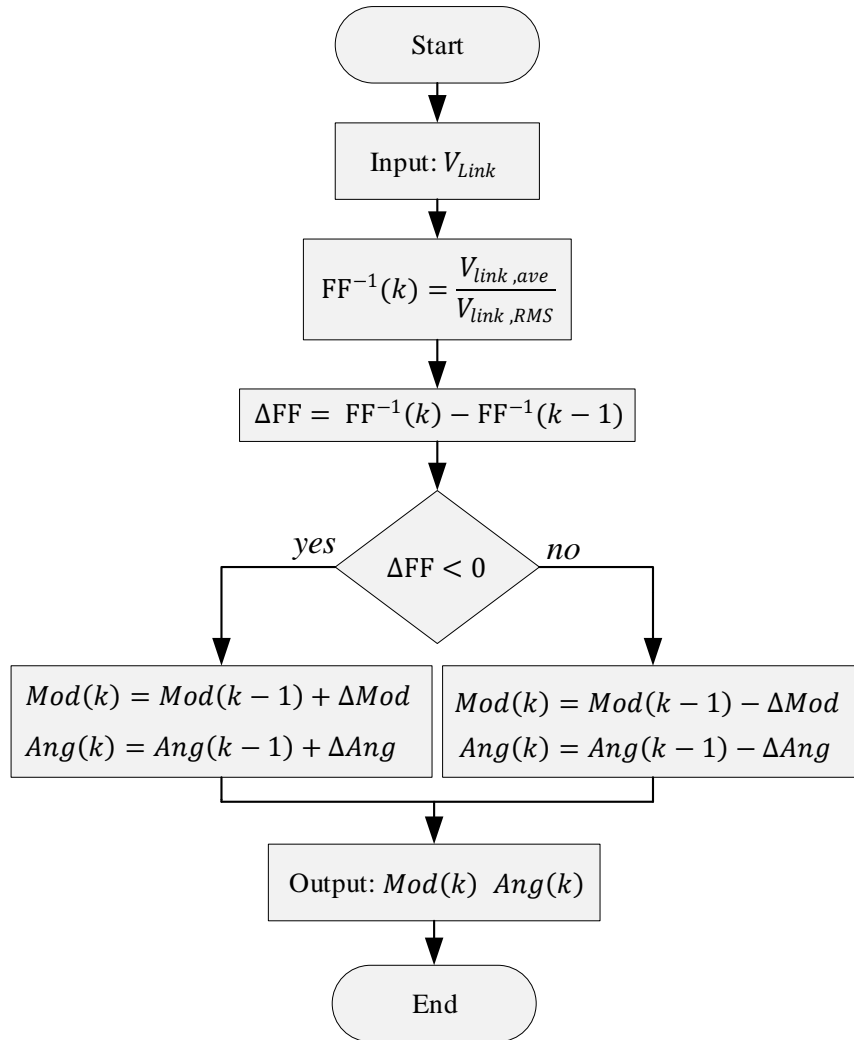


Figure 6.3 Closed-loop hill-climbing based auto-tuning algorithm for the ripple port configuration to achieve a double frequency ripple cancellation.

The proposed closed-loop control scheme for the ripple-port H-bridge inverter is distinct from the grid-tied H-bridge inverter. In other words, the grid-tied H-bridge inverter has its own traditional active-reactive power control, so called PQ decoupling control, to ensure unity power factor integration into the grid. And the ripple port H-bridge inverter, has the hill-climbing based controller described in Figure 6.3.



### 6.3.3. Simulation results of the modulator based control algorithm

A 100 W system system was simulated on Matlab-Simulink to verify the validity of the proposed controller. The component values are displayed in Table 6.1.

Table 6.1 Simulation parameters of the modulator-based controller.

Parameter	Value
dc Link capacitor voltage ( $C_{Link}$ )	16.4 $\mu F$
Ripple port inductor ( $L_d$ )	30 $\mu H$
Ripple port capacitor ( $C_d$ )	140 $\mu F$
LCL filter values	200 $\mu H$ 5 $\mu F$
dc input voltage ( $V_{dc}$ )	20 V
ac grid voltage ( $V_g$ )	24 V <sub>RMS</sub>
Input inductor ( $L_i$ )	100 $\mu H$
Boost converter switching frequency	100 kHz
Inverter switching frequency	20 kHz

Figure 6.4 demonstrates the voltage ripple of the link capacitor before and after turning-on the ripple port closed-loop controller. Before activating the ripple port controller, the amplitude of the double frequency ripple on the link capacitor voltage is 13.5% of the dc voltage. The ripple port controller is activated at time equals one second and the amplitude of the ripple is found to be reduced to 4%. This means that  $C_{link}$  can be made 3.4 times smaller than its original size as is shown in (6.117) using the proposed closed-loop ripple port controller. The settling time was found to be 1.1 seconds. The present step size used to obtain the results in Figure 6.4 for the modulation index controller is  $\Delta Mod = 0.008$  and that of the phase angle is  $\Delta Ang = 0.02$ . By further tuning of the controller step-size, ripple performance can be further improved.

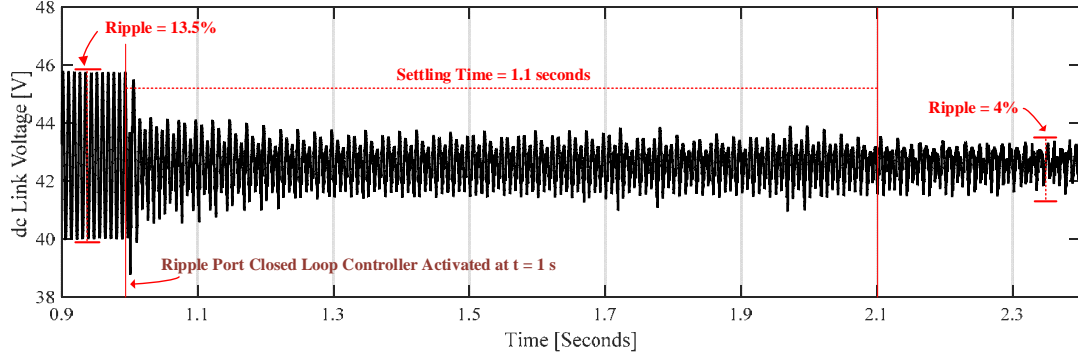


Figure 6.4 Link capacitor voltage response to turning-on the ripple port and its proposed closed loop at time equals 1s. The magnitude of the voltage ripple of the link voltage has gone down from 13.5% to 4% as a result of the hill-climbing auto-tuning algorithm applied on the ripple port. By further tuning of the controller step-size, ripple performance can be further improved. The present step size for the modulation index controller is  $\Delta Mod = 0.008$  and that of the phase angle is  $\Delta Ang = 0.02$ .

Figure 6.5 shows the modulation index ( $Mod(k)$ ) and the phase angle ( $Ang(k)$ ) of the ripple port controller and the resulting inverse form factor ( $FF^{-1}(k)$ ) during the auto-tuning process. Figure 6.5 (a) shows that in steady-state,  $Mod(k)$  converges to a value around 0.39. Similarly Figure 6.5 (b) shows that  $Ang(k)$  converges to a value around 48.3 degrees. These values are very close to the global minimum voltage ripple set of  $[Mod(k), Ang(k)] = [0.38, 49]$  that was shown in Figure 6.2. Generally the oscillations observed in Figure 6.5 (a) and (b) are attributed to the inherent extremum-seeking behavior of the hill-climbing algorithm. Figure 6.5 (c) indicates that after turning-on the ripple port controller,  $V_{ave,dc}$  of the link capacitor becomes much closer to  $V_{RMS,dc}$  which indicates a significant reduction in the double frequency ripple on the dc link capacitor.

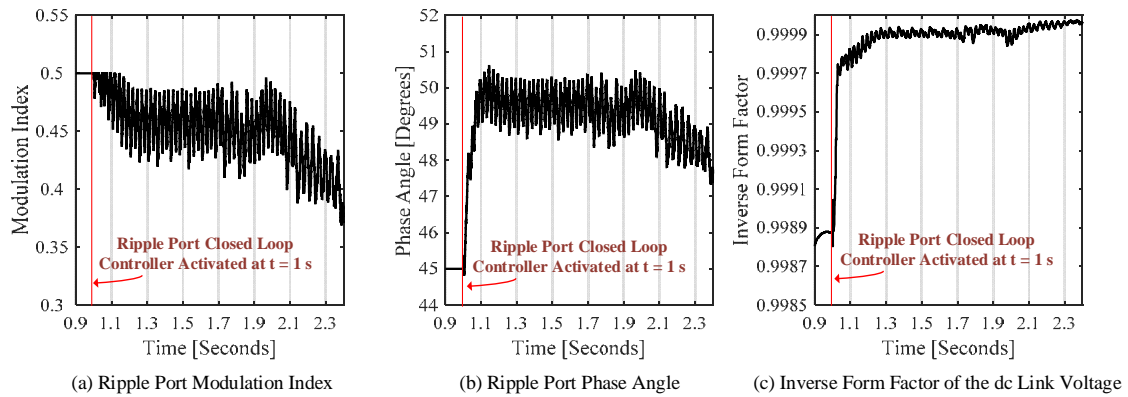


Figure 6.5 Auto-tuning of the ripple-port parameters: modulation index and phase angle, and the resultant inverse form factor of the dc-link voltage. (a) The auto-tuning of the modulation index by the hill-climbing algorithm. (b) The auto-tuning of the phase angle by the hill-climbing algorithm. (c) The inverse form factor ( $V_{ave}/V_{rms}$ ) of the dc-link voltage has approached a value much closer to the ideal “1”. The observed oscillation is due to the inherent extremum-seeking behavior of the hill-climbing algorithm.

Figure 6.6 illustrates the grid side voltage and current. Grid side voltage and current are in-phase before and after the turning on of the closed-loop ripple port inverter controller. This indicates that the unity power factor is maintained before and after turning on the ripple port controller. The total harmonic distortion in the grid current was found to be 2.4% after the closed-loop controller was activated, which is in compliance with the IEEE 519 recommended practice for harmonic control [144].

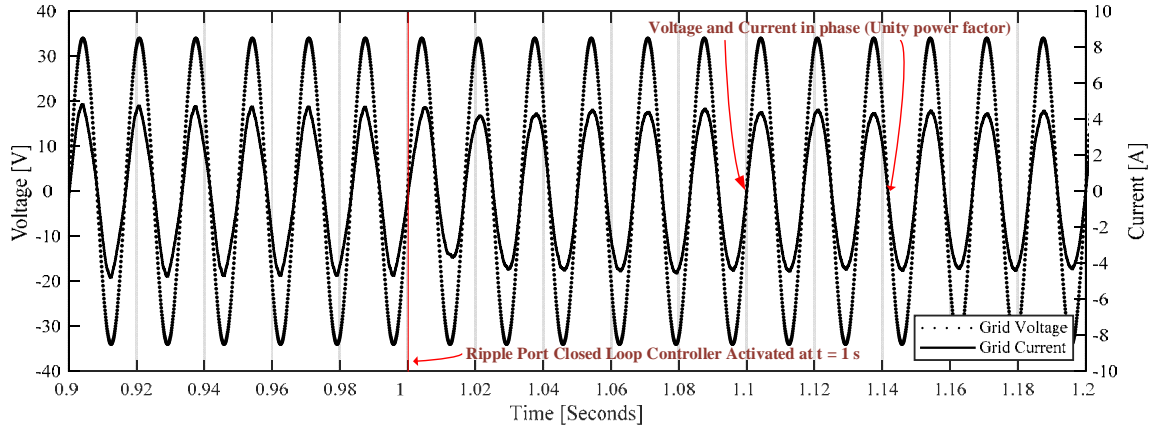


Figure 6.6 Grid side voltage and current are in-phase before and after the turning on of the closed-loop ripple port inverter controller. This indicates that unity power factor is maintained before and after turning on the ripple port controller. The total harmonic distortion in the grid current was found to be 2.4% after the closed loop controller was activated.

The voltage on the ripple port filter capacitor ( $V_{Cd}$ ) during its operation relative to the dc input voltage ( $V_{dc}$ ) and grid ac voltage ( $V_{ac}$ ) is shown in Figure 6.7. The ripple port capacitor voltage,  $V_{Cd}$ , is only visible when the ripple port controller is activated. The phase shift between  $V_{Cd}$  and  $V_{ac}$  is determined by the hill-climbing closed-loop controller of the ripple port ( $Ang(k)$ ).

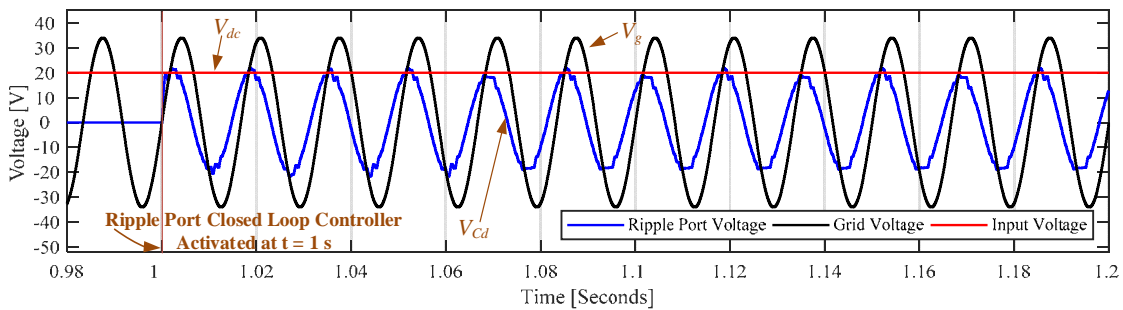


Figure 6.7 The voltage on the ripple port filter capacitor ( $V_{Cd}$ ) during its operation relative to the dc input voltage ( $V_{dc}$ ) and grid ac voltage ( $V_{ac}$ ). The phase shift between  $V_{Cd}$  and  $V_{ac}$  is determined by the hill-climbing closed-loop controller of the ripple port.

#### **6.3.4. Results discussion – motivation for MPC regulator**

The presented modulator-based closed-loop controller for the ripple-port circuit has been shown to converge to some value within a convex optimization problem. As can be observed when comparing Figure 6.4 to Figure 6.2(b), the 4% voltage ripple value was not necessarily the lowest link voltage ripple attainable. This observation could foreseeably be partly mitigated by further tuning of the controller parameters. More importantly, such observation presents an inherent flaw in the presented control algorithm. The presented controller is made of two autonomous controllers, each with a distinct control objective. The first controller has the objective of controlling the grid current injection, a PQ decoupling controller. The second controller is a double frequency regulator. Meeting each of these distinct objectives is a convex optimization problem where each objective has a different set of solutions that may or may not be identical. Additionally, the suggested modulator-based dc-link voltage controller demonstrates an overdetermined control problem in which the modulation index and phase angle are two tunable inputs for one control variable, the dc-link voltage. An overall modulator-based controller for the RP-MII can be illustrated in Figure 6.8.

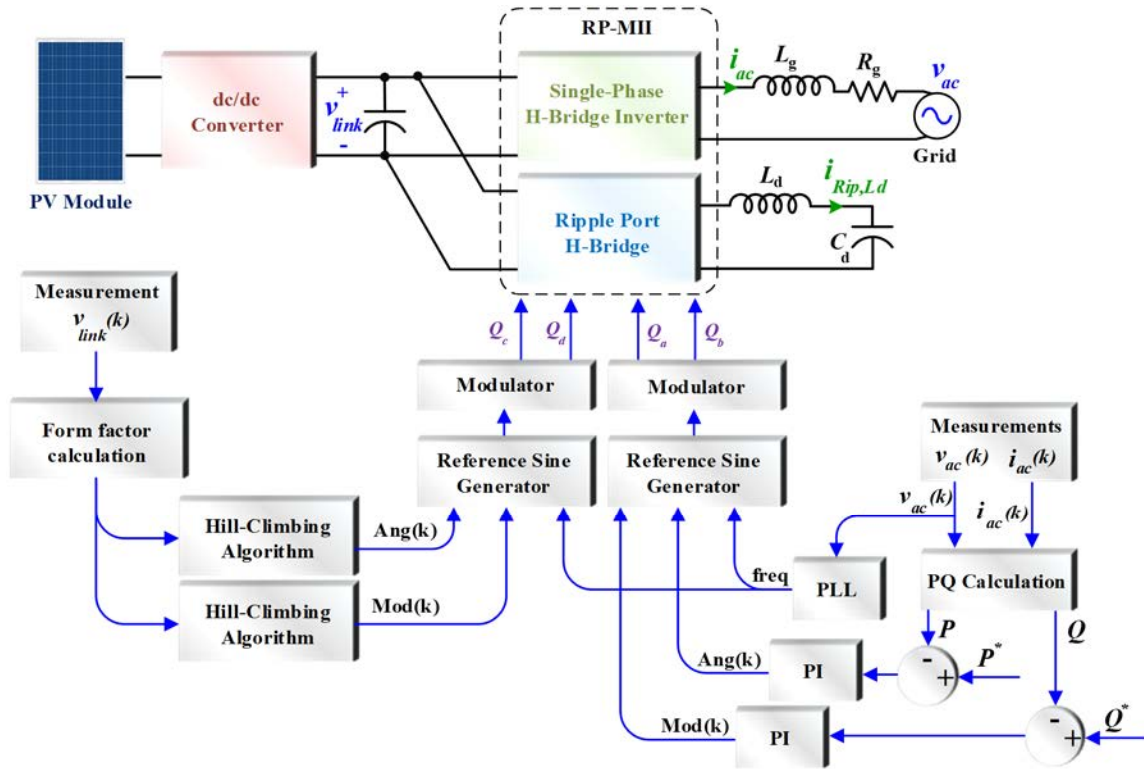


Figure 6.8 Block diagram of the modulator based closed loop controller of the RP-MII. As can be noted, two major loops are displayed: the PQ decoupling controller for the grid side and the dc link voltage ripple loop for the ripple port. More sophisticated controllers on the grid-side have a dc link voltage regulator loop embedded in the grid-side loop. The hill-climbing algorithm of the ripple port is composed of two independent loops.

Figure 6.8 is a block diagram of the modulator based closed-loop controller of the RP-MII. As can be noted, two major loops are displayed: the PQ decoupling controller for the grid side and the dc-link voltage ripple loop for the ripple port. More sophisticated controllers on the grid-side have a dc-link voltage regulator loop embedded in the grid-side loop. The hill-climbing algorithm of the ripple port is composed of two independent loops. An advantageous feature of model predictive control is the multi-objective optimization technique. Using an MPC regulator could reduce the control loops in Figure 6.8 to only one control loop using multi-objective optimization.

## 6.4. Developing the MPC formulation

In the RP-MII (Figure 6.1), the dc-dc input stage provides voltage boost and galvanic isolation [166]. The use of the flyback converter for maximum power point tracking within the MPC framework has been thoroughly discussed in Chapter 3. This section looks into the MPC formulation of the single-phase grid-connected inverter and the proposed ripple control strategy of the dc-link voltage.

### 6.4.1. Background on MPC based grid current controller for a single-phase inverter

Consider the single-phase grid-connected H-bridge inverter in Figure 6.1. The switching configuration of the inverter is shown in Table 6.2. Based on Kirchhoff's current law, the voltage across the filter inductor is

$$v_{Lg} = L_g \frac{di_{ac}}{dt} = \alpha v_{link} - v_{ac} - i_{ac} R_g \quad (6.122)$$

where  $\alpha$  is based on the switching configuration of the inverter is shown Table 6.2 [167].

Table 6.2 Switching states for a single-phase inverter

$Q_a$	$Q_b$	$\alpha$
0	0	0
1	0	1
0	1	-1
1	1	0

The discrete-time estimation of (6.122) in steady-state is found using the Euler forward method for discretization.

$$\tilde{i}_{ac}^{\sigma}(k+1) = \left(1 - \frac{R_g T_s}{L_g}\right) i_{ac}(k) + \frac{T_s}{L_g} (\alpha v_{link}(k) - v_{ac}(k)) \quad (6.123)$$

The reference grid current ( $i_{ac}^*$ ) amplitude is determined based on the photovoltaic maximum power point, as was illustrated in chapter 3. The frequency and phase of  $i_{ac}^*$  are based on the grid voltage. The cost function for the MPC grid controller is written as

$$g_1 = |i_{ac}^* - \tilde{i}_{ac}(k+1)| \quad (6.124)$$

#### 6.4.2. Proposed MPC-based dc-link voltage controller

Consider the equivalent circuit of the RP-MII topology in Figure 6.9. The values of  $\alpha$  and  $\beta$  depend on the switching configuration and are in Table 6.2, depending on the switching state  $\sigma = \{1, 2, \dots, 9\}$ . Based on Kirchoff's current law, the current across the dc-link capacitor is

$$i_{link} = i_{flyb} - \alpha i_{ac} - \beta i_{rp,Ld} \quad (6.125)$$

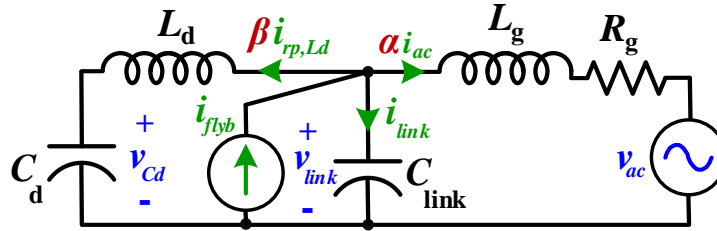


Figure 6.9 Equivalent circuit of the RP-MII during different switching states. The constants  $\alpha$  and  $\beta$  have the values in Table 6.2, depending on the switching state  $\sigma = \{1, 2, \dots, 9\}$ .

The state equations for each of the 9 possible switching states, outlined in Table 6.3, are

$$i_{link}^{\sigma=1} = C_{link} \frac{dv_{link}}{dt} = i_{flyb} \quad (6.126)$$

$$i_{link}^{\sigma=2} = C_{link} \frac{dv_{link}}{dt} = i_{flyb} + i_{rp,Ld} \quad (6.127)$$



$$i_{link}^{\sigma=3} = C_{link} \frac{dv_{link}}{dt} = i_{flyb} - i_{rp,Ld} \quad (6.128)$$

$$i_{link}^{\sigma=4} = C_{link} \frac{dv_{link}}{dt} = i_{flyb} - i_{ac} \quad (6.129)$$

$$i_{link}^{\sigma=5} = C_{link} \frac{dv_{link}}{dt} = i_{flyb} - i_{ac} + i_{rp,Ld} \quad (6.130)$$

$$i_{link}^{\sigma=6} = C_{link} \frac{dv_{link}}{dt} = i_{flyb} - i_{ac} - i_{rp,Ld} \quad (6.131)$$

$$i_{link}^{\sigma=7} = C_{link} \frac{dv_{link}}{dt} = i_{flyb} + i_{ac} \quad (6.132)$$

$$i_{link}^{\sigma=8} = C_{link} \frac{dv_{link}}{dt} = i_{flyb} + i_{ac} + i_{rp,Ld} \quad (6.133)$$

$$i_{link}^{\sigma=9} = C_{link} \frac{dv_{link}}{dt} = i_{flyb} + i_{ac} - i_{rp,Ld} \quad (6.134)$$

The discrete-time estimation of (6.126)-(6.134) in steady-state is found using the Euler forward method for discretization.

$$\tilde{v}_{link}^{\sigma=1}(k+1) = v_{link}(k) + \frac{T_s}{C_{link}} [i_{flyb}(k)] \quad (6.135)$$

$$\tilde{v}_{link}^{\sigma=2}(k+1) = v_{link}(k) + \frac{T_s}{C_{link}} [-i_{rp,Ld}(k) + i_{flyb}(k)] \quad (6.136)$$

$$\tilde{v}_{link}^{\sigma=3}(k+1) = v_{link}(k) + \frac{T_s}{C_{link}} [i_{rp,Ld}(k) + i_{flyb}(k)] \quad (6.137)$$

$$\tilde{v}_{link}^{\sigma=4}(k+1) = v_{link}(k) + \frac{T_s}{C_{link}} [-i_{ac}(k) + i_{flyb}(k)] \quad (6.138)$$

$$\tilde{v}_{link}^{\sigma=5}(k+1) = v_{link}(k) + \frac{T_s}{C_{link}} [-i_{ac}(k) - i_{rp,Ld}(k) + i_{flyb}(k)] \quad (6.139)$$

$$\tilde{v}_{link}^{\sigma=6}(k+1) = v_{link}(k) + \frac{T_s}{C_{link}} [-i_{ac}(k) + i_{rp,Ld}(k) + i_{flyb}(k)] \quad (6.140)$$

$$\tilde{v}_{link}^{\sigma=7}(k+1) = v_{link}(k) + \frac{T_s}{C_{link}} [i_{ac}(k) + i_{flyb}(k)] \quad (6.141)$$

$$\tilde{v}_{link}^{\sigma=8}(k+1) = v_{link}(k) + \frac{T_s}{C_{link}} [i_{ac}(k) - i_{rp,Ld}(k) + i_{flyb}(k)] \quad (6.142)$$

$$\tilde{v}_{link}^{\sigma=9}(k+1) = v_{link}(k) + \frac{T_s}{C_{link}} [i_{ac}(k) + i_{rp,Ld}(k) + i_{flyb}(k)] \quad (6.143)$$

Table 6.3 Switching states of the RP-MII

$\sigma$	$Q_a$	$Q_b$	$Q_c$	$Q_d$	$\alpha$	$\beta$
1	0/1	0/1	0/1	0/1	0	0
2	0/1	0/1	1	0	0	-1
3	0/1	0/1	0	1	0	1
4	1	0	0/1	0/1	1	0
5	1	0	1	0	1	-1
6	1	0	0	1	1	1
7	0	1	0/1	0/1	-1	0
8	0	1	1	0	-1	-1
9	0	1	0	1	-1	1

The discrete state time estimate of the dc-link capacitor voltage  $\sigma$  switching states can generally be written as

$$\tilde{v}_{link}^{\sigma}(k+1) = v_{link}(k) + \frac{T_s}{C_{link}} [-\alpha i_{ac}(k) + \beta i_{rp,Ld}(k) + i_{flyb}(k)] \quad (6.144)$$

The reference dc-link voltage ( $v_{link}^*$ ) value is determined based on the flyback converter input voltage ( $v_{dc}$ ) and duty ratio ( $t_{Q_{f,1}=1}/T_s$ ). The cost function for the MPC dc-link voltage regulator is written as

$$g_2 = |v_{link}^* - \tilde{v}_{link}^{\sigma}(k+1)| \quad (6.145)$$

### 6.4.3. Overall MPC cost function

The state-space representation of the RP-MII has the state variables in matrix form as  $X(k) = [i_{ac}(k) \quad v_{link}(k)]^T$ ; the input matrix is  $U(k) = [i_{flyb}(k) \quad v_{ac}(k)]^T$ , and the output matrix is  $Y(k) = [i_{ac}(k) \quad v_{link}(k)]^T$ . The system model is written as

$$\begin{aligned} \dot{X} &= \begin{bmatrix} 1 & -\alpha/C_{link} \\ \left(1 - \frac{R_g}{L_g}\right) & \alpha/L_g \end{bmatrix} X + \begin{bmatrix} 1/C_{link} & 0 \\ 0 & 1/L_g \end{bmatrix} U + \begin{bmatrix} \beta \\ 0 \end{bmatrix} [i_{rp,Ld}(k)] \\ y &= [1 \quad 1]X \end{aligned} \quad (6.146)$$

The overall cost function encompasses the grid current controller, and the dc-link voltage regulator is as illustrated in

$$\begin{aligned} \min_{\sigma \in \{0,9\}} g_{\sigma} &= \lambda_1 |i_{ac}^* - \tilde{i}_{ac}^\sigma(k+1)| + \lambda_2 |v_{link}^* - \tilde{v}_{link}^\sigma(k+1)| \\ \text{subject to } \tilde{i}_{ac}^\sigma(k+1) &= \left(1 - \frac{R_g T_s}{L_g}\right) i_{ac}(k) + \frac{T_s}{L_g} (\alpha v_{link}(k) - v_{ac}(k)) \\ \tilde{v}_{link}^\sigma(k+1) &= v_{link}(k) + \frac{T_s}{C_{link}} [-\alpha i_{ac}(k) + \beta i_{rp,Ld}(k) + i_{flyb}(k)] \end{aligned} \quad (6.147)$$

where the values of  $\alpha$  and  $\beta$  depend on the switching configuration and are in Table 6.2.

A block diagram of the MPC control strategy applied to the RP-MII is shown in Figure 6.10.

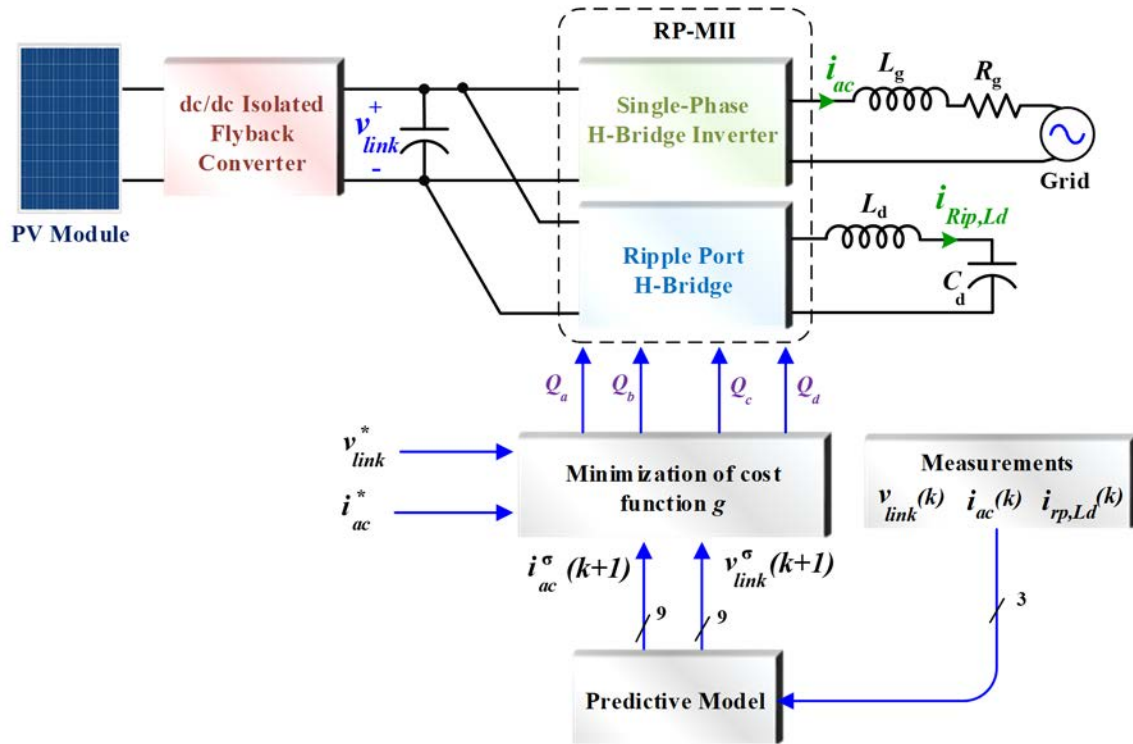


Figure 6.10 A block diagram of the MPC control strategy applied to the RP-MII.

## 6.5. Simulation results

A 500 W system was simulated on Matlab-Simulink to verify the validity of the proposed controller. The component values are displayed in Table 6.4. The MPC code developed for these results is presented in Appendix B.

Table 6.4 Simulation parameters of the RP-MII system.

Parameter	Value
dc Link capacitor voltage ( $C_{Link}$ )	$8 \mu F$
Ripple port inductor ( $L_d$ )	$80 \mu H$
Ripple port capacitor ( $C_d$ )	$2 \mu F$
Grid filter ( $L_g, R_g$ )	$10 \mu H$ $10 \Omega$
dc input voltage ( $V_{dc}$ )	30 V
ac grid voltage ( $V_{ac}$ )	120 V <sub>RMS</sub>
ac grid frequency ( $f_{ac}$ )	60 Hz
Flyback transformer turns ratio ( $n$ )	10

Figure 6.11 demonstrates the voltage ripple of the link capacitor before and after turning-on the ripple port closed-loop controller. The ripple port controller is activated at time equals one second, and the size of the ripple is found to be reduced to 5.3%. These results indicate that total capacitance of  $C_{link} = 8\mu F$  and  $C_d = 2\mu F$ , which could be based on electrolytic capacitors, are sufficient to reduce the double frequency ripple in the dc-link voltage. The settling time was found to be 0.04 seconds.

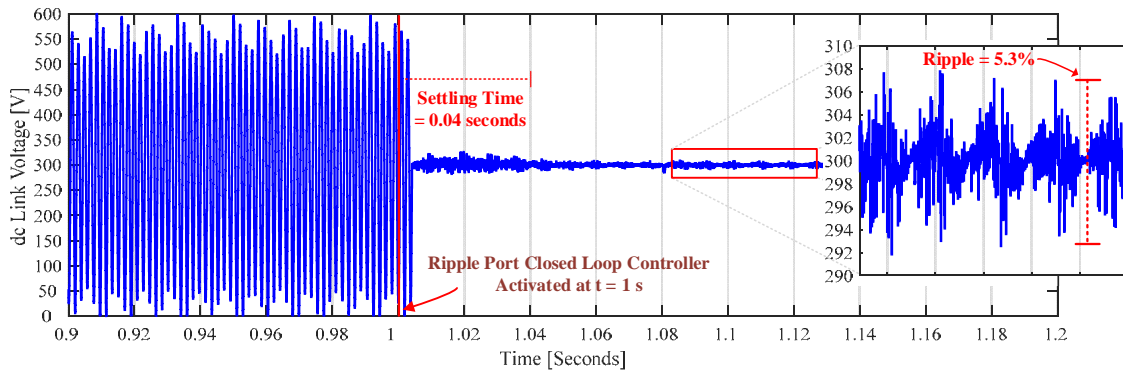


Figure 6.11 Link capacitor voltage response to turning on the ripple port at time equals 1s. The magnitude of the voltage ripple of the link voltage has been reduced to 5.3%.

Figure 6.12 illustrates the grid side voltage and current. Grid side voltage and current are in-phase before and after the turning on of the closed-loop ripple port inverter controller. The results indicate that the unity power factor is maintained before and after turning on the ripple port controller. The total harmonic distortion in the grid current was found to be 1.67% after the closed-loop controller was activated, which complies with the IEEE 519 recommended practice for harmonic control [144].

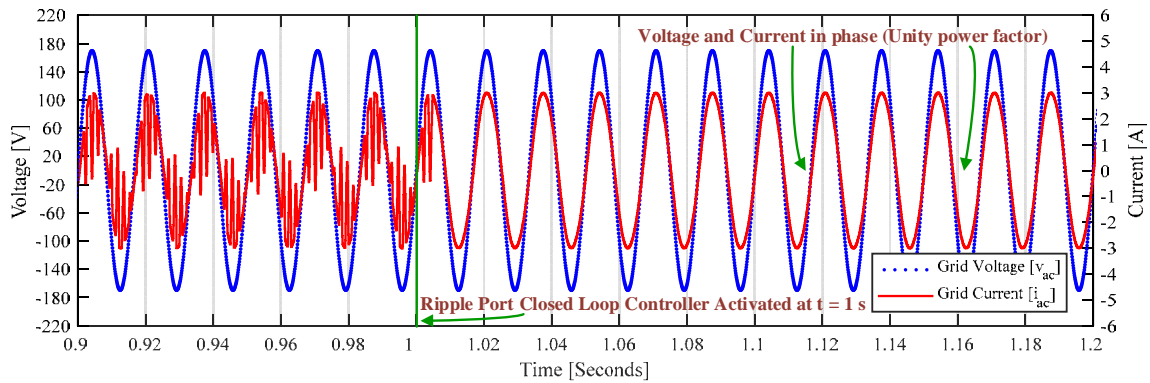


Figure 6.12 Grid side voltage and current are in-phase before and after the turning on of the closed-loop ripple port inverter controller.

## 6.6. Conclusion

This chapter provided a mathematical formulation of the different factors that affect the ripple port inverter's effectiveness in controlling the double frequency ripple at the dc link. A parameter sweep has revealed that to understand the control behavior of the ripple port inverter is convex in nature. Modulator based techniques for dc link ripple regulation use multiple control loops which reduce the tracking accuracy of the overall system. Therefore, a model predictive control framework was used to regulate the grid current injection and the dc-link voltage regulation. Simulation results show that the proposed controller has reduced the dc-link capacitor voltage ripple considerably while using much smaller capacitor values.

## 7. CONCLUSION

This dissertation investigated the controls of the power electronic interfaces with the objective of reducing cost, increasing reliability, and increasing the efficiency of photovoltaic energy conversion systems. The overall theme of this dissertation involved exploring the theory of model predictive control within a range of applications for PV systems. On the control-side, an MPC-based MPPT algorithm has been shown to maximize the energy harvest of the PV module. Within the developed MPC based MPPT framework, sensorless current mode and adaptive perturbation were proposed. The MPC framework was expanded further to include inverter control. The control of a single-phase H-bridge inverter and sub-multilevel inverter were presented in this dissertation to regulate grid current injection. The multi-objective optimization of MPC was employed to control the dc-link voltage in microinverters along with grid current injection. The developed MPC based MPPT controller has been shown to operate with a single-stage impedance source three-phase inverter with PID based grid-side control.

Overall, the applications within PV energy harvesting systems were explored from generation to grid integration to demonstrate the proposed MPC methods. Power optimizers investigated in this dissertation were the flyback converter and the boost converter. Investigated grid interface inverters included the single-phase H-bridge inverter, the sub-multilevel inverter and the three phase H-bridge inverter. The interaction between dc optimizers and single-phase H-bridge inverters within a microinverter configuration was studied. The interconnection between power optimizers with sub-multilevel inverters was investigated. A single-stage impedance source network with a

three-phase H-bridge was investigated for large scale PV installations. The contributions presented in this dissertation according to the chapters are:

Chapter 3 – Maximum power point tracking of standalone dc power optimizers

- MPC-based sensorless current mode
- MPC-based adaptive perturbation MPPT

Chapter 4 – Maximum power point in a grid interactive inverter – sub-multilevel inverter

- MPC based submodule MPPT converters for partial shading mitigation
- MPC based grid integration based on sub-multilevel inverter

Chapter 5 Maximum power point in a grid interactive inverter – impedance source inverter

- MPC based MPPT control of a single-stage power processing systems
- MPC based MPPT integration with pre-existing PID based controller

Chapter 6 Double frequency power ripple controller for microinverters

- MPC-based control strategy for double frequency ripple on dc link voltage reduction in microinverters
- Integrated multi-objective MPC controller for both grid current injection and dc link voltage control.



## REFERENCES

- [1] J. Schellenberg. (2012). *Evaluating the Total Cost of Outages*. Available: <http://grouper.ieee.org/groups/td/dist/sd/doc/2012-07-04-Evaluating-the-Total-Cost-of-Outages.pdf>
- [2] (Sep 2018, Oct). *International Data Base*. Available: <https://www.census.gov/data-tools/demo/idb/informationGateway.php>
- [3] U.S. Energy Information Administration. (2019, Oct). *International Energy Outlook 2019: with projections to 2050*. Available: <https://www.eia.gov/outlooks/ieo/pdf/ieo2019.pdf>
- [4] N. A. Armstrong, "The Engineered Century: A century hence, 2000 may be viewed as quite a primitive period in human history. It's something to hope for.," *The Bridge*, vol. 30, no. 1, pp. 14-18, Spring 2000.
- [5] O. Edenhofer *et al.* (2014). *Climate Change 2014 Mitigation of Climate Change: Working Group III Contribution to the Fifth Assessment Report of the Intergovernmental Panel on Climate Change*. Available: [https://www.ipcc.ch/site/assets/uploads/2018/02/ipcc\\_wg3\\_ar5\\_full.pdf](https://www.ipcc.ch/site/assets/uploads/2018/02/ipcc_wg3_ar5_full.pdf)
- [6] Fraunhofer Institute for Solar Energy Systems. (2019, Oct). *Photovoltaics Report*. Available: <https://www.ise.fraunhofer.de/content/dam/ise/de/documents/publications/studies/Photovoltaics-Report.pdf>
- [7] N. A. Lewis and D. G. Nocera, "The Solar Opportunity," *The Bridge*, vol. 45, no. 2, pp. 41-47, Summer 2015.
- [8] IEA International Energy Agency. (2019). *PVPS 2019: Snapshot of Global PV Markets* [Online]. Available: [www.iea-pvps.org](http://www.iea-pvps.org)
- [9] R. Fu, D. Feldman, and R. Margolis, "U.S. Solar Photovoltaic System Cost Benchmark: Q1 2018," National Renewable Energy Laboratory, Golden, CONREL/TP-6A20-72399, Nov 2018, Available: <https://www.nrel.gov/docs/fy19osti/72399.pdf>.
- [10] K. A. W. Horowitz, T. Remo, B. Smith, and A. Prtak, "A Techno-Economic Analysis and Cost Reduction Roadmap for III-V Solar Cells," National Renewable Energy Laboratory, Golden, CONREL/TP-6A20-72103, Nov 2018, Available: <https://www.nrel.gov/docs/fy19osti/72103.pdf>.

- [11] Y. Yang, K. A. Kim, F. Blaabjerg, and A. Sangwongwanich, *Advances in Grid-Connected Photovoltaic Power Conversion Systems*. Woodhead Publishing, 2018.
- [12] O. Lopez-Lapena, "Time-Division Multiplexing Control of Multi-Input Converters for Low-Power Solar Energy Harvesters," *IEEE Trans. Ind. Electron.*, vol. 65, no. 12, pp. 9668-9676, Dec 2018.
- [13] V. Raveendran, M. Andresen, and M. Liserre, "Improving Onboard Converter Reliability for More Electric Aircraft With Lifetime-Based Control," *IEEE Trans. Ind. Electron.*, vol. 66, no. 7, pp. 5787-5796, Jul 2019.
- [14] F. Blaabjerg, Y. Yang, D. Yang, and X. Wang, "Distributed Power-Generation Systems and Protection," *Proceedings of the IEEE*, vol. 105, no. 7, pp. 1311-1331, Jul 2017.
- [15] T. Ding, Q. Yang, Y. Yang, C. Li, Z. Bie, and F. Blaabjerg, "A Data-Driven Stochastic Reactive Power Optimization Considering Uncertainties in Active Distribution Networks and Decomposition Method," *IEEE Trans. on Smart Grid*, vol. 9, no. 5, pp. 4994-5004, Sep 2018.
- [16] I. G. O. Zurbriggen, Martin, "PV Energy Harvesting Under Extremely Fast Changing Irradiance: State-Plane Direct MPPT," *IEEE Trans. Ind. Electron.*, vol. 66, no. 3, pp. 1852-1861, Mar 2019.
- [17] R. Errouissi and A. Al-Durra, "Disturbance-Observer-Based Control for Dual-Stage Grid-Tied Photovoltaic System Under Unbalanced Grid Voltages," *IEEE Trans. Ind. Electron.*, vol. 66, no. 11, pp. 8925-8936, Nov 2019.
- [18] A. Sangwongwanich and F. Blaabjerg, "Mitigation of Interharmonics in PV Systems With Maximum Power Point Tracking Modification," *IEEE Trans. Power Electron.*, vol. 34, no. 9, Sep 2019.
- [19] S. Qin, C. B. Barth, and R. C. N. Pilawa-Podgurski, "Enhancing Microinverter Energy Capture With Submodule Differential Power Processing," *IEEE Trans. Power Electron.*, vol. 31, no. 5, pp. 3575-3585, May 2016.
- [20] *Photovoltaic (PV) Systems - Characteristics of the Utility Interface*, International Electrotechnical Commission Standard IEC 61727, 2004.
- [21] S. Liu, P. X. Liu, and X. Wang, "Stability Analysis of Grid-Interfacing Inverter Control in Distribution Systems With Multiple Photovoltaic-Based Distributed Generators," *IEEE Trans. Ind. Electron.*, vol. 63, no. 12, pp. 7339-7348, Dec 2016.

- [22] P. Sharma, S. P. Duttgupta, and V. Agarwal, "A Novel Approach for Maximum Power Tracking From Curved Thin-Film Solar Photovoltaic Arrays Under Changing Environmental Conditions," *IEEE Trans. Ind. Appl.*, vol. 50, no. 6, pp. 4142-4151, Nov/Dec 2014.
- [23] C.-T. Pan, M.-C. Cheng, and C.-M. Lai, "Current Ripple-Free Module Integrated Converter (MIC) with More Precise Maximum Power Tracking Control for PV Energy Harvesting," *IEEE Trans. Ind. Appl.*, vol. 51, no. 1, pp. 271-278, 2015.
- [24] A. El Khateb, N. Abd Rahim, J. Selvaraj, and M. Nasir Uddin, "Fuzzy-Logic-Controller-Based SEPIC Converter for Maximum Power Point Tracking," *IEEE Trans. Ind. Appl.*, vol. 50, no. 4, pp. 2349-2358, 2014.
- [25] A. Elrayyah, Y. Sozer, and M. Elbuluk, "Microgrid-Connected PV-Based Sources: A Novel Autonomous Control Method for Maintaining Maximum Power," *IEEE Ind. Appl. Mag.*, vol. 21, no. 2, pp. 19-29, Dec 2015.
- [26] M. Uoya and H. Koizumi, "A Calculation Method of Photovoltaic Array's Operating Point for MPPT Evaluation Based on One-Dimensional Newton-Raphson Method," *IEEE Trans. Ind. Appl.*, vol. 51, no. 1, pp. 567-575, 2015.
- [27] H. Abu-Rub, M. Malinowski, and K. Al-Haddad, *Power Electronics for Renewable Energy Systems, Transportation and Industrial Applications*, 1st ed. West Sussex: IEEE Press and John Wiley & Sons Ltd, 2014.
- [28] M. Das and V. Agarwal, "Novel High-Performance Stand-Alone Solar PV System With High-Gain High-Efficiency dc-dc Converter Power Stages," *IEEE Trans. Ind. Appl.*, vol. 51, no. 6, pp. 4718-4728, Nov/Dec 2015.
- [29] J. Zeng, W. Qiao, and L. Qu, "An Isolated Three-Port Bidirectional dc-dc Converter for Photovoltaic Systems With Energy Storage," *IEEE Trans. Ind. Appl.*, vol. 51, no. 4, pp. 3493-3503, Feb 2015.
- [30] U. M. Choi, F. Blaabjerg, and K. B. Lee, "Control Strategy of Two Capacitor Voltages for Separate MPPTs in Photovoltaic Systems Using Neutral-Point-Clamped Inverters," *IEEE Trans. Ind. Appl.*, vol. 51, no. 4, pp. 3295-3303, Jul-Aug 2015.
- [31] T. ESRAM and P. L. Chapman, "Comparison of photovoltaic array maximum power point tracking techniques," *IEEE Trans. Energy Convers.*, vol. 22, no. 2, pp. 439-449, Jun 2007.
- [32] A. Bidram, A. Davoudi, and R. S. Balog, "Control and Circuit Techniques to Mitigate Partial Shading Effects in Photovoltaic Arrays," *IEEE J. Photovolt.*, vol. 2, no. 4, pp. 532-546, Oct 2012.

- [33] N. Femia, G. Petrone, G. Spagnuolo, and M. Vitelli, "Optimization of perturb and observe maximum power point tracking method," *IEEE Trans. Power Electron.*, vol. 20, no. 4, pp. 963-973, Jul 2005.
- [34] K. A. Kim, R. M. Li, and P. T. Krein, "Voltage-offset resistive control for dc-dc converters in photovoltaic applications," in *IEEE Appl. Power Electron. Conf. and Expo. (APEC)*, Orlando, FL, 5-9 Feb 2012, pp. 2045-2052.
- [35] D. Sera, T. Kerekes, R. Teodorescu, and F. Blaabjerg, "Improved MPPT Algorithms for Rapidly Changing Environmental Conditions," in *IEEE Power Electron. and Motion Control Conf. (EPE/PEMC)*, Novi Sad, 30 Aug - 1 Sep 2006, pp. 1614-1619.
- [36] M. Metry, M. Shadmand, R. S. Balog, and H. Abu-Rub, "MPPT of Photovoltaic Systems Using Sensorless Current-Based Model Predictive Control," *IEEE Trans. Ind. Appl.*, vol. 53, no. 2, pp. 1157-1167, Mar/Apr 2017.
- [37] J. Hu, J. Zhu, G. Lei, G. Platt, and D. G. Dorrell, "Multi-Objective Model-Predictive Control for High-Power Converters," *IEEE Transactions on Energy Conversion*, vol. 28, no. 3, pp. 652-663, 2013.
- [38] Y. Lu, D. Li, Z. Xu, and Y. Xi, "Convergence Analysis and Digital Implementation of a Discrete-Time Neural Network for Model Predictive Control," *IEEE Trans. Ind. Electron.*, vol. 61, no. 12, pp. 7035-7045, Apr 2014.
- [39] M. Metry, M. B. Shadmand, R. S. Balog, and H. Abu-Rub, "A Variable Step-Size MPPT for Sensorless Current Model Predictive Control for Photovoltaic Systems," in *IEEE Energy Convers. Congr. and Expo. (ECCE)*, Milwaukee, WI, 18-22 Sep 2016, vol. PP, pp. 1-8.
- [40] M. B. Shadmand, S. Jain, and R. S. Balog, "Autotuning Technique for the Cost Function Weight Factors in Model Predictive Control for Power Electronic Interfaces," *IEEE J. of Emerg. and Sel. Topics in Power Electron.*, vol. 7, no. 2, pp. 1408-1420, Jun 2019.
- [41] H. T. Nguyen and J.-W. Jung, "Disturbance-Rejection-Based Model Predictive Control: Flexible-Mode Design With a Modulator for Three-Phase Inverters," *IEEE Trans. Ind. Electron.*, vol. 65, no. 4, pp. 2893-2903, Apr 2018.
- [42] J. Holtz and S. Stadtfeld, "A predictive controller for the stator current vector of AC machines fed from a switched voltage source," in *International Power Electronics Conference (IPEC)*, 1983, pp. 1665-1675.
- [43] J. Rodriguez and P. Cortes, *Predictive control of power converters and electrical drives*. Wiley. com, 2012.

- [44] E. F. Camacho and C. Bordons, *Model Predictive Control*, 2nd ed. (Advanced Textbooks in Control and Signal Processing). London, UK: Springer-Verlag London, 2007.
- [45] H. Jiefeng, Z. Jianguo, and D. G. Dorrell, "Model Predictive Control of Grid-Connected Inverters for PV Systems With Flexible Power Regulation and Switching Frequency Reduction," *IEEE Trans. Ind. Appl.*, vol. 51, no. 1, pp. 587-594, Feb 2015.
- [46] M. B. Shadmand, M. Mosa, R. S. Balog, and H. Abu-Rub, "Model Predictive Control of a Capacitor-less Matrix Converter Based STATCOM," *IEEE Journal of Emerging and Selected Topics in Power Electronics*, vol. PP, no. 99, pp. 1-1, Dec 2016.
- [47] J. Sachs and O. Sawodny, "A Two-Stage Model Predictive Control Strategy for Economic Diesel-PV-Battery Island Microgrid Operation in Rural Areas," *IEEE Trans. Sustain. Energy*, vol. 7, no. 3, pp. 903-913, Jul 2016.
- [48] J. Rodriguez *et al.*, "State of the Art of Finite Control Set Model Predictive Control in Power Electronics," *IEEE Transactions on Industrial Informatics*, vol. 9, no. 2, pp. 1003-1016, 2013.
- [49] P. Cortes, A. Wilson, S. Kouro, J. Rodriguez, and H. Abu-Rub, "Model Predictive Control of Multilevel Cascaded H-Bridge Inverters," *IEEE Transactions on Industrial Electronics*, vol. 57, no. 8, pp. 2691-2699, 2010.
- [50] M. B. Shadmand, M. Mosa, R. S. Balog, and H. A. Rub, "An Improved MPPT Technique of High Gain DC-DC Converter by Model Predictive Control for Photovoltaic Applications," in *IEEE Applied Power Electronics Conference & Exposition (APEC)*, 2014, pp. 2993 - 2999.
- [51] M. Mosa, H. Abu-Rub, and J. Rodriguez, "High performance predictive control applied to three phase grid connected Quasi-Z-Source Inverter," in *IEEE Industrial Electronics Society Annual Conference (IECON)*, 2013, pp. 5812-5817.
- [52] M. Mosa, O. Ellabban, A. Kouzou, H. Abu-Rub, and J. Rodriguez, "Model Predictive Control applied for Quasi-Z-source inverter," in *IEEE Applied Power Electronics Conference and Exposition (APEC)*, 2013, pp. 165-169.
- [53] M. Shadmand, R. S. Balog, and H. Abu Rub, "Maximum Power Point Tracking using Model Predictive Control of a flyback converter for photovoltaic applications," in *IEEE Power and Energy Conference at Illinois (PECI)*, 2014, pp. 1-5.

- [54] S. Kouro, M. A. Perez, J. Rodriguez, A. M. Llor, and H. A. Young, "Model Predictive Control - MPC's Role in the Evolution of Power Electronics," *IEEE Ind. Electron. Mag.*, vol. 9, no. 4, pp. 8 - 21, Dec 2015.
- [55] J. Rodriguez *et al.*, "State of the Art of Finite Control Set Model Predictive Control in Power Electronics," *IEEE Trans. Ind. Informat.*, vol. 9, no. 2, pp. 1003-1016, May 2013.
- [56] E. Perez, H. Beltran, N. Aparicio, and P. Rodriguez, "Predictive Power Control for PV Plants With Energy Storage," *IEEE Trans. Sustain. Energy*, vol. 4, no. 2, pp. 482-490, Apr 2013.
- [57] P. T. Krein, *Elements of Power Electronics*, 2nd ed. New York, NY, USA: Oxford University Press, 1998.
- [58] R. D. Middlebrook, "Small-Signal Modeling of Pulse-Width Modulated Switched-Mode Power Converters," *Proceedings of the IEEE*, vol. 76, no. 4, pp. 343-354, Apr 1988.
- [59] D. Liberzon, *Switching in Systems and Control* (Systems & Control: Foundations & Applications). New York, USA: Birkhauser Boston, c/o Springer-Verlag New York, Inc., 2003.
- [60] N. Mohan, T. M. Undeland, and W. P. Robbins, *Power Electronics: Converters, Applications and Design*, Third ed. Danvers, MA, USA: John Wiley & Sons Inc., 2003.
- [61] S. Kouro, P. Cortes, R. Vargas, U. Ammann, and J. Rodriguez, "Model Predictive Control—A Simple and Powerful Method to Control Power Converters," *IEEE Trans. Ind. Electron.*, vol. 56, no. 6, pp. 1826-1838, Jun 2009.
- [62] S.-H. Kim, R.-Y. Kim, and S.-I. Kim, "Generalized Model Predictive Control Method for Single-Phase N-Level Flying Capacitor Multilevel Rectifiers for Solid State Transformer," *IEEE Trans. Ind. Appl.*, May 2019.
- [63] J. H. Lee, M. Morari, and C. E. Garcia, "State-space Interpretation of Model Predictive Control," *Automatica*, vol. 30, no. 4, pp. 707-717, 1994.
- [64] J. Holtz and S. Stadtfeld, "A predictive controller for the stator current vector of AC machines fed from a switched voltage source," in *Int. Power Electron. Conf. (IPEC)*, 1983, pp. 1665–1675.
- [65] P. Mutschler, "A new speed-control method for induction motors," in *PCIM Europe*, Nuremberg, Germany, 1998, pp. 131-136.

- [66] T. Kawabata, T. Miyashita, and Y. Yamamoto, "Dead beat control of three phase PWM inverter," *IEEE Trans. on Power Electron.*, vol. 5, no. 1, pp. 21-28, Jan 1990.
- [67] J. Lee, "Model Predictive Control: Review of the Three Decades of Development," *Int. J. of Control Autom. and Systems*, vol. 9, no. 3, pp. 415-424, Jun 2011.
- [68] A. G. Beccuti, S. Mariéthoz, S. Cliquennois, S. Wang, and M. Morari, "Explicit Model Predictive Control of DC–DC Switched-Mode Power Supplies With Extended Kalman Filtering," *IEEE Trans. Ind. Electron.*, vol. 56, no. 6, pp. 1864-1874, Jun 2009.
- [69] S. Mariéthoz and M. Morari, "Explicit model-predictive control of a PWM inverter with an LCL filter," *IEEE Transactions on Industrial Electronics*, vol. 56, no. 2, pp. 389-399, 2009.
- [70] A. G. Beccuti, S. Mariéthoz, S. Cliquennois, S. Wang, and M. Morari, "Explicit model predictive control of DC–DC switched-mode power supplies with extended Kalman filtering," *IEEE Transactions on Industrial Electronics*, vol. 56, no. 6, pp. 1864-1874, 2009.
- [71] S. Mariéthoz, A. Domahidi, and M. Morari, "Sensorless explicit model predictive control of permanent magnet synchronous motors," in *IEEE Electric Machines and Drives Conference (IEMDC)*, 2009, pp. 1250-1257: IEEE.
- [72] P. Cortes *et al.*, "Guidelines for weighting factors design in Model Predictive Control of power converters and drives," in *IEEE International Conference on Industrial Technology (ICIT)*, 2009, pp. 1-7.
- [73] J. B. Rawlings and D. Q. Mayne, *Model Predictive Control: Theory and Design*. Nob Hill Publishing, 2009.
- [74] L. Cheng *et al.*, "Model Predictive Control for DC–DC Boost Converters With Reduced-Prediction Horizon and Constant Switching Frequency," *IEEE Trans. Power Electron.*, vol. 33, no. 10, pp. 9064-9075, Oct 2018.
- [75] N. Guler and E. Irmak, "A model predictive control-based hybrid MPPT method for boost converters," *Int. J. of Electron.*, pp. 1362-3060, Mar 2019.
- [76] A. El Khateb, N. Abd Rahim, J. Selvaraj, and B. W. Williams, "DC-to-DC Converter With Low Input Current Ripple for Maximum Photovoltaic Power Extraction," *IEEE Trans. Ind. Electron.*, vol. 62, no. 4, pp. 2246-2256, Apr 2015.

- [77] R. W. Erickson and D. Maksimovic, *Fundamentals of Power Electronics*, 1st ed. Boston, MA, USA: Kluwer Academic Publishers, 1997.
- [78] S. J. Castillo, R. S. Balog, and P. N. Enjeti, "Predicting capacitor reliability in a module-integrated photovoltaic inverter using stress factors from an environmental usage model," presented at the North American Power Symposium, Arlington, TX, 26-28 Sept. 2010. Available: <https://ieeexplore.ieee.org/abstract/document/5618955>
- [79] S. A. Larrinaga, M. A. R. Vidal, E. Oyarbide, and J. R. T. Apraiz, "Predictive Control Strategy for DC/AC Converters Based on Direct Power Control," *IEEE Trans. Ind. Electron.*, vol. 54, no. 3, pp. 1261-1271, Jun 2007.
- [80] M. Tomlinson, H. d. T. Mouton, R. Kennel, and P. Stolze, "A Fixed Switching Frequency Scheme for Finite-Control-Set Model Predictive Control—Concept and Algorithm," *IEEE Trans. Ind. Electron.*, vol. 63, no. 12, pp. 7662-7670, Dec 2016.
- [81] M. Tomlinson, T. Mouton, R. Kennel, and P. Stolze, "Model Predictive Control with a Fixed Switching Frequency for a 5-level Flying Capacitor Converter," in *IEEE International Conference on Power Electronics – ECCE Asia (ICPE 2019-ECCE Asia)*, Melbourne, Australia, 3-6 Jun 2013, pp. 1208-1214.
- [82] P. E. Kakosimos, A. G. Kladas, and S. N. Manias, "Fast Photovoltaic-System Voltage- or Current-Oriented MPPT Employing a Predictive Digital Current-Controlled Converter," *IEEE Trans. Ind. Electron.*, vol. 60, no. 12, pp. 5673-5685, Dec 2013.
- [83] H. Chen, F. Xu, and Y. Xi, "Field programmable gate array/system on a programmable chip-based implementation of model predictive controller," *IET Control Theory Appl.*, vol. 6, no. 8, pp. 1055 - 1063, Sep 2012.
- [84] Amin, R. T. Bambang, A. S. Rohman, C. J. Dronkers, R. Ortega, and A. Sasongko, "Energy Management of Fuel Cell/Battery/Supercapacitor Hybrid Power Sources Using Model Predictive Control," *IEEE Trans. Ind. Informat.*, vol. 10, no. 4, pp. 1992-2002, Nov 2014.
- [85] J. Rodríguez; and P. Cortes, *Predictive Control of Power Converters and Electrical Drives*. Hoboken, NJ, USA: Wiley, 2012.
- [86] X. Li, S. Dusmez, U. R. Prasanna, B. Akin, and K. Rajashekara, "A New SVPWM Modulated Input Switched Multilevel Converter for Grid-Connected PV Energy Generation Systems," *IEEE Trans. Emerg. Topics Comput.*, vol. 2, no. 4, pp. 920-930, Dec 2014.



- [87] B. MacCleery, O. Trescases, M. Mujagic, D. M. Bohls, O. Stepanov, and G. Fick, "A new platform and methodology for system-level design of next-generation FPGA-based digital SMPS," in *IEEE Energy Convers. Congr. and Expo. (ECCE)*, Raleigh, NC, 15-20 Sep 2012, pp. 1-8.
- [88] S. Selvakumar, M. Madhusmita, C. Koodalsamy, S. P. Simon, and Y. R. Sood, "High-Speed Maximum Power Point Tracking Module for PV Systems," *IEEE Trans. Ind. Electron.*, vol. 66, no. 2, pp. 1119-1129, Feb 2019.
- [89] M. Adly and K. Strunz, "Irradiance-Adaptive PV Module Integrated Converter for High Efficiency and Power Quality in Standalone and DC Microgrid Applications," *IEEE Trans. Ind. Electron.*, vol. 65, no. 1, pp. 436-446, Jan 2018.
- [90] M. Metry, M. B. Shadmand, L. Yushan, R. S. Balog, and H. Abu Rub, "Maximum power point tracking of photovoltaic systems using sensorless current-based model predictive control," in *IEEE Energy Convers. Congr. and Expo. (ECCE)*, Montreal, QC, 20-24 Sep 2015, pp. 6635-6641.
- [91] D. Sera, L. Mathe, T. Kerekes, S. V. Spataru, and R. Teodorescu, "On the Perturb-and-Observe and Incremental Conductance MPPT Methods for PV Systems," *IEEE J. Photovolt.*, vol. 3, no. 3, pp. 1070 - 1078, Jul 2013.
- [92] E. Mamarelis, G. Petrone, and G. Spagnuolo, "Design of a Sliding-Mode-Controlled SEPIC for PV MPPT Applications," *IEEE Trans. Ind. Electron.*, vol. 61, no. 7, pp. 3387-3398, Jul 2014.
- [93] A. K. Abdelsalam, A. M. Massoud, S. Ahmed, and P. N. Enjeti, "High-Performance Adaptive Perturb and Observe MPPT Technique for Photovoltaic-Based Microgrids," *IEEE Transactions on Power Electronics*, vol. 26, no. 4, pp. 1010-1021, Apr 2011.
- [94] K. S. Tey and S. Mekhilef, "Modified Incremental Conductance Algorithm for Photovoltaic System Under Partial Shading Conditions and Load Variation," *IEEE Trans. Ind. Electron.*, vol. 61, no. 10, pp. 5384-5392, Oct 2014.
- [95] N. Kumar, B. Singh, B. K. Panigrashi, and L. Xu, "Leaky-Least-Logarithmic-Absolute-Difference-Based Control Algorithm and Learning-Based InC MPPT Technique for Grid-Integrated PV System," *IEEE Trans. Ind. Electron.*, vol. 66, no. 11, pp. 9003-9012, Nov 2019.
- [96] D. Das, S. Madichetty, B. Singh, and S. Mishra, "Luenberger Observer Based Current Estimated Boost Converter for PV Maximum Power Extraction—A Current Sensorless Approach," *IEEE J. Photovolt.*, vol. 9, no. 1, pp. 278-286, Jan 2019.

- [97] Life Energy Motion (LEM). (2017). *Datasheet: Current Transducer LTSR 6-NP*. Available: [www.lem.com](http://www.lem.com)
- [98] Allegro Microsystems. (2019). *Datasheet: ACS712 Fully Integrated, Hall-Effect-Based Linear Current Sensor IC with 2.1 kVRMS Isolation and a Low-Resistance Current Conductor*. Available: [www.allegromicro.com](http://www.allegromicro.com)
- [99] A. Itzke, R. Weiss, and R. Wiegel, "Influence of the Conductor Position on a Circular Array of Hall Sensors for Current Measurement," *IEEE Trans. Ind. Electron.*, vol. 66, no. 1, pp. 580-585, Jan 2019.
- [100] Y. Chen, Q. Huang, and A. H. Khawaja, "An Interference-Rejection Strategy for Measurement of Small Current Under Strong Interference With Magnetic Sensor Array," *IEEE Sensors J.*, vol. 19, no. 2, pp. 692-700, Jan 2019.
- [101] B. George, Z. Tan, and S. Nihtianov, "Advances in Capacitive, Eddy Current, and Magnetic Displacement Sensors and Corresponding Interfaces," *IEEE Trans. Ind. Electron.*, vol. 64, no. 2, pp. 9595-9607, Dec 2017.
- [102] P. Midya, P. T. Krein, and M. F. Greuel, "Sensorless current mode control-an observer-based technique for dc-dc converters," *IEEE Trans. Power Electron.*, vol. 16, no. 4, pp. 522-526, Jul 2001.
- [103] N. Kasa, T. Iida, and L. Chen, "Flyback Inverter Controlled by Sensorless Current MPPT for Photovoltaic Power System," *IEEE Trans. Ind. Electron.*, vol. 52, no. 4, pp. 1145 - 1152, Aug 2005.
- [104] G. M. Dousoky, E. M. Ahmed, and M. Shoyama, "Current-sensorless MPPT with dc-dc boost converter for Photovoltaic battery chargers," in *IEEE Energy Convers. Congr. and Expo. (ECCE)*, Raleigh, NC, Sep 20-24 2012, pp. 1607 - 1614: IEEE.
- [105] E. Dallago, D. G. Finarelli, U. P. Gianazza, A. L. Barnabei, and A. Liberale, "Theoretical and Experimental Analysis of an MPP Detection Algorithm Employing a Single-Voltage Sensor Only and a Noisy Signal," *IEEE Trans. on Power Electron.*, vol. 28, no. 11, pp. 5088 - 5097, Nov 2013.
- [106] A. Chikh and A. Chandra, "An Optimal Maximum Power Point Tracking Algorithm for PV Systems With Climatic Parameters Estimation," *IEEE Trans. Sustain. Energy*, vol. 6, no. 2, pp. 644-652, Apr 2015.
- [107] M. Metry and R. S. Balog, "A Model Parity Study on the Model Predictive Control Based Sensorless Current Mode," in *IEEE Int. Conf. on Compatibility, Power Electron. and Power Eng.*, Doha, Qatar, 10-12 Apr 2018, pp. 1-6.

- [108] R. Min, Q. Tong, Q. Zhan, X. Zou, K. Yu, and Z. Liu, "Digital Sensorless Current Mode Control Based on Charge Balance Principle and Dual Current Error Compensation for dc–dc Converters in DCM," *IEEE Trans. Ind. Electron.*, vol. 63, no. 1, pp. 155-165, Jan 2016.
- [109] A. Kwasinski, W. Weaver, and R. S. Balog, *Microgrids and other Local Area Power and Energy Systems*. Cambridge, United Kingdom: Cambridge University Press, 2016.
- [110] T. Dragicevic, X. Lu, J. C. Vasquez, and J. M. Guerrero, "DC Microgrids—Part II: A Review of Power Architectures, Applications, and Standardization Issues," *IEEE Trans. Ind. Electron.*, vol. 31, no. 5, pp. 3528-3549, May 2016.
- [111] S.-H. Lee, W.-J. Cha, B.-H. Kwon, and M. Kim, "Discrete-Time Repetitive Control of Flyback CCM Inverter for PV Power Applications," *IEEE Trans. Ind. Electron.*, vol. 63, no. 2, pp. 976-984, Feb 2016.
- [112] F. F. Edwin, W. Xiao, and V. Khadkikar, "Dynamic Modeling and Control of Interleaved Flyback Module-Integrated Converter for PV Power Applications," *IEEE Trans. Ind. Electron.*, vol. 61, no. 3, pp. 1377-1388, Mar 2014.
- [113] M. Metry, M. B. Shadmand, R. S. Balog, and H. A. Rub, "Sensitivity Analysis to Model Parameter Errors of MPPT by Model Predictive Control for Photovoltaic Applications," presented at the IEEE 1st Workshop on Smart Grid & Renewable Energy (SGRE), Doha, Qatar, Mar, 22-23 Mar 2015.
- [114] M. Metry, M. B. Shadmand, R. S. Balog, and H. Abu Rub, "High Efficiency MPPT by Model Predictive Control Considering Load Disturbances for Photovoltaic Applications Under Dynamic Weather Condition," in *IEEE Ind. Electron. Conf. (IECON)*, Yokohama, Jpn., 9-12 Nov 2015, pp. 4092-4095.
- [115] M. B. Shadmand, R. S. Balog, and H. Abu-Rub, "Model Predictive Control of PV Sources in a Smart dc Distribution System: Maximum Power Point Tracking and Droop Control," *IEEE Trans. Energy Convers.*, vol. 29, no. 4, pp. 913 - 921, Dec 2014.
- [116] J. Guzinski and H. Abu-Rub, "Speed Sensorless Induction Motor Drive With Predictive Current Controller," *IEEE Trans. Ind. Electron.*, vol. 60, no. 2, pp. 699-709, Feb 2013.
- [117] S. Bayhan, M. Trabelsi, H. Abu-Rub, and M. Malinowski, "Finite-Control-Set Model-Predictive Control for a Quasi-Z-Source Four-Leg Inverter Under Unbalanced Load Condition," *IEEE Trans. Ind. Electron.*, vol. 64, no. 4, pp. 2560-2569, Apr 2017.

- [118] P. Manganiello, M. Ricco, G. Petrone, E. Monmasson, and G. Spagnuolo, "Optimization of Perturbative PV MPPT Methods Through Online System Identification," *IEEE Trans. Ind. Electron.*, vol. 61, no. 12, pp. 6812-6821, Dec 2014.
- [119] M. A. Elgendy, B. Zahawi, and D. J. Atkinson, "Assessment of the Incremental Conductance Maximum Power Point Tracking Algorithm," *IEEE Trans. Sustain. Energy*, vol. 4, no. 1, pp. 108-117, Jan 2013.
- [120] C.-C. Hua, Y.-H. Fang, and W.-T. Chen, "Hybrid maximum power point tracking method with variable step size for photovoltaic systems," *IET Renewable Power Generation*, vol. 10, no. 2, pp. 127-132, Feb 2016.
- [121] H. A. Sher, A. F. Murtaza, A. Noman, K. E. Addoweesh, K. Al-Haddad, and M. Chiaberge, "A New Sensorless Hybrid MPPT Algorithm Based on Fractional Short-Circuit Current Measurement and P&O MPPT," *IEEE Trans. Sustain. Energy*, vol. 6, no. 4, pp. 1426 - 1434, Oct 2015.
- [122] J. Ahmed and Z. Salam, "A Modified P&O Maximum Power Point Tracking Method with Reduced Steady State Oscillation and Improved Tracking Efficiency," *IEEE Trans. Sustain. Energy*, Early Access vol. PP, no. 99, p. 1, May 2016.
- [123] F. Paz and M. Ordonez, "High-Performance Solar MPPT Using Switching Ripple Identification Based on a Lock-In Amplifier," *IEEE Trans. Ind. Electron.*, vol. 63, no. 6, pp. 3595-3604, Jun 2016.
- [124] H. F. Blanchette, T. Ould-Bachir, and J. P. David, "A State-Space Modeling Approach for the FPGA-Based Real-Time Simulation of High Switching Frequency Power Converters," *IEEE Trans. Ind. Electron.*, vol. 59, no. 12, pp. 4555-4567, Dec 2012.
- [125] R. Bründlinger, N. Henze, H. Häberlin, B. Burger, A. Bergmann, and F. Baumgartner, "prEN 50530 - The New European Standard for Performance Characterisation of PV Inverters," presented at the 24th European Photovoltaic Solar Energy Conference, Germany, September 2009, 21-25 Sep 2009.
- [126] D. C. Montgomery and G. C. Runger, *Applied Statistics and Probability for Engineers*, 6th ed. Wiley, 2014.
- [127] M. Metry and R. S. Balog, "A Parameter Mismatch Study on Model Predictive Control Based Sensorless Current Mode," in *IEEE Texas Power and Energy Conf. (TPEC)*, College Station, TX, 8-9 Feb 2018, pp. 1-6.

- [128] A. Andreas and S. Wilcox, "Observed Atmospheric and Solar Information System (OASIS) - SOLRMAP University of Arizona: 2018 Data," in *NREL Report No. DA-5500-56494*, ed. Tucson, Arizona (Data, 2010): <http://dx.doi.org/10.5439/1052226>.
- [129] K. Chen, S. Tian, Y. Cheng, and L. Bai, "An Improved MPPT Controller for Photovoltaic System Under Partial Shading Condition," *IEEE Trans. Sustain. Energy*, vol. 5, no. 3, pp. 978-985, Jul 2014.
- [130] C. Manickam, G. R. Raman, G. P. Raman, S. I. Ganesan, and C. Nagamani, "A Hybrid Algorithm for Tracking of GMPP Based on P&O and PSO With Reduced Power Oscillation in String Inverters," *IEEE Trans. Ind. Electron.*, vol. 63, no. 10, pp. 6097-6106, Oct 2016.
- [131] A. Ramyar, H. Iman-Eini, and S. Farhangi, "Global Maximum Power Point Tracking Method for Photovoltaic Arrays Under Partial Shading Conditions," *IEEE Trans. Ind. Electron.*, vol. 64, no. 4, pp. 2855-2864, Apr 2017.
- [132] C. Olalla, D. Clement, M. Rodriguez, and D. Maksimovic, "Architectures and Control of Submodule Integrated DC–DC Converters for Photovoltaic Applications," *IEEE Trans. Power Electron.*, vol. 28, no. 6, pp. 2980-2997, Jun 2013.
- [133] M. Metry, S. Bayhan, R. S. Balog, and H. Abu Rub, "Model Predictive Control for PV Maximum Power Point Tracking of Single-Phase subMultilevel Inverter," in *IEEE Power and Energy Conf. at Illinois (PECI)*, Illinois, 19-20 Feb 2016, pp. 1-8.
- [134] M. Metry, S. Bayhan, M. B. Shadmand, R. S. Balog, and H. Abu-Rub, "Sensorless Current Model Predictive Control for Maximum Power Point Tracking of Single-Phase subMultilevel Inverter for Photovoltaic Systems," in *IEEE Energy Convers. Congr. and Expo. (ECCE)*, Milwaukee, WI, 18-22 Sep 2016, vol. PP, pp. 1-8.
- [135] C. Olalla, C. Deline, D. Clement, Y. Levron, M. Rodriguez, and D. Maksimovic, "Performance of Power-Limited Differential Power Processing Architectures in Mismatched PV Systems," *IEEE Trans. Power Electron.*, vol. 30, no. 3, pp. 618-631, Feb 2015.
- [136] M. Mosa, H. Abu-Rub, M. E. Ahmed, A. Kouzou, and J. Rodriguez, "Control of single phase grid connected multilevel inverter using model predictive control," in *Fourth International Conference on Power Engineering, Energy and Electrical Drives (POWERENG)*, 2013, pp. 624-628.

- [137] M. Mousa, M. E. Ahmed, and M. Orabi, "New converter circuitry for high v applications using Switched Inductor Multilevel Converter," in *IEEE 33rd International Telecommunications Energy Conference (INTELEC)*, 2011, pp. 1-8.
- [138] M. Trabelsi, S. Bayhan, M. Metry, H. Abu Rub, L. Ben-Brahim, and R. S. Balog, "An Effective Model Predictive Control for Grid Connected Packed U Cells Multilevel Inverter," in *IEEE Power and Energy Conf. at Illinois (PECI)*, Illinois, 19-20 Feb 2016, pp. 1 - 6: IEEE.
- [139] S. Bayhan and H. Abu-Rub, "Model predictive sensorless control of standalone doubly fed induction generator," presented at the IEEE Ind. Electron. Conf. (IECON), Oct, 2014. Available: <http://dx.doi.org/10.1109/iecon.2014.7048802>
- [140] D. Q. Mayne, J. B. Rawlings, C. V. Rao, and P. O. M. Scokaert, "Constrained model predictive control: Stability and optimality," *Automatica*, vol. 36, pp. 789-814, Nov 2000.
- [141] M. F. Kangarlu and E. Babaei, "A Generalized Cascaded Multilevel Inverter Using Series Connection of Submultilevel Inverters," *IEEE Trans. Power Electron.*, vol. 28, no. 2, pp. 625-636, Feb 2013.
- [142] E. Babaei, S. Laali, and Z. Bayat, "A Single-Phase Cascaded Multilevel Inverter Based on a New Basic Unit With Reduced Number of Power Switches," *IEEE Trans. Ind. Electron.*, vol. 62, no. 2, pp. 922-929, Feb 2015.
- [143] A. M. Gole et al., "Guidelines for modeling power electronics in electric power engineering applications," *IEEE Trans. Power Del.*, vol. 12, no. 1, pp. 505-514, Jan 1997.
- [144] I. W. Group, "519-2014 - IEEE Recommended Practice and Requirements for Harmonic Control in Electric Power Systems," *IEEE Std 519-2014 (Revision of IEEE Std 519-1992)*, Standard pp. 1-29, Jun 2014.
- [145] P. Fang Zheng, "Z-source inverter," *IEEE Trans. Ind. Appl.*, vol. 39, no. 2, pp. 504-510, 2003.
- [146] M. Aleenejad, H. Mahmoudi, and R. Ahmadi, "A Fault-Tolerant Strategy Based on Fundamental Phase-Shift Compensation for Three-Phase Multilevel Converters With Quasi-Z-Source Networks With Discontinuous Input Current," *IEEE Trans. on Power Electron.*, vol. 31, no. 11, pp. 7480-7488, Nov 2016.
- [147] Y. Liu, H. Abu-Rub, and B. Ge, "Z-Source/Quasi-Z-Source Inverters: Derived Networks, Modulations, Controls, and Emerging Applications to Photovoltaic Conversion," *IEEE Ind. Electron. Mag.*, vol. 8, no. 4, pp. 32-44, Dec 2014.

- [148] H. Abu-Rub, Y. Liu, B. Ge, F. Blaabjerg, O. Ellabban, and P. Chiang Loh, *Impedance source power electronic converters*, 1st ed. West Sussex: IEEE Press and John Wiley & Sons Ltd, 2016.
- [149] H. Abu-Rub, A. Iqbal, S. Moin Ahmed, F. Z. Peng, L. Yuan, and B. Ge, "Quasi-Z-Source Inverter-Based Photovoltaic Generation System With Maximum Power Tracking Control Using ANFIS," *IEEE Trans. Sustain. Energy*, vol. 4, no. 1, pp. 11-20, Jan 2013.
- [150] M. Metry, Y. Liu, R. S. Balog, and H. Abu-Rub, "Model Predictive Control for Maximum Power Point Tracking of Quasi-Z-Source Inverter Based Grid-Tied Photovoltaic Power System," presented at the IEEE Int. Symp. on Ind. Electron., Edinburgh, Scotland, UK, 19-21 Jun 2017.
- [151] G. Baoming *et al.*, "An Energy-Stored Quasi-Z-Source Inverter for Application to Photovoltaic Power System," *IEEE Trans. Ind. Electron.*, vol. 60, no. 10, pp. 4468-4481, 2013.
- [152] L. Yuan, F. Z. Peng, J. G. Cintron-Rivera, and J. Shuai, "Controller design for quasi-Z-source inverter in photovoltaic systems," in *IEEE Energy Convers. Congr. and Expo. (ECCE)*, 2010, pp. 3187-3194.
- [153] X. Li, H. Zhang, M. B. Shadmand, and R. S. Balog, "Model Predictive Control of a Voltage-Source Inverter With Seamless Transition Between Islanded and Grid-Connected Operations," *IEEE Trans. Ind. Electron.*, vol. 64, no. 10, pp. 7906-7917, Oct 2017.
- [154] P. S. Shenoy, K. A. Kim, B. B. Johnson, and P. T. Krein, "Differential Power Processing for Increased Energy Production and Reliability of Photovoltaic Systems," *IEEE Trans. Power Electron.*, vol. 28, no. 6, pp. 2968-2979, Jun 2013.
- [155] J. Wei and B. Fahimi, "Maximum solar power transfer in Multi-port Power Electronic Interface," in *IEEE Appl. Power Electron. Conf. and Expo. (APEC)*, 2010, pp. 68-73.
- [156] H. Wang, M. Liserre, and F. Blaabjerg, "Toward Reliable Power Electronics: Challenges, Design Tools, and Opportunities," *IEEE Ind. Electron. Mag.*, vol. 7, no. 2, pp. 17-26, Jun 2013.
- [157] H. Hu, S. Harb, N. Kutkut, I. Bataresh, and J. Z. Shen, "A Review of Power Decoupling Techniques for Microinverters With Three Different Decoupling Capacitor Locations in PV Systems," *IEEE Trans. on Power Electron.*, vol. 28, no. 6, pp. 2711-2726, Oct 2012.

- [158] V. M. Iyer and V. John, "Low-frequency dc bus ripple cancellation in single phase pulse-width modulation inverters," *IET Power Electron.*, vol. 8, no. 4, pp. 497-506, Oct 2014.
- [159] H. Li, K. Zhang, H. Zhao, S. Fan, and J. Xiong, "Active Power Decoupling for High-Power Single-Phase PWM Rectifiers," *IEEE Trans. Power Electron.*, vol. 28, no. 3, pp. 1308-1319, Mar 2013.
- [160] H. Han, Y. Liu, Y. Sun, M. Su, and W. Xiong, "Single-phase current source converter with power decoupling capability using a series-connected active buffer," *IET Power Electron.*, vol. 8, no. 5, pp. 700-707, Oct 2014.
- [161] M. Jang, M. Ciobotaru, and V. G. Agelidis, "A Single-Stage Fuel Cell Energy System Based on a Buck–Boost Inverter with a Backup Energy Storage Unit," *IEEE Trans. Power Electron.*, vol. 27, no. 6, pp. 2825-2834, Jun 2012.
- [162] P. T. Krein, R. S. Balog, and M. Mirjafari, "Minimum Energy and Capacitance Requirements for Single-Phase Inverters and Rectifiers Using a Ripple Port," *IEEE Trans. on Power Electron.*, vol. 27, no. 11, pp. 4690-4698, 3 Feb 2012.
- [163] S. Harb, M. Mirjafari, and R. S. Balog, "Ripple-Port Module-Integrated Inverter for Grid-Connected PV Applications," *IEEE Trans. Ind. Appl.*, vol. 49, no. 6, pp. 2692-2698, 17 May 2013.
- [164] B. Tian, S. Harb, and R. S. Balog, "Ripple-port integrated PFC rectifier with fast dynamic response," in *IEEE International Midwest Symposium on Circuits and Systems (MWSCAS)*, College Station, TX, 3-6 Aug 2014, vol. PP, pp. 781-784.
- [165] M. Metry, M. Kim, and R. S. Balog, "A Hill-Climbing Optimization Approach for Closed-Loop Auto-Tuning of the Grid-Connected Ripple-Port Inverters," in *IEEE Int. Conf. on Power Electron. – ECCE Asia (ICPE 2019-ECCE Asia)*, Busan, Korea, 27-30 May 2019, pp. 754-759.
- [166] M. Mirjafari, S. Harb, and R. S. Balog, "Multiobjective Optimization and Topology Selection for a Module-Integrated Inverter," *IEEE Trans. Power Electron.*, vol. 30, no. 8, pp. 4219-4231, Aug 2015.
- [167] P. Cortés, M. P. Kazmierkowski, R. M. Kennel, D. E. Quevedo, and J. Rodríguez, "Predictive Control in Power Electronics and Drives," *IEEE Trans. Ind. Electron.*, vol. 55, no. 12, pp. 4312-4324, Dec 2008.



## APPENDIX A

### SENSORLESS CURRENT MPPT BASED ON MPC

#### Sensorless current MPPT based on MPC

by Morcos Metry

```
% Input: PV voltage Vpv
%   Output voltage Vout

% Output: Digital MPC output - switch state S
%   A duty ratio for use with a high frequency modulator - D

function [S, D] = MPC_function(Enabled, Vpv, Vout)
```

#### Setting initial and parameter values for the flyback converter

```
Vinit = 35; %Initial value for D output
Vmax = 45; %Maximum value for D
Vmin = 2; %Minimum value for D
%deltaV = Param(4); %Increment value used to increase/decrease the duty cycle D
% ( increasing D = decreasing Vref )
Ts = 10e-6; %Sampling Time
R = 430; %Resistor Value
Cin = 94e-6; %Input Capacitor Value
Cout = 100e-6; %Output Capacitor Value
n = 10; %Turns Ratio

persistent Vrefold Pold S_old D_old k;
if isempty(Vrefold)
    Pold=0;
    D_old = 0.1;
    S_old = 0;
    k=0;
    Vrefold=Vinit;
end
```

## Model-based estimation

```
% Current surrogate model (ipv(k))
ipv = ((n*D_old)/((1-D_old)*R))*Vout + ((Cin/Ts)*(Vpv-Vpv_old));

% State variable estimation (Vpv(k+1))
Vmpc1 = ((1-D_old)/(n*D_old))*(1-(Ts/(R*Cout)))*Vout;
Vmpc0 = ((1-D_old)/(n*D_old))*(1-(Ts/(R*Cout)))+(Ts/(R*Cout*(1-D_old))))*Vout;

% Step-size estimation (delta_V)
Vmpc_ave = 0.5*(Vmpc1+Vmpc0);
deltaV = Vmpc_ave - Vpv;
```

## MPPT reference calculation

```
P= Vpv*ipv;
dV= Vpv - Vrefold;
dP= P - Pold;
if dP ~= 0 && Enabled ~=0
    if dP < 0
        if dV < 0
            Vref = Vrefold + deltaV;
        else
            Vref = Vrefold - deltaV;
        end
    else
        if dV < 0
            Vref = Vrefold - deltaV;
        else
            Vref = Vrefold + deltaV;
        end
    end
else
    Vref=Vrefold;
end

if Vref >= Vmax
    Vref=Vmax;
end
if Vref<= Vmin
    Vref=Vmin;
end
```

## Cost function optimization

```
% Cost function for MPC-MPPT
g1 = abs(Vref - Vmpc1);
g0 = abs(Vref - Vmpc0);

% Finding the control actuate S that minimizes the cost function g
if g1 < g0
    S = 1;
elseif g0 < g1
    S = 0;
else
    S = (1-S_old);
end

k=k+1;
S_mem(k) = S;

% Finding an average (mean) value for duty ratio D
% based on the past 1000 control actuates S
if k==1000
    D = sum(S_mem)/1000;
    k=0;
else D = D_old;
end

D_old = D;
S_old = S;
Vrefold=Vref;
Pold=P;
```

*Published with MATLAB® R2018b*

## APPENDIX B

### MPC CONTROLLED RIPPLE-PORT MODULE INTEGRATED INVERTER CODE

#### MPC controlled ripple-port module integrated inverter code

By Morcos Metry

#### Parameter definition

```
Ts=0.5e-6;
Ts_Control=Ts;
Ts_Power=Ts;
C_rip = 2e-6;
L_rip = 80e-6;
Cf = 1e-6;
C_link = 8e-6;
Lf = 2.183e-3;
L1 = 100e-6;
% Load parameters
R = 10; % Resistance [Ohm]
L = 10e-3; % Inductance [H]
e = 120; % Grid Voltage RMS [V]
f_e = 60*(2*pi); % Back-EMF frequency [rad/s]
Vlink_dc_ref = 300; % DC-link voltage [V]
% Current reference
I_ref_peak = 10; % Peak amplitude [A]
f_ref = 50*(2*pi); % Frequency [rad/s]

% Voltage vectors
v0 = 0; %00
v1 = Vlink_dc_ref; % 10
v2 = -Vlink_dc_ref; %01
v3 = 0; % 11
v = [v0 v1 v2 v3];
% Switching states
states = [0 0;1 0 ;0 1;1 1];
```

## Code for grid-current control

```
function [x_opt, Sa,Sb] = control(I_ref,I_meas, Ts, R, L, v, states)
```

```
% Variables defined in the parameters file
x_opt = 1;
% Optimum vector and measured current at instant k-1
persistent x_old i_old
% Initialize values
if isempty(x_old),
    x_old = 1;
end
if isempty(i_old),
    i_old = 0+1j*0;
end
g_opt = 1e10;

% Read current reference inputs at sampling instant k
ik_ref = I_ref(1);
% Read current measurements at sampling instant k
ik = I_meas(1);
% Back-EMF estimate
e = v(x_old) - L/Ts*ik - (R - L/Ts)*i_old;
% Store the measured current for the next iteration
i_old = ik;
```

## Model-based estimation for each switching configuration

```
for i = 1:4
    v_o1 = v(i); % i-th voltage vector for current prediction
    ik1 = (1 - R*T_s/L)*ik + T_s/L*(v_o1 - e); % Current prediction at instant k+1
    g = abs(real(ik_ref - ik1)); % Cost function
    % Selection of the optimal value
    if (g < g_opt)
        g_opt = g;
        x_opt = i;
    end
end
x_old = x_opt; % Store the present value of x_opt
% Output switching states
Sa = states(x_opt,1);
Sb = states(x_opt,2);
```

## Code for dc link voltage controller as a continuation of the previous code

This code and the above code are designed to be one integrated function. The code was separated into two different functions to ease the debugging process.

```
function [x_opt, qX, Sc, Sd] = control(Sa, Sb, v_clink_ref, v_clink, iac, irp, ilink, Ts, R, L, states, irp_V, C_link, vgV)

% Variables defined in the parameters file
x_opt = 1;
% Optimum vector and measured current at instant k-1
persistent x_old vck_old m
% Initialize values
if isempty(x_old),
    m=1;
    x_old = 1;
end
if isempty(vck_old),
    vck_old = 0;
end
g_opt = 1e10;

gsv = nan(4,1);
g_out = nan(4,1);
g_out2 = nan(4,2);

if Sa == 1 && Sb == 0
    igS = -1;
else if Sa == 0 && Sb == 1
    igS = 1;
else igS = 0;
end
end

% Read current reference inputs at sampling instant k
vck_ref = v_clink_ref;
% Read current measurements at sampling instant k
vck = v_clink;
% Store the measured voltage for the next iteration
vck_old = vck;
```

## Model-based estimation for each switching configuration

```
for i = 1:4
% i-th voltage vector for current prediction
irpS = irp_V(i);
% Current prediction at instant k+1
vck1 = vck + (Ts/C_link)*((iac*igS)+(irp*irpS)+ilink);
% Cost function
g = abs(real(vck_ref - vck1)^2);
% Selection of the optimal value
if (g < g_opt)
g_opt = g;
x_opt = i;
end
end

mm = 1; % mm = m;
x_opt = g_out2(mm,1);
m=mm;
```

## Store the present value of x\_opt

```
x_old = x_opt;
% Output switching states
Sc = states(x_opt,1);
Sd = states(x_opt,2);
```

Display the precise state selected from the 9 RP-MII possible states

The combines outcome of both codes

```
qS = [Sa Sb Sc Sd];
if qS == [0 0 0 0];
    qX = 1;
else if qS == [0 0 1 0];
    qX = 2;
else if qS == [0 0 0 1];
    qX = 3;
else if qS == [1 0 0 0];
    qX = 4;
else if qS == [1 0 1 0];
    qX = 5;
else if qS == [1 0 0 1];
    qX = 6;
else if qS == [0 1 0 0];
    qX = 7;
else if qS == [0 1 1 0];
    qX = 8;
else if qS == [0 1 0 1];
    qX = 9;
else qX = 0;
end
end
end
end
end
end
end
end
end
end
end
end
end
```

*Published with MATLAB® R2018b*